MODELING DISPERSION INTERACTIONS ON METAL SURFACES USING THE EXCHANGE-HOLE DIPOLE MOMENT

by

Matthew S. Christian

Submitted in partial fulfillment of the requirements

for the degree of Doctor of Philosophy

at

Dalhousie University

Halifax, Nova Scotia

June 2018

Dedicated to my dear family and friends, who have shepherded me through my education, and to Isabel, my emotional rock.

Table of Contents

List of Tables

List of Figures

Abstract

Graphene is a two-dimensional material possessing unique electrical and physical properties. London dispersion interactions play a significant role in its adsorption and friction on metal surfaces. Accurate computational modeling of these processes is complicated by the fact that conventional density-functional methods do not include the proper physics to describe dispersion interactions. Modeling dispersion between a metal surface and substrate is found to be particularly complex as models based on properties of the free metal atoms alone cause the interaction strength to be over-estimated. As an alternative, the exchange-hole dipole moment (XDM) method is a density-dependent dispersion correction that has previously been shown to model dispersion interactions accurately for both molecules and solids. In this thesis, we first test the validity of XDM for modeling surface-substrate dispersion interactions for a set of small aromatic molecules physisorbed on noble-metal (111) surfaces. Upon validation of XDM for molecular adsorption, we investigated interfaces of single and double-layered graphene on selected transition-metal surfaces in two rotational orientations. Our results show that thermal effects greatly affect the potential energy surface for graphene on a nickel surface. In general, the rotational orientation significantly affects graphene interlayer distances and interactions and there is an energetic preference for substrate alignment. Our results also demonstrate that metal substrates affect interlayer distances and exfoliation energies for bilayer graphene systems that chemisorb to metal surfaces. The sliding of multi-layered graphene is investigated in detail for copper surfaces. It is shown that the energetically preferred sliding interface is between graphene and the copper surface, even when subjected to an applied constraint. Our results consistently demonstrate that XDM captures the proper physics required to model surface dispersion interactions.

List of Abbreviations and Symbols Used

α Atomic polarizability

α_i^{SCS} MBD Self-Consistent screening atomic polarizability

α_i^{TS} vdW-TS atomic polarizability

β Surface heating rate

$\langle p_i|$ PAW projector function

$\chi(\mathbf{r}, \mathbf{r}, i\omega)$ Density-density fluctuation response function

χ_i MBD quantum oscillator mass and displacement

$\epsilon_B(i\omega)$ Solid dielectric function

$\epsilon_C^{\mathrm{unif}}$ Correlation energy for a uniform electron gas

$\epsilon_X^{\mathrm{unif}}$ Exchange energy for a uniform electron gas

η_f Frictional interaction of a film on a surface

$\hbar$ Reduced Plank's constant (1.054×10^{-34}J·s)

$|\psi_{\mathrm{ps}}\rangle$ Pseudoized wave-function

$|\psi_{\mathrm{real}}\rangle$ All-electron wave-function

λ Electronic system coupling constant

λ_i MBD energy eigenvalue

μ Surface coefficient of friction

$\nabla\rho$, $\nabla\rho(\mathbf{r})$ Density gradient

$\nu(\Theta)$ Coverage-dependent desorption pre-exponential constant

ν_d Coverage independent desorption pre-exponential constant

ω Electron density fluctuation

ω_{MBD} MBD quantum oscillation frequency

ω_p Frequency of photoelectron

ω_q Vibrational frequency of quartz substrate

Φ Work function energy

ϕ_{ps} Pseudo atomic radial wave function

ϕ_{real} All-electron atomic radial wave function

Π_{ij} Dipole interaction tensor

$\psi(\mathbf{r})$ Crystal wave function

ψ_{cut} Wave function cut-off parameter for PAW

$\rho, \rho(\mathbf{r})$ Electron density

ρ_{cut} Density cut-off parameter for PAW

ρ_{eff} Effective electron density

ρ_{free} Free electron density

ρ_f Mass density of adsorbed film

ρ_q Mass density of quartz microbalance

σ Integral smearing parameter

τ Film characteristic slip time

$\mathbf{a}_1$, $\mathbf{a}_2$, $\mathbf{a}_3$ Lattice vector

$\mathbf{k}$ Reciprocal lattice vector

$\mathbf{r}$ Electron coordinates

$\mathbf{T}$ Crystal Bravais vector

Θ Molecular surface coverage

θ Angle between atoms

θ_C Displacement angle of AFM cantilever

θ_e Electron emission angle

Θ_t Surface coverage at time t

ζ Electron spin polarizability

a Crystal lattice constant

a_1, a_2 XDM Damping parameters

A_c Surface area of a cell

b_{TS} TS fitting constant

C_G Fitted constant for Grimme DFT-D2

C_n Dispersion coefficient

$d_{X,\sigma}$ Exchange-hole dipole moment

$E_{\mathrm{adsorption}}$ Molecular adsorption energy

E_{complex} Kinetic and potential energy of a molecule on a surface

E_{molec} Kinetic and potential energy of a molecule

E_{surf} Kinetic and potential energy of a surface

E_{base} DFT functional contribution

E_{kin} Kinetic energy of a photoelectron

E_{MBD} MBD dispersion energy

E_{XDM} XDM dispersion energy contribution

E_B Binding energy to eject an electron from a bulk material

E_C Correlation energy

E_d Desorption energy

E_{XC} Exchange-correlation energy

E_X Exchange energy

$f(\mathbf{r}, \mathbf{r}')$ vdW-DF kernel function

F_{AFM} Force measured by an atomic force microscope

f_{damp} Dispersion correction damping function

F_l AFM lateral force

F_N AFM normal force

$F_X(s)$ Exchange enhancement factor

G_C AFM cantilever shear modulus

h Plank's constant (6.626×10^{-34}J·s)

$H(\rho, \zeta, \nabla, \rho)$ Correlation gradient contribution

H_{MBD} MBD Hamiltonian

I_p Atomic ionization potential

k, l, m, n Stoichiometric coefficients

k_B Boltzmann's constant ($1.380 \times 10^{-23}\text{J}\cdot\text{K}^{-1}$)

k_C AFM cantilever vertical spring constant

k_l AFM cantilever lateral force constant

L_C AFM cantilever length

L_t Length of AFM tip

m_e Mass of an electron

m_f Mass of adsorbed substrate on QCM

M_i Dipole multipole moment

m_q Mass of quartz microbalance

n_1, n_2, n_3 Lattice translation constant

n_D Desorption rate constant

n_s Number of atoms per unit cell

P_c Pressure in a closed cell

Q QCM quality factor

R Molar gas constant ($8.314\ \text{JK}^{-1}\text{mol}^{-1}$)

$r(\Theta)$ Rate of molecular desorption

R_0, R_{ij}^c Critical vdW radii cut-off

R_{LEED} LEED global scaling factor

R_{ij} Inter-atomic distance

s Reduced electron density gradient

s_G Grimme global scaling factor

S_p Gas pumping speed

T Temperature

t Time

t_C AFM cantilever thickness

T_g Gas-phase temperature

T_m Temperature of maximum molecular desorption

t_q Thickness of quartz microbalance

$u(\mathbf{r})$ One-electron periodic potential

V_{eff} Effective atomic volume

V_{free} Free atomic volume

$v_{\mathbf{r}}$ Normal unit vector

V_c Volume of a cell

w_C AFM cantilever width

$w_i(r)$ Hirshfeld partition weight

x AFM lateral scanning

Y_C Young's modulus for AFM cantilever

Z Atomic nuclear charge

Z_C AFM cantilever vertical displacement

Z_l AFM cantilever lateral displacement

AFM Atomic force microscopy

ARPES Angle resolved photo-electron spectroscopy

B86b Becke GGA exchange functional

CVD Chemical vapor deposition

DFT Density-functional theory

DFT-D Grimme dispersion correction

fcc Face centered cubic

GGA General gradient approximation

hcp Hexagonal closest-packed

LAPW Linear augmented plane wave

LC-ωPBE Range-separated GGA hybrid functional

LDA Local density approximation

LEED Low-energy electron diffraction

MBD Many-body dispersion correction

NCI Non-covalent interactions

PAW Projector augmented wave

PBE Perdew, Burke, Ernzerhof GGA functional

PES Potential energy surface

QCM Quartz crystal microbalance

QTAIM Bader's quantum theory of atoms in molecules

STM Scanning tunnel microscopy

TPD Temperature programmed desorption

vdW-DF van der Waals density functional

vdW-TS Tkatchenko and Scheffler dispersion correction

vdW-TS$^{\text{surf}}$ Tkatchenko and Scheffler surface dispersion correction

XDM Exchange-hole dipole moment

Acknowledgements

I would like to thank Dr. Erin Johnson for her tutelage for the past five years. Her guidance and supervision has allowed me to become the scientist that I am today. I would not have been able to achieve what I have without her.

I would like to thank my fellow researchers of the Johnson Research Group, Luc LeBlanc, Fredrick Hills-Feng, Alastair Price and Dr. Stephen Dale, who provided valuable help and feedback with my research and whom I am honored to also call friends. I would additionally like to thank the conversations with Dr. Axel Becke, Dr. Jan Henrick Pohls and Alex Patterson. I thank the patience of Dr. Alberto Otero de la Roza for helping me carry out my initial studies and who provided me with invaluable technical support and Dr. Enrico Benassi, who provided an early outline for this thesis. I also would like to thank the Dalhousie Department of Chemistry, who provided a nurturing environment for scientific thought and growth.

I would like to thank the love and support of my parents, Brad and Christie Christian, the support of my sister, Michelle Christian, and the support of my extended family and friends. Most of all, I would like to acknowledge the love and support of Isabel Lawrence, whose constant presence has provided shelter for the stresses of graduate school.

Finally, I would like to acknowledge the financial support of the Nova Scotia Graduate Scholarship fund for providing financial assistance to my studies

Chapter 1: Introduction

Two-dimensional (2D) materials possess a planar, lamellar structure formed upon exfoliation from the bulk. The interlayer interactions of the bulk allotrope are dominated by London dispersion,[1,2] which has become a defining characteristic in identifying new 2D materials.[2] These materials show different physical and chemical properties as an isolated single-layer than in their bulk allotropes. Some 2D materials have the potential to replace silicon in electronics[3,4] and have shown promise for photocatalytic applications.[5–7] The applications for these materials range from molecular sensors[4,8] to solid lubricants.[9–11]

The number of 2D material classes are too many to be discussed here, but a few have dominated the recent literature.[1,2] Transition metal dichalcogenides (TMD) are layered compounds with a general formula of MX_2, where M is a transition metal and X is a chalcogen, such as S, Se or Te.[8] Each 2D TMD consists of repeating layers that are three atoms thick: a transition metal layer sandwiched between two chalcogen layers. These materials have been shown to be promising photocatalysts and optical sensors.[8,12,13] Boron nitride (BN) has become an important 2D material for nano-electronics because it is an excellent insulator and interacts weakly with other materials. This has made BN an ideal substrate base for creating layered electronic components.[14,15] Materials such as silicene and black phosphorus have also been heavily investigated.[13,16]

Graphene is the archetype 2D material. First theoretically predicted,[3,4] then experimentally isolated in 2004,[17] it has been studied thoroughly because of its unique electronic band structure that is sensitive to changes in chemical environment, specifically molecular adsorption.[3,4,18] Graphene also has ideal lubrication

properties due to its continuous aromatic pi region that interacts weakly with substrates via London dispersion.[9,10,19] It has also become one of the few 2D materials to become commercially available and incorporated into consumer products.[18]

Methods to manufacture 2D materials can be subdivided into two classes: exfoliation methods,[3,17,18,20] where layers are physically separated from the bulk material, and synthetic methods,[21–23] where the 2D material is synthesized on a substrate using a precursor. Laboratory material samples are typically generated using a mechanical exfoliation method,[17] which is not scalable for industrial production. Chemical-based separation methods, where charged solvent atoms diffuse between the van der Waals interlayer, have also shown promise for some 2D materials.[6,24–26] The repulsive force of the solvent ions is greater than the attractive dispersion interactions, resulting in bulk layer separation. However, exfoliation methods can result in surface defects that hinder active material properties. Synthetic routes, if mastered, can efficiently produce defect-free 2D materials.[26] Mechanical sputtering[27,28] and chemical vapor deposition (CVD)[20,21,23,29] are two leading synthetic methods. Synthetic methods require the use of a substrate, like a metal surface, to use as a scaffold for monolayer formation. Both methods deposit a precursor, either in solid or vapor form, onto a substrate surface. The precursor then reacts to form the 2D material.[20,23]

Interactions between materials and metal surfaces have been investigated both experimentally[29–34] and theoretically[35–37] in order to optimize production processes and to investigate manipulation of material properties, such as the electronic band gap. Mechanistic studies have been carried out to better understand monolayer formation on metal scaffolds[38] and to understand the parameters that drive defect formation during CVD.[36,37] Such studies have been used to explain orientation-dependent interactions of graphene on metals[34] and to explain Moiré pattern formation,[39] which refers to the overlay pattern of the 2D material laid on a substrate. Metals also provide a source for charge donation. It has been shown that charge transfer from a metal to a 2D material can alter a material's band gap[4,20] and

enhance catalytic activity.[40] This has been specifically shown for TMDs where charge donation enhances the material's metallic character, increasing catalytic activity for the hydrogen evolution reaction.[24]

2D materials are also excellent solid lubricants because of their weak interlayer dispersion interactions. Bulk allotropes of 2D materials, like graphite, have been used for many years as lubricants.[11] Even the adsorption of a single 2D layer significantly decreases the friction at a surface.[41,42] As the number of 2D layers increase at the sliding interface, the friction decreases.[41–44] 2D coatings also make the surface more resilient to wear because of strong lateral interatomic bonds in these materials.[45] Maximum lubricity occurs when the 2D material lays flat on a substrate and strongly interacts with the surface.[19,41,46] Material rippling due to defects or lattice constant mismatch reduces lubricity.[42] Creating new 2D materials for lubricants is an active research area.

Computational investigations of 2D materials can provide insight into substrate effects on adsorption energies and physical properties. Surface adsorption processes are traditionally classified as either chemisorption, where covalent and ionic interactions dominate, or physisorption, where molecules bind primarily via weak non-covalent interactions.[47] Therefore, chemisorption interactions are typically stronger than physisorption. 2D materials typically physisorb or weakly chemisorb onto metal surfaces.[23,48,49] Inclusion of dispersion interactions is essential to accurately model molecular adsorption, particularly physisorption, and for modeling 2D materials.[36,50–52] Even when 2D materials chemisorb to metal substrates, dispersion interactions constitute a significant contribution to the adsorption energy.[52,53]

Most computational surface-adsorption investigations use periodic-boundary density-functional methods with the local density approximation[38,53] or generalized gradient approximation functionals.[54] These methods perform well for covalent or ionic bonding, but historically fail to predict accurate adsorption of most 2D materials to substrates due to the neglect of dispersion interactions. Dispersion

interactions in materials can be accurately modeled using the random phase approximation.[39,50] However, the cost of this method makes it impracticable to apply to large systems.[55] A practical way to fix the failure of local density-functional approximations is to add a dispersion-energy correction.[56–61]

Dispersion energies can be calculated using a pairwise interaction approach based on perturbation theory for interacting instantaneous multipoles.[56–61] At the start of this thesis, it was largely believed that pairwise atomic models could not properly model surface dispersion interactions.[59,62,63] Early pairwise dispersion energy corrections typically over-estimated adsorption energies and underestimated bond lengths for physisorbed molecules on surfaces.[56,64] This was because these methods used fixed- empirical parameters for the dispersion coefficients and not because they were a pairwise atomic approach. Neglect or inaccurate treatment of dispersion interactions will result in large errors in calculating material-metal distances, adsorption energies, and frictional barriers.[53] It is therefore imperative to properly model the material-metal surface interactions.

The objective of this thesis is to show that metal–2D-material interactions can be accurately modeled using density-functional theory (DFT) with the exchange-hole dipole moment (XDM) dispersion correction.[60,61] Graphene is chosen as a model 2D material because of its central importance in modern materials chemistry and because of its good lattice match with noble-metal substrates.

This thesis consists of a sequence of papers, published or in-process, that discuss the role of dispersion interactions at metal surfaces as modeled by the XDM dispersion correction. Background information about experimental methods used to validate our results is presented in Chapter 2. The theoretical methods used in our investigations, such as DFT, are reviewed in Chapters 3-4. We begin by showing that a flexible pairwise dispersion model, specifically XDM, can accurately reproduce experimental adsorption energies of small aromatic molecules on noble metal surfaces in Chapter 5. This was the first benchmark to show that pairwise dispersion methods, like XDM, can provide accurate energies for adsorp-

tion on metal surfaces. In Chapter 6, we verify that the accuracy of DFT-XDM for molecular adsorption processes transfers to the adsorption of graphene on the Ni (111) surface, which is a particularly challenging case because of the sensitive balance between dispersion and electrostatic interactions that controls the shape of the potential energy surface. We then expanded our investigation of graphene adsorption to additional (111) metal surfaces and benchmarked our results against reported structures and energies calculated using the random phase approximation in Chapter 7. In Chapter 8, substrate contributions to bilayer graphene interlayer distances and sliding energy barriers are investigated. Finally, Chapter 9 discusses sliding-energy barriers of multiple graphene layers over Cu (111) at equilibrium and under compression. Though we concentrate on graphene, the approaches that were developed for this thesis can be generally applied to other 2D materials.

Chapter 2: Experimental Methods

A variety of experimental methods can be used to characterize surfaces. However, this section will only concentrate on methods that provided data for direct comparison with the theoretical results presented in this thesis. It is important to understand these experimental methods because each method has inherent limitations in what they measure. A large disadvantage of these experimental methods is that they measure surface-averaged values and lack the resolution required to measure the single-molecule–surface interactions that are studied here.

2.1 Temperature Programmed Desorption (TPD) Methods for Adsorption Energies

Molecular adsorption energies are typically determined via temperature programmed desorption (TPD) methods. TPD spectra were originally produced using flash-filament desorption,[65] in which a gas-phase substrate is streamed at a steady rate through a cell containing a sample surface. The pressure at this steady state is marked as a baseline. A heated filament inside the cell prevents the substrate from adsorbing on the surface. Turning the filament off cools the system, allowing the substrate to adsorb to the surface. The feed and exhaust gas ports are then shut, creating a closed system. As the system cools, pressure decreases. The amount of molecules adsorbed at any instant can be obtained either from a pressure burst upon flashing the filament, or from the decrease in cell pressure during adsorption. From the cell pressure P_c, adsorbent area A_c, system pumping speed S_p, cell volume V_c, and gas temperature T_g, the rate of desorption, $d\Theta/dt$, of a

molecule from the surface upon filament flashing is

$$\frac{d\Theta}{dt} = \left(\frac{V_c}{A_c k_B T_g}\right)\left[\frac{dP_c}{dt} + \frac{S_p}{V_c}P_c\right], \tag{2.1.1}$$

where Θ is the molecular surface coverage in molecules per unit area.[65]

A more accurate way of obtaining the desorption rate is by analyzing desorption spectra with a mass spectrometer. This method was introduced by Gert Ehrlich in his study of molecular nitrogen on tungsten surfaces.[65] His results showed that nitrogen weakly adsorbs to tungsten surfaces and established a new paradigm for determining molecule-surface adsorption energies. Generating TPD spectra with a mass spectrometer is simpler than using flash desorption analysis. To obtain a TPD spectrum, a mass spectrometer focuses on the mass of the molecule of interest. The sample surface is heated at a continuous rate β (K/s) while the mass spectrometer records the intensity of molecular desorption. The produced curve of time versus intensity can then be used for analysis.[66,67]

All TPD analysis methods are derived from an Arrhenius-type expression known as the Polanyi-Wigner equation,[67–71]

$$r(\Theta) = \frac{d\Theta}{dt} = \nu(\Theta)\Theta e^{-E_d/RT}. \tag{2.1.2}$$

The rate of molecular desorption, $r(\Theta)$, as a function of surface coverage, Θ, is dependent on the temperature T, the molecular desorption energy E_d, and a pre-exponential factor $\nu(\Theta)$ in s^{-1}. R is the molar gas constant in $J{\cdot}mol^{-1}K^{-1}$. Many TPD analysis methods are derived from this equation. Determination of E_d for a molecule is trivial if $\nu(\Theta)$ is known; however, this is rarely the case. In order to remove coverage-dependencies, approximations simplify the Polanyi-Wigner equation. A popular approximation is the Redhead equation:[72]

$$E_d = RT_m[\ln(\nu_d T_m/\beta) - 3.46]. \tag{2.1.3}$$

This equation is valid only for first-order desorption rates. In this method, $\nu(\Theta)$ is coverage independent (ν_d) and is chosen to be $10^{13}/s$, a value derived by Redhead from a fit of $\nu(\Theta)$ to desorption rates of hydrogen and argon on tungsten. This allows the activation energy to be determined from a plot of desorption rate versus T_m, the temperature of maximum desorption. Furthermore, ν_d can be determined if E_d is known:

$$\nu_d = (E_d\beta/RT_m^2\Theta_0^{n_D-1})e^{E_d/RT_m}, \tag{2.1.4}$$

where n_D is the desorption rate order. This is a coverage-independent approximation. As such, the Redhead approximation fails when molecules have strong coverage dependencies.[68] However, E_d is usually predicted to be within 1.5% if ν_d is known.[66] Generally, a poor approximation of ν_d results in an inaccurate adsorption energy. This property, known as the compensation effect, states that an overestimated ν_d results in an overestimation of E_d and an underestimation of ν_d results in an underestimation of E_d.[68] Methods have been developed to determine accurate pre-exponential factors and add coverage dependence.[70]

In complete analysis,[70] $\nu(\Theta)$ and E_d are coverage dependent. For coverage at time t, Θ_t is given by

$$\Theta_t = S_p/(A_c k_B T)\int_0^\infty P_c dt. \tag{2.1.5}$$

An Arrhenius plot of $\ln[r(\Theta_t)]$ against $1/T$ is constructed corresponding to a coverage Θ_t. Since the pre-exponential factor is a constant at constant Θ, the slope yields $E(\Theta)$, independent of $\nu(\Theta)$. Repeating the procedure for different values of Θ_t constructs a plot of $E(\Theta)$. If the plot satisfies

$$E(\Theta) = \ln\left[\nu(\Theta)\right] + n_D \ln\left[\Theta\right], \tag{2.1.6}$$

$\nu(\Theta)$ is not coverage dependent. If the plot is non-linear, then $\nu(\Theta)$ is coverage

dependent.[69–71] Complete analysis has been shown to yield more accurate pre-exponential factors and adsorption energies than Redhead analysis.[66,68]

TPD-derived adsorption energies are important for benchmarking computational methods for surface adsorption. Computationally determined adsorption energies for benzene have matched well with experimental TPD data[47] because benzene does not have a coverage-dependent surface orientation or strong intermolecular interactions.[73] More complex molecules, such as nucleobases, have lower computationally predicted adsorption energies than Redhead TPD-derived adsorption energies because they have strong intermolecular interactions as well as coverage-dependent surface orientations.[66,70] Due to the lack of accounting for intermolecular interactions and coverage-dependent properties, TPD-derived adsorption energies should be taken more as approximations than as exact adsorption energies. The experimental adsorption energies reported here were obtained from either complete analysis or Redhead TPD experiments.

2.2 Angle Resolved Photo-Electron Spectroscopy (ARPES)

Angle resolved photoemission spectroscopy (ARPES) is a spectroscopic technique used to probe electronic properties of solids. The basis of ARPES is Einstein's photoelectric effect, where adsorption of a photon leads to an electronic excitation, causing the ejection of an electron. An ARPES measurement can decompose important features of a solid, such as electronic band structure and density of states.[74]

An ARPES spectrum is produced by focusing a monochromatic beam from a discharge lamp or synchrotron source onto the surface of a sample, ejecting an electron. The analyzer then determines the intensity and angle of the photoelectron emission based on the collision of the photoelectron with the lens.[75] Photoemission intensity is a function of the photon energy, $\hbar\omega_p$, where ω_p is the frequency of the photon and $\hbar$ is the reduced Planck's constant (J/s). Since energy is conserved, the energy of the photon must be equal to the energy of the emitted

photoelectron:

$$E_{\text{kin}} + |E_B| + \Phi = \hbar\omega_p, \tag{2.2.1}$$

where E_B is the binding energy of the electron in the sample, E_{kin} is the kinetic energy of the photoelectron, and Φ is the work function energy. From the kinetic energy of the electron, the crystal momentum $\hbar\mathbf{k}$ can be calculated as

$$\hbar\mathbf{k} = \sqrt{2m_e E_{\text{kin}}} \cdot \sin\theta_e, \tag{2.2.2}$$

where m_e is the mass of an electron. The angle θ_e is the electron emission angle with respect to the surface normal.[76] From this, it is possible to determine the electron energy as a function of the reciprocal lattice vector $\mathbf{k}$, producing an electronic band structure. Most ARPES experiments are performed at ultraviolet frequencies, particularly $h\omega_p$ less than 100 eV. This is because the momentum resolution of ARPES is high at lower energies. The ARPES emission can be further decomposed theoretically into a product of one-particle spectral functions and Fermi distribution functions, allowing direct insight into the Bloch states of a solid.[77]

ARPES has an important role in characterizing solids and it remains a main experimental technique to determine electronic band structures. Furthermore, because surface states are highly sensitive to perturbations, ARPES is used for structural analysis of layered materials via changes in their component band structures. Heterogeneous materials, where layers strongly interact, have a band structure that is perturbed with respect to that of the isolated component. This thesis compares computationally predicted graphene-metal interactions with reported results that used ARPES measurements.[75,77]

2.3 Low Energy Electron Diffraction (LEED)

Low energy electron diffraction (LEED) is a powerful tool used to image surface structures.[78–81] The principles of LEED are similar to other diffraction methods, in that a material is bombarded with electrons and the structure is resolved from the resulting scattering pattern.[79,80,82] Though measuring a LEED spectrum is relatively simple, electronic scattering theory is employed to decipher the electron refraction pattern. It is therefore a hybrid analytic technique that requires both laboratory and computational approaches to resolve a surface structure.[83–85]

A typical LEED optical setup consists of a filament that provides a mono-energetic source of electrons by thermionic emission. Focusing electrodes are employed to produce a narrow electron beam and a detector assembly is set to eliminate electrons that inelastically scatter from the sample. The energy of the bombarded electrons is varied from 50-500 eV in 1 eV increments.[80] Scattering intensities of the different diffraction beams are plotted as a function of energy. The highest intensities in the spectrum will occur for single scattering sites–atoms that represent the periodic Bragg condition.[82] Electron diffractions that occur from surface atoms vary due to the complicated nature of surfaces. However, the scattering spectra can be resolved with electronic scattering theory.[81]

LEED became a powerful tool in the 1970s when computational power and electronic structure theory converged such that it could accurately resolve the scattering spectra.[79,82] A spectrum is resolved by comparing the experimental spectrum with a series of theoretical scattering spectra with systematically varied atom positions.[83–85] The theoretical spectra can be calculated independent of the experiment. As such, most LEED software comes with a dataset of theoretical spectra. All structural variables are grouped into a single root-mean squared distance parameter, R_{LEED}, related to a given theoretical spectrum. A search through the dataset of theoretical spectrum is carried out to minimize the R_{LEED} parameter with respect to the experimental spectrum.[83,84] Surface analysis is

completed upon minimization of R_{LEED}. Improving R_{LEED} minimization increases the accuracy and the detail of LEED analysis.[85]

LEED analysis has been employed to study CVD of graphene on metal surfaces.[23,33,86] It has been used to show how monolayer growth evolves and gives a qualitative measure of the graphene-metal interaction strength.[28,87] Specific rotational and translational orientations of graphene, termed Moiré patterns, have also been resolved using LEED analysis.[34,88,89] LEED studies of graphene on metal surfaces are used in this thesis to confirm computationally-predicted stable orientations.

2.4 Atomic Force Microscopy (AFM)

Atomic force microscopy (AFM) can be used to measure the friction coefficient of surfaces.[90–94] An AFM friction study is relatively simple; an AFM needle on a cantilever is moved across a surface and the force of the interaction is measured.[91–93] The friction coefficient is determined from normal and lateral forces measured by the AFM needle. However, an AFM requires careful calibration to measure the friction coefficient.[92]

The normal force, F_N, between the tip and the sample is measured by the vertical displacement of the cantilever, Z_C:

$$F_N = k_C Z_C, \tag{2.4.1}$$

where k_C is the cantilever spring constant. Some studies also employ a piezoelectric cantilever beneath a sample that measures the substrate deformation during AFM scanning. This is not needed for hard substrates, like metals, where the cantilever force does not plastically deform the sample.[91] The cantilever spring constant depends on its shape and is generally calculated through inherent mate-

rial properties, such as its Young's modulus, Y_C (N/m^2):

$$k_C = \frac{Y_C w_C t_C^3}{4L_C^3}, \tag{2.4.2}$$

where L_C, w_C, and t_C and the length, width and thickness of the cantilever in meters.

Measuring frictional forces requires lateral scanning of a material's surface and measurement of the lateral forces. As the AFM scans across the surface, the cantilever has a lateral displacement, Z_l, and the lateral force is

$$F_l = k_l Z_l. \tag{2.4.3}$$

The lateral spring constant of the cantilever, k_l, is similar to k_c:

$$k_l = \frac{G_C w_C t_C^3}{4L_C^3}, \tag{2.4.4}$$

where G_C is the cantilever shear modulus.[91,93] As the AFM tip scans across the surface, the needle bends at an angle θ_C. The combined normal and lateral forces at the tip are

$$F_{\mathrm{AFM}} = F_l(\cos\theta_C + \sin\theta_C) + F_n(\cos\theta_C - \sin\theta_C). \tag{2.4.5}$$

As the AFM tip moves across the surface, the normal force changes by ΔF_N. The total of the lateral and normal forces measured as the AFM tip slides across the sample becomes

$$\begin{aligned} F_{\mathrm{AFM}} = \mu(F_N - \Delta F_N)\cos\theta_C - (F_N - \Delta F_N)\sin\theta_C + \\ \mu(F_N - \Delta F_N)\sin\theta_C + (F_N + \Delta F_N)\cos\theta_C. \end{aligned} \tag{2.4.6}$$

The friction coefficient, μ, is defined as $F_l/(F_N - \Delta F_N)$ and is averaged over two lateral passes, x and $-x$. Simplifying the previous expression and solving for the

friction coefficient yields

$$\mu = \frac{\Delta F_{N,x} + \Delta F_{N,-x}}{2F_N - \Delta F_{N,x} + \Delta F_{N,-x}} \frac{(-2L_t \sin\theta_C + L_C \cos\theta_C)}{(2L_t \cos\theta_C + L_C \sin\theta_C)}, \tag{2.4.7}$$

where L_t is the length of the AFM tip.

The method presented above is a generalization of how the friction coefficient of a surface can be measured using AFM.[90–94] Other approaches have been developed that determine the coefficient using different variables related to the cantilever shape and substrate-tip heights.[90] AFM frictional studies are cited in this thesis to measure the friction coefficient of graphene on metals and how it changes with the number of graphene layers.[41,43,95,96]

2.5 Quartz Crystal Microbalance (QCM)

The quartz crystal microbalance (QCM) is a tool that can measure masses of single monolayers. It is typically used to weigh molecule-sized masses on substrates,[97] but has been adapted to measure friction between weakly interacting systems,[97–100] such as noble gases on surfaces. A QCM consists of a single crystal of quartz, which has a natural vibration frequency ω_q. Upon adsorption of a molecule or film, the frequency changes by $\delta\omega_q$, which is related to the adsorbate's mass:

$$\frac{\delta\omega_q}{\omega_q} = -\frac{m_f}{m_q}, \tag{2.5.1}$$

where m_q is the mass of the quartz crystal and m_f is the mass of the adsorbate. The mass per area of the adsorbed film, ρ_f, can be related to the frequency shift:

$$\frac{\delta\omega_q}{\omega_q} = -\frac{\rho_f}{\rho_q t_q}, \tag{2.5.2}$$

where ρ_q is the density and t_q is the thickness of the quartz crystal.

Krim and Widom adapted QCM to measure frictional interactions between

substrates and adsorbents.[97,99,100] Atomically thin adsorbed films shift the quartz oscillation frequency and the quality factor, Q, a unit-less parameter that describes the resonance behavior of quartz oscillation. As a film moves across the quartz surface, Q and ω_q change proportionally to the film's characteristic slip time τ, the time it takes to move across a periodic length of a surface:

$$\delta(Q^{-1}) = -2\pi\tau\delta\omega_q. \tag{2.5.3}$$

In a QCM frictional study, Q and ω_q are simultaneously measured to calculate τ. The interfacial viscosity, η_f, describes the frictional interaction of the film on the surface and is calculated from τ and ρ_f:

$$\eta_f = \frac{\rho_f}{\tau}. \tag{2.5.4}$$

The frictional interaction is proportional to η_f; high values indicate large friction and low values indicate low friction.

QCM has been employed to study how molecular friction varies on different metal substrates and on graphene surfaces.[98] This thesis cites studies that have employed QCM to understand molecular friction on graphene surfaces. These studies were used as reference systems for comparing our results for substrate effects on interfacial graphene bilayer friction.[101,102]

Chapter 3: Electronic Structure Methods for Solids

A variety of electronic structure methods are employed in this thesis. This section begins by reviewing the foundations of periodic-boundary plane-wave pseudopotential methods. Post-processing methods that are used to characterize material-surface interactions are also explained.

3.1 Periodic Boundary Conditions and Plane Waves

The periodicity of a crystal allows one to study a bulk solid while only having to specifically define the positions of atoms contained in a single unit-cell. The periodicity can be represented by a Bravais lattice vector $\mathbf{T}$ composed of the crystal's primitive lattice vectors $\mathbf{a}$:

$$\mathbf{T} = n_1\mathbf{a}_1 + n_2\mathbf{a}_2 + n_3\mathbf{a}_3, \tag{3.1.1}$$

where n is an integer representing the number of lattice translations. A plane wave, $e^{i\mathbf{k}\cdot\mathbf{r}}$, can suitably describe the crystal's wave function, $\psi(\mathbf{r})$, because it satisfies the periodic Born-von Karman boundary condition:

$$\psi(\mathbf{r} + n\mathbf{a}) = \psi(\mathbf{r}). \tag{3.1.2}$$

Bloch's theorem[103] states that the electronic wave function obeys these conditions and can be written as the product of a plane wave and a one-electron potential $u_{\mathbf{k}}(\mathbf{r})$, which has the same spacial periodicity as the crystal lattice:

$$\psi_{\mathbf{k}}(\mathbf{r}) = e^{i\mathbf{k}\cdot\mathbf{r}}u_{\mathbf{k}}(\mathbf{r}). \tag{3.1.3}$$

The vector **k** relates an electron's momentum to a point in the crystal's reciprocal space. Using Bloch's theorem, the general form for a uniform crystal's wave function can be constructed as:

$$\psi_{\mathbf{k}}(\mathbf{r}) = e^{i\mathbf{k}\cdot\mathbf{r}} \sum_{\mathbf{G}} C_{\mathbf{k}+\mathbf{G}} e^{i\mathbf{G}\cdot\mathbf{r}}, \tag{3.1.4}$$

where **G** contains all the recirprocal lattice vectors and $C_{\mathbf{k}+\mathbf{G}}$ is a Fourier coefficient. Bloch's theorem[103] and the Born-von Karman boundary conditions are the foundation for plane-wave quantum mechanics.

3.2 K-Point Sampling and Integral Smearing

There exists an infinite number of **k** vectors in a crystal; however, only a minimal set of **k** vectors that adequately cover the crystal are needed to accurately sample the space. A sample of **k**-points within a crystal is known as a **k**-point mesh. As the number of **k**-points in a mesh approaches infinity, the trial wave function, $\psi_{\mathbf{k}}(\mathbf{r})$, approaches the real crystal wave function. Creating an efficient **k**-point mesh reduces computational cost without sacrificing accuracy.

A good **k**-point mesh should be uniformly distributed in **k**-space and ensures that a trial wave function is not biased in any coordinate plane. Choosing **k**-points at symmetrical points allows the number of **k**-points to be reduced while maintaining an accurate crystal sampling. This is the basis of Monkhorst-Pack **k**-point grids.[104] A crystal mesh can be rotated in **k**-space to maximize uniformity and increase symmetry, which reduces computational time. Because these properties largely depend on crystal geometry, most computational packages generate crystal-dependent **k**-point meshes on the fly.

The **k**-space discontinuities occur in metals between occupied and unoccupied states that require a large number of plane-waves to adequately reproduce the cusp between states. Smearing the discontinuity between states with a smoothing operator increases convergence with respect to the number of **k**-points. Quicker

convergence is achieved with high smearing, but usually at the expense of accuracy. An early smearing method is Fermi-Dirac smearing,[105] which models the discontinuity boundary as a Fermi-Dirac distribution function for a temperature T equal to σ/k_B, where σ is the smearing parameter and k_B is Boltzmann's constant. However, the presence of partially occupied states results in energies that are no longer variational.

A simpler method is Gaussian smearing,[106] which uses a Gaussian function to smooth the occupation numbers. Because of its simplistic mathematic formation, energies converge faster with respect to **k**-points, but like the Fermi-Dirac method, energies derived from Gaussian smearing are not variational. The Methfessel-Paxton method[107] is a more rigorous smoothing method than either Fermi-Dirac or Gaussian. This method expands the occupied states in terms of Hermite polynomials, allowing energies to vary less as integral smearing increases. However, it can produce unphysical negative occupied states. Marzari and Vanderbilt fixed this by multiplying the smearing function by a first order polynomial.[108]

Insulators and semiconductors do not require smearing because there is a smooth transition between occupied and unoccupied states. For metals that have few fragmented states at the Fermi energy cut-off, simple methods like Fermi-Dirac and Gaussian smearing are sufficient. For complex metallic states, where many states are partially occupied and fragmented by the Fermi energy cut-off, more rigorous smearing methods, like Methfessel-Paxton and Marzari-Vanderbilt, are required. The Marzari-Vanderbilt smearing method is used in all calculations reported here.

3.3 Atomic Pseudopotentials

A pseudopotential divides an atom into two energy regions: valence and core. Core-electron wave functions are frozen since they are not chemically active and are incorporated into an atomic valence wave function as an effective potential. The valence electron wave function then becomes the effective atomic wave func-

tion. Each pseudopotential is characterized by a core radius that originates at the nucleus and terminates at the boundary of the valence state. Norm-conserving pseudopotentials[109] hold that

$$\int_0^\infty |\phi_{\text{real}}(\mathbf{r})|^2 \mathbf{r}^2 d\mathbf{r} = \int_0^\infty |\phi_{\text{ps}}(\mathbf{r})|^2 \mathbf{r}^2 d\mathbf{r}, \tag{3.3.1}$$

where ϕ_{real} is an all-electron atomic wave function and ϕ_{ps} is the pseudopotential wave function. Norm-conservation is achieved by orthogonalizing core and valence states. This restriction ensures small changes in energy eigenvalues with atomic environment, allowing a single atomic pseudopotential for a given element to be used in many chemical environments.[109]

Norm-conservation creates a hard cutoff for p orbitals in first-row elements and d orbitals in transition metals because there are no core states with equal angular momentum to impose orthogonality with the valence state. The norm-conserving pseudopotential valence wave function for these elements is nodeless, requiring a large number of plane waves to adequately describe the total electron potential for these elements. Vanderbilt proposed[110] that relaxing the charge-conservation constraint of the core region allows core wave functions to indirectly interact with the valence wave functions via an overlap matrix. This "softens" the cut-off between the core and valence region, lowering the wave function energy cut-off and reducing the number of needed plane waves. This allows core functions to be indirectly expanded in the plane-wave basis set, increasing accuracy and reducing computational time.

3.4 The Projector Augmented Wave (PAW) Method

The projector augmented wave (PAW) method is a hybrid plane-wave and atomic pseudopotential method. It is conceptually based on Slater's augmented plane wave (APW) method[111] where the total wave function within a crystal is divided into two sections: an intra-atomic region and an inter-atomic continuum.

The intra-atomic region is modeled as an atomistic radial function with a radius $\mathbf{R}$; outside the atomic region $\mathbf{R}$, the wave function is represented as a linear combination of plane waves $e^{i\mathbf{G}\cdot\mathbf{r}}$. At the boundary of the atomic region, the plane wave and atomic radial functions must equal each other. However, self-consistent convergence of the APW equations is slow. These convergence problems were fixed in the linear augmented plane wave (LAPW)[112] method by including energy derivatives at the edge of the atomic region. The orthogonal plane wave (OPW) method[113] divides the atomic region into core and valence regions. Core wave functions are well localized about lattice sites, like in augmented wave methods, while the valence region is described by plane waves. The total wave function is then constrained to be orthogonal to the core wave function.

The PAW[114] method combines pseudopotential methods with augmented plane wave methods. LAPW and OPW schemes have rapid oscillations near the atom's valence boundary that are computationally intensive to evaluate. The PAW method transforms these oscillating functions into smooth functions that are easier to evaluate, reducing computational wall time. Using a linear transformation, the all-electron wave-function can be reconstructed from a smooth pseudo wave function ψ_{ps}:

$$|\psi_{\text{real}}\rangle = \widehat{T}\,|\psi_{\text{ps}}\rangle\,, \tag{3.4.1}$$

where the linear function $\widehat{T}$ is defined as

$$\widehat{T} = 1 + \sum_{i}^{N} (|\phi_{\text{real},i}\rangle - |\phi_{\text{ps},i}\rangle)\,\langle p_i|\,. \tag{3.4.2}$$

The projection function $\langle p_i|$ projects the pseudo wave function on to the all-electron wave function. There are several advantages to PAW. Foremost, it combines the accuracy of augmented wave methods, but reduces the required number of plane waves. Its formalism allows easy implementation of popular exchange-correlation functionals in electronic structure programs. Because of its accuracy

and efficient computational performance, PAW is one of the most popular plane wave methods and is the chosen DFT framework used in this work. All calculations presented here use Kresse and Joubert's version of PAW potentials.[115]

3.5 Charge Transfer

Atomic charge is not a uniquely defined observable of a typical DFT calculation. Instead, it is determined via the converged electron density. Bader proposed in his quantum theory of atoms in molecules (QTAIM)[116] that the total electron density can be partitioned into atomic basins. These atomic basins are defined as the region within a zero-flux surface such that $\nabla\rho(\mathbf{r}) \cdot v_{\mathbf{r}} = 0$, where $v_{\mathbf{r}}$ is a unit vector perpendicular to the surface at $\mathbf{r}$.[117] Atomic volumes and charges can then be computed through numerical integration over each atomic basin.

The numerical method used to calculate atomic charges in this paper is one created by Yu and Trinkle.[118] It uses a weighted grid approach to determine the atomic volumes and charges from the density. In standard grid approaches, a volume grid is overlaid onto the set of zero-flux surfaces. The sum of grid volumes associated with an atom yields an atomic Bader volume. A threshold is set, based on the percentage of an atom's zero-flux surface, to either add or neglect the addition of the grid volume to the total atomic Bader volume. In contrast, a weighted grid approach accounts for all grid volume contributions where a zero-flux surface is present, but contributions are scaled based on the percentage of zero-flux surface in the grid volume.

Charge transfer is defined as the difference in atomic charge before and after molecular surface adsorption. The magnitude of charge transfer provides insight into the type of adsorption interactions occurring between a molecule and surface.

Chapter 4: Density-Functional Theory (DFT) and Dispersion Corrections for Modeling Physisorption

Using local or semi-local density functionals alone is not suitable to model 2D materials on metal substrates as they neglect London dispersion interactions, which contribute a significant portion to the adsorption energy.[56–61] This section reviews four functional classes and four types of popular dispersion corrections. It concludes with an overview of the exchange-hole dipole moment (XDM) model[60,61] of dispersion, which is the density-functional dispersion-correction method used in this thesis.

4.1 The Local Density Approximation (LDA)

The local density approximation (LDA) is the earliest density functional.[119] In the LDA approximation, the exchange-correlation energy depends solely upon the value of the electron density at each point in space. The LDA expression for the exchange energy is:

$$E_x^{\mathrm{LDA}}[\rho] = -\frac{3}{4}\left(\frac{3}{\pi}\right)^{(1/3)} \int \rho(\mathbf{r})^{4/3} d\mathbf{r}, \tag{4.1.1}$$

where $\rho(\mathbf{r})$ is the electron density. There is no analytical expression for the LDA correlation contribution. However, Ceperley and Alder computed a numerically fitted function for LDA correlation that, due to the function's nature, will not be printed here.[120]

The LDA provides a reasonable description of bond lengths and adsorption energies for many van der Waals layered systems, such as graphite. Although the

LDA returns reasonable energies and geometries, the results arise from cancellation of errors. Dispersion interactions modeled in LDA arise from the exchange functional and not from a physically correct treatment of long-range correlation. For chemisorbed molecules that have both covalent and dispersion energy contributions, the LDA usually predicts relatively accurate adsorption energies because covalent-binding contributions are over-stabilized.[121,122] However, LDA typically overestimates adsorption energies and underestimates bond lengths. For example, Liu *et al.* used the LDA to investigate benzene on gold and platinum and found it to overestimate the covalent binding of benzene on platinum (adsorption energy 2.30 eV predicted, 1.57 eV expt.[123]), while underestimating the physisorption energies of benzene on gold (0.49 eV predicted, 0.73 eV expt[124]).[47]

4.2 The Generalized Gradient Approximation (GGA)

The generalized gradient approximation (GGA) is an improvement over the LDA for general thermochemistry because it includes contributions from the density gradient. A GGA functional has the general form of

$$E_{XC}^{\mathrm{GGA}}[\rho] = \int d\mathbf{r} f[\rho, \nabla\rho]. \tag{4.2.1}$$

The exchange contribution is modeled as

$$E_{X}^{\mathrm{GGA}} = \int d\mathbf{r} \epsilon_{X}^{\mathrm{unif}}[\rho(\mathbf{r})] F_X(s), \tag{4.2.2}$$

where $\epsilon_X^{\mathrm{unif}}$ is the exchange contribution from a uniform electron gas. $F_X(s)$ is the enhancement factor dependent on the reduced density gradient, s, defined as $|\nabla\rho|/\rho^{4/3}$. It has been shown that GGA ionization potentials, electron affinities, and optimized geometries are generally more accurate than with the LDA.[47,125]

The correlation contributions are

$$E_C^{\mathrm{GGA}}[\rho] = \int d\mathbf{r}\rho[\epsilon_C^{\mathrm{unif}}(\rho,\zeta)] + H(\rho,\zeta,\nabla\rho)]. \tag{4.2.3}$$

The correlation energy is split into two contributions, the energetic contribution from a uniform electron gas ϵ_C^{unif}, and the gradient contribution H, which is dependent on the electron density, density gradient, and the relative spin polarization ζ.[126] Molecular adsorption energies are also more accurate than with the LDA for strong covalent or ionic binding. However, GGAs lack a proper description of the non-local correlation effects needed to describe dispersion interactions and do not exhibit the same error cancelation as the LDA.[60,61] Therefore, GGAs fail to adequately predict adsorption energies for physisorbed molecules. Calculated adsorption energies of benzene on platinum and gold surfaces using the PBE functional in a study by Liu *et al.* were significantly less than experimental values: 0.81 eV for benzene/platinum (1.57 expt.[123]) and 0.15 eV for benzene/gold (0.73 eV expt[124]).[47]

4.3 The Random Phase Approximation (RPA)

The random phase approximation (RPA) is a framework to calculate electronic correlation energies.[127] Though it is considered to be a DFT method, the RPA correlation energy is not calculated in the Kohn-Sham framework, as for the LDA or GGA functionals.[55] Instead, the method calculates the correlation energy through the interactions of fluctuating densities with different frequencies ω, represented by the density-density response function $\chi(\mathbf{r},\mathbf{r},i\omega)$.[55,127–130] The RPA correlation energy is calculated by evaluating

$$E_C[\rho] = \frac{1}{2\pi}\int_0^1 d\lambda \int_0^\infty d\omega \int d\mathbf{r}d\mathbf{r}' \frac{\chi_\lambda(\mathbf{r},\mathbf{r}',i\omega) - \chi_0(\mathbf{r},\mathbf{r}',i\omega)}{|\mathbf{r}-\mathbf{r}'|}, \tag{4.3.1}$$

where λ is the interaction strength. The density fluctuations are non-interacting when $\lambda = 0$ and fully interacting when $\lambda = 1$.

The density-density response function can be formulated using a variety of electronic structure methods. Approaches that have been used to calculate the RPA correlation energy are many-body Green's functions, time-dependent density-functional theory, and coupled-cluster theory.[127,130] RPA has gained a resurgence in the last two decades because it is a parameter-free method and recovers the $1/R^6$ asymptote required to model van der Waals interactions.[131] However, RPA-based methods are computationally expensive compared to LDA and GGA functionals because they require the inclusion of excited states. RPA calculations scale as $O(N^6)$,[128] but recent implementations have reduced the cost to $O(N^4)$.[127,132] RPA methods also require using Kohn-Sham orbitals generated with LDA or GGA functionals and have not been implemented self-consistently.[130]

It has been shown that both the interactions between noble-gas atom pairs and graphite exfoliation energies can be accurately calculated with respect to experimental data.[39] Because of its accuracy and parameter-free formalism, RPA energies are used to benchmark DFT dispersion correction methods.[131] Reported RPA energies are used for comparison to those reported in this thesis.

4.4 The Non-Local van der Waals Density Functional (vdW-DF)

In order to properly describe dispersion interactions, functionals based on GGAs have been developed with specific non-local energy contributions. These functionals, classified as vdW-DF functionals, split the correlation contribution into local and non-local contributions:[133]

$$E_{XC}[\rho] = E_X^{\mathrm{GGA}}[\rho] + E_C^{\mathrm{LDA}}[\rho] + E_C^{\mathrm{nl}}[\rho]. \tag{4.4.1}$$

The non-local contribution, E_C^{nl}, is evaluated as

$$E_C^{\mathrm{nl}} = \frac{1}{2}\int d\mathbf{r}d\mathbf{r}'\rho(\mathbf{r})f(\mathbf{r},\mathbf{r}')\rho(\mathbf{r}'), \tag{4.4.2}$$

where $f(\mathbf{r},\mathbf{r}')$ is the vdW-DF kernel, an analytical function based on density-fluctuation theory.[122,134] E_C^{nl} has been paired with several popular GGAs, such as PBE.[126] Carter and Rohl systematically investigated adsorption energies of benzene on copper using several vdW-DF functionals.[135] Their results show that vdW-DF functionals recover much of the required non-local correlation contributions lost by their corresponding GGA functionals (e.g. -0.06 eV revPBE, 0.40 eV for revPBE-DF and 0.59 eV expt.[136])[135] Toyoda *et al.* also had much success investigating adsorption energies for pentacene on noble metals with vdW-DF, predicting an adsorption energy of 1.47 eV for pentacene/copper compared to an experimentally predicted value of 1.6 eV.[137,138]

4.5 The Grimme Density-Functional Dispersion Correction (DFT-D)

The simplest approach to account for dispersion interactions is to add an energy correction to the converged DFT energy. The concept of a dispersion-energy correction was first proposed by Ahlrichs, Penco and Scoles, who used semi-empirical dispersion coefficients to correct Hartree-Fock energies.[139] The magnitude of this correction is determined via an analytical function. Grimme created a similarly-framed dispersion correction for DFT where a set of empirically-fit homoatomic dispersion coefficients are employed to calculate averaged pairwise dispersion interactions.[140] The dispersion energy has the form:

$$E_{\mathrm{disp}} = -s_G \sum_{i=1}^{N_{at}-1}\sum_{j=i+1}^{N_{at}} \frac{C_6^{ij}}{R_{ij}^6} f_{\mathrm{damp}}(R_{ij}). \tag{4.5.1}$$

Molecular dispersion coefficients C_6^{ij} are calculated as a simple average of homoatomic dispersion coefficients:

$$C_6^{ij} = 2\frac{C_6^{ii}C_6^{jj}}{C_6^{ii} + C_6^{jj}}. \tag{4.5.2}$$

The weight of the dispersion contribution C_6^{ij}/R_{ij}^6 is determined by a global scaling factor s_G, as well as a damping function $f_{\text{damp}}(R_{ij})$, which ensures that the dispersion correction is not unphysically applied at small internuclear separations:

$$f_{\text{damp}}(R_{ij}) = \frac{1}{1 + e^{-s_G(R_{ij}/R_0 - 1)}}. \tag{4.5.3}$$

R_0 is the dispersion cut-off radius. Grimme's DFT-D provided a large improvement to standard GGA functionals, but due to its empiricism, lacks accuracy for applications where molecules are dissimilar to those in the fit set.[56]

Transferability of the dispersion correction method to encompass the entirety of the periodic table was reached in the DFT-D2 model.[57] Each homoatomic dispersion coefficient is determined empirically as

$$C_6^{ii} = 0.05 C_G I_p \alpha_i \tag{4.5.4}$$

and the two-body dispersion coefficients are

$$C_6^{ij} = \sqrt{C_6^{ii}C_6^{jj}}. \tag{4.5.5}$$

This model provided better values for small-large atom-pair dispersion coefficients. The homo atomic dispersion coefficient is a function of the atomic ionization potential I_p and the static free atomic polarizability α. C_G is a fitted constant dependent on the row of the periodic table for an element. Despite success for molecular dimers, the DFT-D2 method has been found to over-bind molecules to metal surfaces.[141]

A third iteration of DFT-D (DFT-D3)[56] is a variable-C_6 approach using com-

puted atomic polarizabilities, allowing the dispersion correction to change depending on the chemical environment. The dispersion coefficient between atoms i and j is related to the polarizability of their analogous elemental hydrides, $\mathrm{I}_m\mathrm{H}_n$ and $\mathrm{J}_k\mathrm{H}_l$. The DFT-D3 dispersion energy is defined as:

$$C_6^{ij} = \frac{3}{\pi}\int_0^\infty \mathrm{Im}d\omega \frac{1}{m}\left(\alpha^{\mathrm{I}_m\mathrm{H}_n}(\omega) - \frac{n}{2}\alpha^{\mathrm{H}_2}(\omega)\right)\cdot\frac{1}{k}\left(\alpha^{\mathrm{J}_k\mathrm{H}_l}(\omega) - \frac{l}{2}\alpha^{\mathrm{H}_2}(\omega)\right), \quad (4.5.6)$$

where α is the atomic polarizability and m, n, k, l are stoichiometric factors. The constant α^{H_2} is the polarizability of molecular hydrogen. The D3 correction also includes a higher-order two-body C_8 dispersion term:

$$C_8^{ij} = 3C_6^{ij}\sqrt{Q^{ii}Q^{jj}} \quad (4.5.7)$$

where Q^i is:

$$Q^{ii} = \sqrt{Z^i}\frac{\langle M^4\rangle^{ii}}{\langle M^2\rangle^{ii}}. \quad (4.5.8)$$

The terms $\langle M^4\rangle$ and $\langle M^2\rangle$ are multipole expectation values and Z is the atomic nuclear charge. Three-body corrections can be included in D3, if needed, and are approximated to be:

$$E^{ijk} = \frac{C_9^{ijk}(3\cos(\theta_i)\cos(\theta_j)\cos(\theta_k)+1)}{(R_{ij}R_{jk}R_{ki})^3} \quad (4.5.9)$$

with the three-body dispersion coefficients represented as:

$$C_9^{ijk} = -\sqrt{C_6^{ij}C_6^{ki}C_6^{jk}}. \quad (4.5.10)$$

Both two and three-body energy corrections are damped with a function that depends on the fitted constants, s_1 and s_2, and the order of the dispersion constant,

n:

$$f_{\mathrm{damp},n}(R_{ij}) = \frac{1}{1 + 6(R_{ij}/(s_{1,n}R_0))^{-s_{2,n}}}. \tag{4.5.11}$$

The cut-off radii, R_0, and the inter-atomic distances, R_{ij}, are either the two-body distances or averaged three-body distances. The constants, s_1 or s_2, scale the dispersion coefficient depending on the order, n, of the dispersion term.

DFT-D3 adsorption energies are more accurate than DFT-D and DFT-D2 energies. For thiophene adsorption on copper, Callsen and co-workers compared DFT-D2 and DFT-D3 thiophene/copper adsorption energies and demonstrated that the D2 correction overestimates the molecular adsorption energy (1.02 eV), while the D3 adsorption energy (0.61 eV) was in good agreement with experiment (0.59 eV[142]).[141]

4.6 The Tkatchenko-Scheffler van der Waals Correction (vdW-TS)

Another variable-C_6 DFT dispersion-correction is the vdW-TS method proposed by Tkatchenko and Scheffler.[58] In this method, the heteroatomic dispersion coefficients are approximated as follows:

$$C_6^{ij} = \frac{2C_6^{ii}C_6^{jj}}{\left(\frac{\alpha^j}{\alpha^i}C_6^{ii} + \frac{\alpha^i}{\alpha^j}C_6^{jj}\right)}, \tag{4.6.1}$$

where C_6^{ii} is the homoatomic dispersion constant and α is the atom-in-molecule polarizability. Atom-in-molecule dispersion coefficients are obtained by scaling the free-atomic dispersion coefficients, using a relation between atomic polarizability and volume:

$$C_{\mathrm{eff},6}^{ii} = \left(\frac{V_{\mathrm{eff}}^i}{V_{\mathrm{free}}^i}\right)^2 C_{6,\mathrm{free}}^{ii}. \tag{4.6.2}$$

V_{free} is the volume of the free atom. The effective atomic volumes, V_{eff}, are computed via Hirshfeld partitioning of the electron density. Within the vdW-TS framework, three-body terms are essential to properly describe dispersion interactions.[143] The three-body dispersion coefficient is defined as:

$$C_9^{ijk} = \frac{8}{3}\frac{P_i P_j P_k (P_i + P_j + P_k)}{(P_i + P_j)(P_j + P_k)(P_k + P_i)} \tag{4.6.3}$$

where

$$P_i = C_{9,\text{free}}^{iii}\left(\frac{V_{\text{eff}}^i[\rho_{\text{eff}}(\mathbf{r})]}{V_{\text{free}}^i[\rho_{\text{free}}(\mathbf{r})]}\right)^3 \frac{\alpha_j \alpha_k}{\alpha_j^2}. \tag{4.6.4}$$

The three-body energy equation is the same as in Grimme's DFT-D3.[57] However, the damping functions are quite different from DFT-D3. The two-body damping function $f_{\text{damp}}(R_{ij})$ is defined as

$$f_{\text{damp}}(R_{ij}) = 1 - e^{-b_{\text{TS}}^{ij} R_{ij}} \sum_{k=0}^{n=6} \frac{(b_{\text{TS}}^{ij} R_{ij})^k}{k!}, \tag{4.6.5}$$

where b_{TS} is a range parameter that reflects the atom-pair size. The three-body damping function is simply the product of the three combinations of the two-body damping functions:

$$f_{\text{damp}}(R_{ijk}) = f_{\text{damp}}(R_{ij}) \times f_{\text{damp}}(R_{ik}) \times f_{\text{damp}}(R_{jk}). \tag{4.6.6}$$

It has been shown that vdW-TS overestimates molecular-surface adsorption energies because it does not adequately compute dispersion coefficients between surface atoms and molecules.[124]

A more accurate C_{ij}^6 coefficient for surface atoms is created by scaling it using the Lifshitz-Zaremba-Kohn (LZK) theory for van der Waals interactions between an atom and a solid surface.[144,145] LZK theory states that the dispersion coefficient

between a solid's surface and a molecule is

$$C_3^{ij} = \frac{\hbar}{4\pi}\int_0^\infty d\omega \alpha^i \frac{\epsilon_B^j(i\omega)-1}{\epsilon_B^j(i\omega)+1}, \tag{4.6.7}$$

where $\epsilon_B^j(i\omega)$ is the solid's dielectric function and is taken from experiment. From this, the two-body dispersion coefficient between a molecule and a surface atom, $C_{6,\mathrm{LZK}}^{ij}$, can be determined as

$$C_3^{ij} = n_s\left(\frac{\pi}{6}\right) C_{6,\mathrm{LZK}}^{ij}, \tag{4.6.8}$$

where n_s is the number of atoms per unit volume in the bulk. The heteronuclear interaction is decomposed into homonuclear terms as

$$C_{6,\mathrm{LZK}}^{ij} = \frac{2C_6^{ii}C_{6,\mathrm{LZK}}^{jj}}{\frac{\alpha_{\mathrm{LZK}}^j}{\alpha^i}C_6^{ii} + \frac{\alpha^i}{\alpha_{\mathrm{LZK}}^j}C_{6,\mathrm{LZK}}^{jj}}. \tag{4.6.9}$$

Both α_{LZK}^j and $C_{6,\mathrm{LZK}}^{jj}$ are constant for a solid. These constants are determined through a system of equations using vdW-TS gas-phase molecular dispersion coefficients and polarizabilities (C_6^{ii} and α^i) and from $C_{6,\mathrm{LZK}}^{ij}$, which is calculated from Equation 4.6.8. Once α_{LZK}^j and $C_{6,\mathrm{LZK}}^{jj}$ are determined, $C_{6,\mathrm{LZK}}^{ij}$ for any molecule will vary by way of a molecule's environment dependent C_6^{ii} and α_0^i. Surface adsorption energies from LZK-corrected dispersion coefficients are more accurate. For benzene on gold, vdW-TS$^{\mathrm{surf}}$ predicts an adsorption energy of 0.74 eV, close to the experimental value of 0.73 eV.[47]

4.7 The Many-Body Dispersion (MBD) Correction

The many-body dispersion (MBD) correction[62,63,146] of Tkatchenko and coworkers is a DFT dispersion correction based on the RPA.[62] It models an atom as a quantum harmonic oscillator with a frequency ω_{MBD}. The polarizability of

atom i is equal to the vdW-TS polarizability, α_i^{TS}. The polarizability of atom i in the presence of atom j is calculated using the self-consistent screening equation:[63]

$$\alpha_i^{\mathrm{SCS}} = \alpha_i^{\mathrm{TS}} + \alpha_i^{\mathrm{TS}} \sum_{i \neq j}^{N} \Pi_{ij} \alpha_j^{\mathrm{SCS}}, \tag{4.7.1}$$

where Π_{ij} is the dipole interaction tensor. The long-range correlation energy is calculated by evaluating the MBD Hamiltonian:

$$\begin{aligned} H_{\mathrm{MBD}} = -\frac{1}{2} \sum_{i=1}^{N} \nabla_{\chi_i}^2 + \frac{1}{2} \sum_{i=1}^{N} \omega_{i,\mathrm{MBD}}^2 \chi_i^2 \\ + \sum_{i>j}^{N} \omega_{i,\mathrm{MBD}} \omega_{j,\mathrm{MBD}} \sqrt{\alpha_i^{\mathrm{SCS}} \alpha_j^{\mathrm{SCS}}} \chi_i \Pi_{ij} \chi_j, \end{aligned} \tag{4.7.2}$$

where χ_i is related to the mass and displacement of the quantum harmonic oscillator. Diagonalization of the interaction matrix yields a numerically exact solution to the Schrödinger equation. The dispersion interaction is then equal to the energy difference between the coupled and uncoupled quantum harmonic oscillators:

$$E_{\mathrm{MBD}} = \frac{1}{2} \sum_{i=1}^{3N} \sqrt{\lambda_i} - \frac{3}{2} \sum_{i=1}^{N} \omega_{i,\mathrm{MBD}}, \tag{4.7.3}$$

where λ_i is the eigenvalue to the solution of the MBD Hamiltonian. Papers[147,148] have shown that MBD gives accurate energies for benzene on noble metals, yielding an adsorption energy of benzene on Au (111) to be 0.67 eV (0.65 eV expt.)[148] Though MBD is an accurate method, it is more expensive than comparable DFT-D3 and XDM dispersion corrections, scaling as N^3 due to the required interaction matrix diagonalization.[63,146] Furthermore, accurate MBD results require the use of a hybrid-GGA functional, which is quite expensive to employ for solid-state calculations.[147,148]

4.8 The Exchange-Hole Dipole Moment (XDM) Model

The exchange-hole dipole moment (XDM) model is another post-SCF dispersion energy correction.[60,61] In XDM, dispersion interactions are modeled using the dipole moment between an electron and its corresponding exchange-hole as the source of the instantaneous dipole moments responsible for dispersion. Using second-order perturbation theory, the dispersion energy is defined as

$$E_{\text{disp}} = -\frac{1}{2}\sum_{n=6,8,10}\sum_{i<j}\frac{C_{n,ij}}{R_{ij}^{n}}f_{\text{damp}}(R_{ij}). \tag{4.8.1}$$

The dispersion coefficients, $C_{n,ij}$, are derived from atomic polarizabilities α_i, and the electron/exchange-hole multipole moments $\langle M_l^2\rangle_i$:

$$C_{6,ij} = \frac{\alpha_i\alpha_j\langle M_1^2\rangle_i\langle M_1^2\rangle_j}{\langle M_1^2\rangle_i\alpha_j + \langle M_1^2\rangle_j\alpha_i}, \tag{4.8.2}$$

$$C_{8,ij} = \frac{3}{2}\frac{\alpha_i\alpha_j\left(\langle M_1^2\rangle_i\langle M_2^2\rangle_j + \langle M_2^2\rangle_i\langle M_1^2\rangle_j\right)}{\langle M_1^2\rangle_i\alpha_j + \langle M_1^2\rangle_j\alpha_i}, \tag{4.8.3}$$

$$C_{10,ij} = 2\frac{\alpha_i\alpha_j\left(\langle M_{1\,i}^2\langle M_3^2\rangle_j + \langle M_3^2\rangle_i\langle M_1^2\rangle_j\right)}{\langle M_1^2\rangle_i\alpha_j + \langle M_1^2\rangle_j\alpha_i} + \frac{21}{5}\frac{\alpha_i\alpha_j\langle M_2^2\rangle_i\langle M_2^2\rangle_j}{\langle M_1^2\rangle_i\alpha_j + \langle M_1^2\rangle_j\alpha_i}. \tag{4.8.4}$$

All dispersion coefficients are computed from the electron density and are non-empirical. The series expansion for the dispersion-energy can be extended to include higher-order atomic coefficients, but is truncated because it has been shown that contributions beyond C_{ij}^{10} contribute little to the dispersion energy. The correction is damped using the interatomic van der Waals radii, R_{ij}^{vdW}, to prevent the dispersion energy from being unphysically large at short interatomic separations R_{ij}:

$$f_{\text{damp}}(R_{ij}) = \frac{R_{ij}}{R_{ij} + R_{ij}^{\text{vdW}}}, \tag{4.8.5}$$

where R_{ij}^{vdW} is defined as

$$R_{ij}^{\mathrm{vdW}} = a_1 R_{ij}^{c} + a_2. \tag{4.8.6}$$

R_{ij}^{c} is the critical radius for atomic dispersion interactions obtained using a ratio of the dispersion coefficients. The constants a_1 and a_2 are the only empirical parameters used in XDM. These parameters are fitted to minimize the mean absolute percent error for a set of 49 gas-phase dimers. Each density functional has a unique set of corresponding XDM damping parameters.

XDM has successfully been used to investigate metallophillic[149] interactions as well as molecular dimers[150] and crystals.[151] The purpose of this thesis is to demonstrate that the XDM dispersion correction accurately models surface dispersion interactions as demonstrated through modeling adsorption of molecules and graphene on metal surfaces.

Chapter 5: Surface Adsorption from the Exchange-Hole Dipole Moment Dispersion Model

Original reference: M. S. Christian, A. Otero-de-la-Roza, and E. R. Johnson, J. Chem. Theory Comput. **12**, 1049 (2016).

5.1 Abstract

The accurate calculation of intermolecular interaction energies with density-functional theory (DFT) requires methods that include a treatment of long-range, non-local dispersion correlation. In this work, we explore the ability of the exchange-hole dipole moment (XDM) dispersion correction to model molecular surface adsorption. Adsorption energies are calculated for six small aromatic molecules (benzene, furan, pyridine, thiophene, thiophenol, and benzenediamine) and the four DNA nucleobases (adenine, thymine, guanine, and cytosine) on the (111) surfaces of the three coinage metals (copper, silver, and gold). For benzene, where the experimental reference data is most precise, the mean absolute error in the computed absorption energies is 0.04 eV. For the other aromatic molecules, the computed adsorption energies are found to be within 0.09 eV of the available reference data, on average, which is well below the expected experimental uncertainties for temperature-programmed desorption measurements. Unlike other dispersion-corrected functionals, adequate performance does not require changes to the canonical XDM implementation, and the good performance of XDM is explained in terms of the behavior of the exchange hole. Additionally, the base functional employed (B86bPBE) is also optimal for molecular studies, making B86bPBE-XDM an excellent candidate for studying chemistry on material sur-

faces. Finally, the non-covalent interaction (NCI) plot technique is shown to detect adsorption effects in real space on the order of tenths of an eV.

5.2 Introduction

Molecule-surface interactions influence all processes that occur on the surface of a material. Modeling these interactions accurately is important in the study of topics as diverse as monolayer formation on metal surfaces,[152] construction of DNA microarrays,[153] molecular electronics,[154] and heterogeneous catalysis.[155] Molecular adsorption has been traditionally classified as a) chemisorption, which is relatively strong and where covalent interactions between molecule and substrate are predominant, and b) physisorption, which is dominated by weak non-covalent interactions. Chemisorption and physisorption also differ in the extent to which the electronic structure of the molecule and surface are disrupted at the adsorbed geometry. Chemisorption perturbs the surface band structure as well as the electronic energy levels of the adsorbate, whereas physisorption occurs through long-range effects that have little impact on the electronic levels. The nature of an adsorption event (chemisorption or physisorption) depends on the properties of both the molecule and surface. Simple aromatic molecules, such as benzene, thiophene, and pyridine are known to physisorb on noble-metal surfaces.[73,142,156–160]

Since long-range effects are essential to describe molecule-surface interactions, it is critical to have an accurate representation of dispersion forces when modeling physisorption and, to a lesser extent, chemisorption phenomena.[59,161] If dispersion models are included, quantum-chemical methods can be applied to complex systems, such as predicting polymorphic self-assembled monolayer structures in good agreement with experimental results.[162,163]

Accurately predicting physisorption geometries and energies with density-functional theory (DFT) is challenging because conventional functionals do not account for London dispersion interactions.[164,165] Indeed, previous physisorption studies using non-dispersion-corrected functionals yielded drastically underestimated ad-

sorption energies, relative to experiment.[141,166,167] The addition of a dispersion correction greatly increases the accuracy. Several recent studies have modeled physisorption with an assortment of dispersion-corrected functionals, including pairwise,[47,56,124,141,168–172] many-body,[148] and non-local[47,135,172–175] dispersion corrections. The majority of these studies focused on the adsorption of benzene on noble metals – copper, silver, and gold.[47,56,124,135,168–173,175]

Computational methods provide more detailed information regarding the nature of individual molecular-surface interactions than can be determined from experiments, which are complicated by differing molecule-surface interaction orientations, monolayer formation, and surface defects. Experimentally, molecular adsorption energies are generally measured via temperature-programmed desorption (TPD) analysis. The desorption energy is determined from the temperature of maximum desorption via Redhead's analysis.[66,72] This procedure is appropriate in the zero-coverage limit and where monolayers involve only weak intermolecular interactions. Since Redhead's analysis only accounts for intermolecular interactions through the pre-exponential factor, results can differ from actual adsorption energies.[68] In the particular case of benzene on coinage metals, Liu *et. al*[148] recently determined the adsorption energy of benzene using the complete analysis method, which is expected to be more accurate than the Redhead model. Benzene also does not have a coverage-dependent molecule-surface orientation below monolayer coverage. Hence, benzene on coinage metals is an excellent system to conduct benchmarking calculations of dispersion-corrected density functionals.

In this work, we present the first comprehensive performance study of the exchange-hole dipole moment (XDM) dispersion model[60] applied to molecular surface adsorption. XDM models the dispersion energy as a sum over all pairwise atomic interactions, with non-empirical, density-dependent dispersion coefficients, involving C_6, C_8, and C_{10} terms. When paired with suitable base density functionals, XDM has been demonstrated to be highly accurate for molecular dimers,[150] molecular crystals,[151] and graphene,[61] as well as for metallophilic interactions,[149]

without any system-specific re-parameterization. A study similar to this work was conducted by Chwee and Sullivan[170] for benzene on noble-metal surfaces,[170] where the authors successfully used a modification of XDM involving only the C_6 and C_8 terms, to calculate adsorption energies for benzene on noble metals. While their results show that XDM predicts suitable physisorption energies, the damping parameters used were taken from earlier work involving post-Hartree-Fock calculations[176] and are not expected to be generally applicable. In addition, several *ad hoc* modifications to the XDM method were used.

Previous works have suggested that simple pairwise methods[56,168] are not suitable for accurate calculation of physisorbed energies.[47,124,148,171,172] In this chapter, the canonical XDM implementation with the usual damping function parameters (determined for gas-phase dimers[61,150]) is used to demonstrate that a pairwise dispersion correction does not only represent molecule-surface interactions accurately, but it does so to an accuracy on par with previous estimates using either more complex dispersion corrections (including many-body effects) or purposely-built methods for molecule-surface interactions, such as vdW-TS$^{\text{surf}}$,[171,172] and at a computational cost that is comparable to a semi-local DFT calculation. The nature of the molecule-surface interactions is further analyzed using non-covalent interaction (NCI) plots,[177,178] where we demonstrate that NCI detects the minute energetic adsorption effects between molecule and substrate in real space. This chapter confirms that physisorption energies can be accurately calculated using the XDM dispersion model for single-molecule adsorption and that XDM is an excellent method for modeling chemical processes on material surfaces.

5.3 Computational Methods

Copper, silver, and gold (111) surfaces were modeled using (4×4) super-cells. The model surfaces were four atomic layers thick and a vacuum of 25 Å was inserted between each slab. The atomic positions of the two bottom layers were held fixed while the top two layers were allowed to relax. Our molecular test set

consisted of ten small aromatic molecules, including the four DNA nucleobases: benzene, furan, pyridine, thiophene, thiophenol, 1,4-benzenediamine (BDA), adenine, cytosine, guanine, and thymine. Each molecule was initially placed roughly 3 Å above the surface in a parallel position such that the aromatic region was centered over a surface atom and the geometry optimized. Additional calculations were performed for furan, pyridine, thiophene, and thiophenol, with the molecule initially placed perpendicular to the surface, such that the heteroatom was directly above a surface atom.

Periodic-boundary DFT calculations were performed using the pseudopotential plane-wave approach and the Projector Augmented Wave formalism.[114] Calculations were carried out using Quantum ESPRESSO[61,179] version 5.3.0 with the B86b[180] exchange functional and PBE[126] correlation, known to perform well in conjunction with XDM.[151] Additional XDM calculations with the PBE exchange-correlation functional[126] were performed for benzene adsorbed on the three metal surfaces for comparison with other literature results. PAW datasets were generated using LD1 version 4.3.2 using pslibrary 0.2.5 inputs. The datasets also included scalar relativistic effects and non-linear core corrections.[181] All datasets were checked to ensure that there was no PAW sphere overlap for each optimized geometry. The calculations used a 2×2×1 Γ-centered **k**-point grid, a plane-wave cutoff of 50 Ry and a density-expansion cutoff of 400 Ry, and cold smearing,[108] with a smearing parameter of 0.01 Ry. Subsequent single-point energy calculations with 4×4×1 **k**-points, as well as higher plane-wave and density-expansion cut-offs of 60 and 800 Ry respectively, were performed at the relaxed geometries. Results of convergence tests, with respect to the number of metal layers, **k**-point grid, and plane-wave cut-off are reported in Appendix A.

The XDM dispersion functional is a post-SCF correction to the base DFT energy, calculated using one of the usual semi-local functionals:

$$E = E_{\text{base}} + E_{\text{XDM}}, \tag{5.3.1}$$

$$E_{\mathrm{XDM}} = -\sum_{n=6,8,10}\sum_{i<j}\frac{C_{n,ij}f_n(R_{ij})}{R_{ij}^n}. \tag{5.3.2}$$

In this equation, the sum runs over all pairs of atoms i and j in the system. R_{ij} is the interatomic distance, f_n is a damping function that reduces the dispersion correction at short range, and the $C_{n,ij}$ are pairwise dispersion coefficients. In the XDM model, each $C_{n,ij}$ is approximated non-empirically via second-order perturbation theory using the multipole moments of a reference electron and its exchange hole and atom-in-molecule polarizabilities for the interacting atoms.[60] The XDM dispersion model offers excellent accuracy for both gas-phase[150] and condensed-matter[61,151] systems, notably including the interactions between noble-metal complexes.[149]

The adsorption energy is defined as the difference between the calculated energy of the adsorbed molecule and the energies of the bare surface and isolated molecule:

$$E_{\mathrm{adsorption}} = E_{\mathrm{surf}} + E_{\mathrm{molec}} - E_{\mathrm{complex}}. \tag{5.3.3}$$

The contributions of image interactions[135] on E_{molec}, arising from the use of periodic boundary conditions, were evaluated by calculating the molecular energy in two configurations. First, energies were calculated for each molecule in a large vacuum to nullify any self-interactions. Second, E_{molec} was calculated for an isolated molecule in a cell with the same dimensions as the surface unit cell. The results are compared in Appendix A. For the six small aromatic molecules, the energy differences between these two definitions were negligible, with the largest variations of 0.03 eV occurring for thiophene and 1,4-benzenediamine (*cis*). However, image interactions for the nucleobases were found to be as large as 0.10 eV, due to their greater molecular sizes and polarities. In order to eliminate the effect of these image interactions, all adsorption energy results are reported relative to a periodic array of molecules with the same cell dimensions as for the physisorbed complex.

Non-covalent interaction (NCI)[177,178] plots at the optimized adsorption geom-

etry were generated using the Critic2 program[182] to investigate the nature of the interactions between the physisorbed molecules and the metal surfaces. The NCI index reveals non-covalent contacts based on the electron density and the reduced density gradient (RDG) defined as

$$s = \frac{1}{2(3\pi^2)^{1/3}} \frac{|\nabla\rho|}{\rho^{4/3}}. \tag{5.3.4}$$

This approach provides qualitative information about the presence and extent of non-bonded atomic contacts using isosurfaces of the RDG. These isosurfaces are defined to enclose regions with low density and low RDG that are a signature of non-covalent interactions.[177] Weak dispersion interactions typically appear as broad, green isosurfaces, while stronger directional non-covalent interactions (such as hydrogen bonds) appear as localized blue domains.

5.4 Results and Discussion

5.4.1 Benzene

Because abundant theoretical predictions and highly-precise experimental adsorption-energy results[148] are available, we focus first on the adsorption of benzene on the three metal surfaces. From the B86bPBE-XDM calculations, the benzene molecule adsorbs roughly parallel to the surface and the equilibrium distances between the nearest atoms in the benzene molecule and the metal surface are 2.71, 3.03, and 3.15 Å for copper, silver, and gold, respectively. The benzene-silver distance is in good agreement with the only available experimental measurement of 3.04±0.02 Å.[148] Table 5.4.1 compares our calculated adsorption energies with results from other dispersion methods in the literature, and with experimental results using complete analysis.[148]

In agreement with previous studies,[141,166,167] the PBE functional without any dispersion correction, predicts only extremely weak physisorption, with adsorption energies around 0.1 eV, compared to the experimental values of 0.65–0.69 eV.

Table 5.4.1: Comparison of reported adsorption energies for benzene on noble-metal surfaces in eV. The combination of base density functional and dispersion correction are noted in each case. The mean absolute error (MAE) is computed for the functionals for which the three adsorption energies have been reported.

Base Functional	Disp. Method	Cu	Ag	Au	MAE	Ref.
PBE	none	0.08	0.08, 0.09	0.08, 0.15	0.57–0.59	171, 172
PBE	D2	0.86	—	1.35	—	168
PBE	D3	0.99	0.74	0.86	0.19	169
PBE	D3(ABC)	0.79	0.61	0.73	0.08	169
PBE	vdW-TS	1.02, 1.07	0.82, 0.87	0.80, 0.84	0.20–0.25	171, 172
PBE	vdW-TS$^{\text{surf}}$	0.79, 0.86	0.73, 0.75	0.73, 0.74	0.08–0.11	171, 172
PBE	MBD	0.63	0.57	0.56	0.09	148
HSE	MBD	0.78	0.68	0.67	0.04	148
opt-B86b	vdW-DF	0.82	0.76	0.86	0.14	173
opt-B88	vdW-DF	0.74	0.72	0.82	0.09	173
opt-PBE	vdW-DF	0.68	0.71	0.71	0.03	173
revPBE	vdW-DF	0.53	0.55	0.56	0.13	173
rPW86	vdW-DF	0.49	0.52	0.55	0.15	173
SCAN	rVV10	0.74	0.68	0.73	0.04	175
PBE	XDM	0.54	0.58	0.61	0.10	This work
B86bPBE	XDM	0.59	0.68	0.64	0.04	This work
Expt.		0.69±0.04	0.68±0.05	0.65±0.03		148

Among the dispersion corrected functionals, the DFT-D2 dispersion correction to PBE causes an overestimation of the adsorption energies, particularly for benzene on gold.[168] This overestimation is likely due to a combination of the use of empirically-derived C_6 dispersion coefficients for the metal atoms (which in PBE-D2 are independent of the chemical environment) and, perhaps, to the omission of higher-order C_8 and C_{10} terms.

The more sophisticated DFT-D3 dispersion correction, in which the dispersion coefficients do depend on the adsorption geometry, shows improvement over D2, with a mean absolute error (MAE) of 0.19 eV. PBE-D3 improves upon PBE-D2 for silver[56] and gold,[169] but severely overestimates the adsorption energy for benzene on copper.[169] It has been argued that the overestimation of dispersion coefficients for metals with D3 may be due to the use of neutral hydrides with various coordination numbers as model systems and that improved coefficients

for metals could be obtained by changing the choice of reference.[183] The PBE-D3 result is further improved if a 3-body dispersion term is included, since the 3-body term is repulsive and serves to off-set the over-binding.[169]

The Tkatchenko-Scheffler (TS) dispersion method[58] also strongly overestimates adsorption of benzene to metals,[171,172] likely due to the free-metal-atom reference for the dispersion coefficients. A version of the TS method specifically designed for surfaces has been proposed[124] that recovers the C_3 dispersion coefficient for the metal surface.[145] In practice, this is achieved by scaling the dispersion coefficients, resulting in lower adsorption energies with a MAE of around 0.1 eV compared to the experimental values. The newer many-body dispersion (MBD) modification to the original TS method[62,63] accurately predicts the adsorption energies for benzene on the noble metals,[148] giving a mean absolute error of only 0.04 eV when combined with the range-separated hybrid functional HSE (which is considerably more computationally expensive than PBE).

Non-local van der Waals functionals[133,184] provide an alternative, non-empirical approach to model dispersion. Non-local functionals of the vdW-DF type display good performance for determining adsorption energies of benzene on noble metals.[135,172,173] While there is significant spread of the vdW-DF results depending on the choice of base functional, opt-B88, opt-PBE, and revPBE offer good agreement with experiment and all predict effectively degenerate adsorption energies for the three surfaces, in agreement with experimental observations. The performance of opt-PBE is particularly good with a mean absolute error of only 0.03 eV, within the precision of the experimental data. The SCAN meta-GGA combined with the non-local rVV10 dispersion correction[175] also performs quite well, with a MAE of 0.04 eV, again comparable to the experimental precision.

The adsorption energies calculated with XDM are generally lower than the other pairwise dispersion corrections. The adsorption energies are found to be nearly degenerate down the group, in agreement with the vdW-TS$^{\text{surf}}$ and MBD results. The B86bPBE functional provides better performance when paired with

XDM than does the PBE functional, in agreement with previous work.[151] This is to be expected given the improved behavior of the B86b exchange enhancement factor in the large reduced-gradient limit.[61,180,185] With a MAE of 0.04 eV, the B86bPBE-XDM adsorption energies are in comparable agreement with experiment as those obtained with the more computationally expensive HSE-MBD. B86bPBE-XDM also yields lower errors relative to vdW-TS$^{\text{surf}}$ and the vdW-DF functionals, except for opt-PBE, which shows superior performance.

It should be noted that the combination of B86bPBE and XDM performs well for physisorption without any modification or re-parameterization of the dispersion model and that the same functional has been shown to give accurate results for lattice energies of molecular crystals[61] and other non-covalently bound materials.[60] Hence, B86bPBE is a good candidate functional when adsorption on material surfaces is only one aspect of the system under study and a good representation of interactions between molecules on the surface is also necessary (e.g. heterogeneous catalysis, self-assembled monolayers, etc.).

5.4.2 Dispersion Coefficients: The Role of the Exchange-Hole Dipole Moment

In this section, we consider why the XDM model is capable of providing an improved treatment of surface adsorption relative to other pairwise dispersion corrections. In XDM, the C_6 (and higher-order) dispersion coefficients are determined from the atomic polarizabilities and integrals involving the exchange-hole dipole moment. Specifically, for a homonuclear pair of atoms, the C_6 dispersion coefficient is

$$C_{6,ii} = \frac{1}{2}\alpha_i \langle M_1^2 \rangle_i, \tag{5.4.1}$$

where

$$\langle M_1^2 \rangle_i = \sum_\sigma \int w_i(\mathbf{r}) \rho_\sigma(\mathbf{r}) \left[r - (r - d_{X\sigma}) \right]^2 . \tag{5.4.2}$$

Table 5.4.2: Free-atomic polarizabilities (α, in Å^3) for copper, silver, and gold. Also shown are the $\langle M_1^2 \rangle$ moments and the homoatomic C_6 dispersion coefficients (in atomic units) obtained for the bulk metal, the bulk metal chloride (MCl, in its fcc structure), the top layer of the metal surface, and the free atoms with XDM. The dispersion coefficients are compared with literature values for the bulk metal and free atoms from the vdW-TS$^{\text{surf}}$ model.[124]

Metal	α	$\langle M_1^2 \rangle$ XDM				C_6 XDM				C_6 vdW-TS$^{\text{surf}}$	
	free	bulk metal	bulk MCl	surf	free	bulk metal	bulk MCl	surf	free	bulk metal	free
Cu	6.2	5.27	6.82	6.19	9.71	103	130	120	180	59	253
Ag	7.2	7.30	9.79	9.19	15.64	179	226	221	351	122	339
Au	5.8	6.43	9.28	8.70	13.86	137	182	170	271	134	298

In these equations, $w_i(\mathbf{r})$ are the Hirshfeld partitioning weights;[186] $d_{X\sigma}$ is the dipole moment between the reference electron and its corresponding exchange hole, evaluated using the Becke-Roussel model;[187] and α_i is the atomic polarizability, evaluated by a volume scaling of the reference free-atomic polarizabilities.[188] Both the atomic polarizabilities and moment integrals show considerable dependence on the atomic environment, resulting in highly variable values for the dispersion coefficients.[189]

Table 5.4.2 shows the free-atom polarizibilities, as well as the dipole moment integrals and homonuclear dispersion coefficients for copper, silver, and gold. Values are reported for the free atoms, bulk metal, and surface, taken as the atoms in the top layer in the bare slab model used in the adsorption calculations. Literature C_6 values from the vdW-TS$^{\text{surf}}$ model[124] are also given for comparison. The computed XDM dispersion coefficients are larger than the analogous vdW-TS$^{\text{surf}}$ values for the bulk metals for copper and silver, although these values match XDM for gold.

The tabulated data shows that silver is more polarizable than copper and gold and therefore has larger dispersion coefficients. Relativistic effects increase the electronegativity of gold,[149] decreasing its polarizbiliy, and causing it to have dispersion coefficients closer to those of copper than silver.

The dispersion coefficients decrease considerably (by nearly a factor of one

half) going from the free atoms to the surface and bulk metal. This explains the over-binding tendency of other pairwise dispersion corrections (Table 5.4.1), which do not capture this large decrease in C_6 for the bulk metals. The decrease is not due to changes in the atomic volumes, which vary by less than 10%. Rather, Table 5.4.2 reveals that the difference in the dispersion coefficients originates from the exchange-hole dipole moment integrals.

The variation in the moment integrals can easily be understood by considering the nature of the exchange-hole in the valence region of a free atom compared to a bulk metal. In the free atom, the electron density decays exponentially and the exchange hole will remain centered on the atom, even when the reference electron is relatively far from the nucleus.[187] This results in large values of the exchange-hole dipole moment. Conversely, the electron density between two atoms in a metal remains quite flat,[190] causing the exchange hole to be centered very near the position of the reference electron.[187] Indeed, for a uniform electron gas, the exchange hole is centered exactly at the reference point. This results in small values of the exchange-hole dipole moment.

Table 5.4.2 also shows the calculated moments and coefficients for the metal in the rock-salt-type phase of the bulk metal chloride MCl (M = Cu, Ag, Au). This phase is the experimentally-observed structure of AgCl, and a metastable phase in AuCl and CuCl, and has been used in the past to explore the importance of metallophilic interactions in simple solids.[149] It is interesting to note that the crystallographic positions of the metal atoms are the same in the chloride as in the elemental metal. The critical influence of the atomic environment on the XDM moments, and hence on the dispersion coefficients, is clearly exemplified by comparing the elemental metals with the corresponding chlorides. The atomic volumes in the metal are larger than in the chloride (e.g. 128.5 bohr^3 in AuCl compared to 136.3 in Au metal). However, the XDM moments are smaller in the metal, because the exchange-hole dipole is significantly smaller and, in consequence, the metallic dispersion coefficients are lower.

We note that pairwise dispersion-correction methods such as DFT-D2 and the original Tkatchenko-Scheffler model, which depend on reference free-atom dispersion coefficients, will be unable to predict a greatly reduced C_6 for the bulk metal. The necessary physics to describe this variation in the dispersion coefficients is captured by the behavior of the exchange hole, but not by a simple volume scaling.

5.4.3 Comparison to Other Experimental and Theoretical Adsorption Energies

Table 5.4.3: Comparison of calculated adsorption energies (in eV) with available experimental data for selected molecules on copper, silver, and gold surfaces.

Molecule	Metal	Calc.	Expt.
Thiophene	Cu	0.66	0.66[142]
Thiophene	Ag	0.67	0.52[156]
Thiophene	Au	0.62	0.68[157]
Furan	Cu	0.53	0.43[158]
Pyridine	Cu	0.69, 0.86	0.53, 0.84[159]
1,4-BDA	Au	1.12	1.0[160]
MAE		0.09	

Table 5.4.3 shows a comparison of B86bPBE-XDM results with experimental TPD adsorption energies, where available. With the exception of the complete analysis results for benzene,[148] discussed previously, all of the TPD reference data will have fairly low precision. This occurs because the conversion of the temperature of maximum desorption to a desorption energy uses an empirically-chosen pre-exponential factor, typically taken to be 10^{13}/s.[72] Coverage-dependence of the pre-exponential factor[68] can introduce uncertainties of up to 0.2 eV for the molecules considered here. Additionally, some heteroaromatic molecules can adsorb in multiple stable configurations, resulting in a range of measured physisorption energies from TPD. For pyridine, the two reported experimental values[159] were compared with the computational results for the parallel and perpendicular orientations. The mean absolute error (MAE) is 0.09 eV, showing that the

XDM results agree with the reference values to within the expected experimental precision.

The case of 1,4-benzenediamine (BDA) on gold has also been studied using a vdW-DF functional by Li et al.[191] and will be discussed in more detail. For this system, an experimental adsorption energy of 1 eV was measured using temperature-dependent helium atom scattering.[160] BDA can adsorb to coinage metals in two geometries, where the amine groups on both sides of the phenyl ring are in relative *cis* and *trans* positions. Our calculated adsorption energies are 1.10 eV for *cis* and 1.12 eV for *trans* and both values are in good agreement with the experimental result. For comparison, PBE-vdW-DF gives 0.94 eV for the *trans* and 0.98 eV for the *cis* orientations,[191] closely matching our results and experiment. For the *trans* orientation, the tilt angle is predicted to be 8.4° with B86bPBE-XDM, in agreement with the optimal tilt angle of 8° found with PBE-vdW-DF.[191] This is significantly smaller than the angle of ca. 35° obtained with PBE in the absence of a dispersion correction.[191] Thus, dispersion causes the *trans* form of BDA to lie flatter on the surface. Interestingly, the "weak but non-negligible amine-Au bond" observed in previous studies[160,191] is revealed by an increased energetic contribution from the base functional in the *trans* configuration (Table 5.4.4) and also by the blue domains shown by the NCI plots in Figure 5.4.1. This same chemisorption effect is detected in the NCI plots for some of the other systems studied.

5.4.4 Molecular Trends: Dispersion Contributions and Non-Covalent Interaction Plots

The complete set of adsorption energies for the six small aromatic molecules with the three noble-metal surfaces is collected in Table 5.4.4, together with the XDM-dispersion and base-functional contributions. The dispersion contribution to the adsorption energies generally decreases down the group of coinage metals. Also, this energy decomposition shows that adsorption is entirely due to dispersion

Table 5.4.4: Calculated adsorption energies of selected molecules on the copper, silver, and gold surfaces, in eV. The contributions to the adsorption energies from the XDM dispersion correction and the base functional are also reported.

Molecule	Total			XDM			Base functional		
	Cu	Ag	Au	Cu	Ag	Au	Cu	Ag	Au
Benzene	0.59	0.68	0.64	1.01	0.85	0.75	-0.42	-0.17	-0.11
Furan	0.53	0.52	0.51	0.72	0.63	0.56	-0.19	-0.12	-0.05
Furan perp.	0.24	0.25	0.22	0.31	0.33	0.29	-0.08	-0.08	-0.07
Thiophene	0.66	0.67	0.62	0.90	0.77	0.69	-0.24	-0.11	-0.07
Thiophene perp.	0.40	0.40	0.25	0.49	0.47	0.32	-0.08	-0.07	-0.07
Thiophenol	1.00	0.90	0.91	1.15	1.05	0.90	-0.16	-0.15	0.01
Thiophenol perp.	0.35	0.36	0.33	0.44	0.39	0.34	-0.09	-0.03	-0.01
Pyridine	0.69	0.58	0.60	0.83	0.81	0.70	-0.14	-0.23	-0.09
Pyridine perp.	0.86	0.66	0.64	0.55	0.49	0.46	0.32	0.17	0.19
1,4-BDA (cis)	1.17	1.04	1.10	1.17	1.15	0.98	-0.01	-0.11	0.13
1,4-BDA (trans)	1.24	1.09	1.12	1.18	1.13	0.96	0.06	-0.04	0.16

interactions, with the two exceptions of pyridine, in the perpendicular orientation, and 1,4-benzenediamine, where bonding between the molecular lone pair and the surface can result in a non-negligible contribution to adsorption from the base functional. However, the total adsorption energy, even in these two cases with incipient chemisorption behavior, is still dominated by the dispersion contribution. Lone-pair–surface interactions will be discussed in detail throughout this section.

We now turn to the dependence of the absorption energies on molecular properties. We first consider the cases of benzene, furan, thiophene, and thiophenol, all of which prefer a parallel orientation to the surface such that dispersion interactions are maximized. The adsorption-energy trend for this series is furan $<$ benzene $<$ thiophene $<$ thiophenol, which can be attributed to increasing molecular size and polarizability. Additionally, the heteroatom lone pairs become softer across this series due to greater polarizabililty of sulfur in the thiols than oxygen and the change from an sp^2 sulfur in thiophene to an sp^3 sulfur in thiophenol.

Experimentally, benzene and furan have been found to bind parallel to the surface,[73,192,193] in agreement with our calculations. However, thiophene and thiophenol have coverage-dependent surface orientations. At low coverages, both molecules prefer a parallel surface orientation, maximizing dispersion interactions

Figure 5.4.1: NCI plots for selected molecules adsorbed on the gold surface using an $s = 0.6$ isosurface.

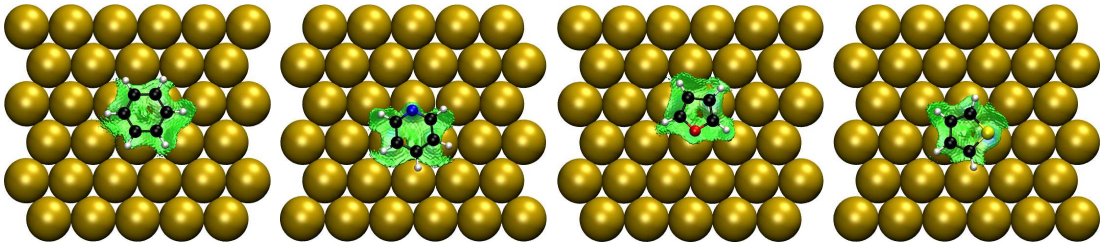

(a) benzene (b) pyridine (c) furan (d) thiophene

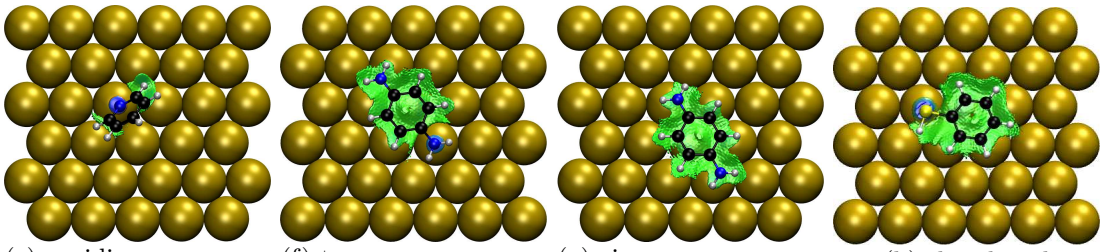

(e) pyridine perpendicular (f) trans p-benzenediamine (g) cis p-benzenediamine (h) thiophenol

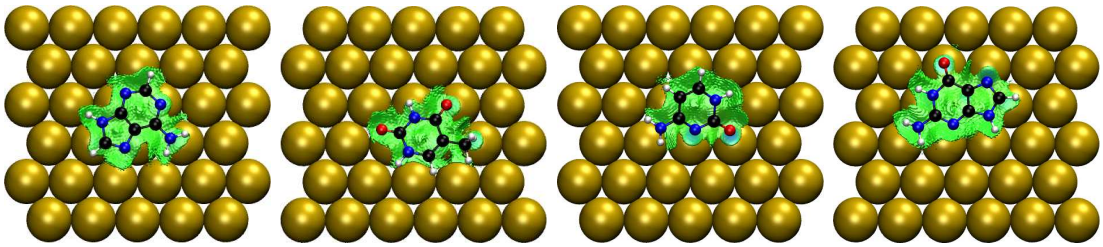

(i) adenine (j) thymine (k) cytosine (l) guanine

between the aromatic ring and the surface, but as the coverage increases, thiophene and thiophenol adopt perpendicular orientations where sulfur-surface interactions dominate.[142,193–195] Our calculations (Table 5.4.4) predict that the parallel orientations are energetically preferred over the perpendicular orientations, in agreement with experimental observations. However, the perpendicular orientations of thiophene and thiophenol are still energetically favorable, and the stabilization during monolayer formation can be attributed to the additional dispersion interactions between the adjacent π-stacked molecules and to the monolayer being more densely packed if the molecules are perpendicular to the surface.

NCI plots, shown in Figure 5.4.1 for the gold surfaces, provide additional insight into the nature of the molecule-surface interactions. Broad green isosurfaces in the NCI plots correspond to dispersion interactions between the aromatic ring and the surface. The plots clearly show that dispersion interactions are dominant, in agreement with the adsorption-energy decomposition in Table 5.4.4. Additionally, the increased adsorption for softer lone pairs can be clearly seen in the coloring of the NCI plots. For thiophene, the NCI surface directly under the sulfur lone pair is light blue, indicating a slight increase in interaction strength. For thiophenol, the bluer region of the NCI plot shows that the sulfur interacts with the surface even more strongly, reflecting the greater adsorption energy. This is consistent with the known strong adsorption of thiophenol to gold in self-assembled monolayers.[196,197] While the NCI plots show favorable interactions between the sulfur atoms and the surface, they are not strong enough to significantly tilt the molecules, which form angles of 7° or less with the surface in the parallel orientation. The adsorption geometries (distances and angles between the aromatic ring and the surface) are given in Appendix A.

Like thiophene and thiophenol, pyridine's orientation on metal surfaces is coverage-dependent.[159] At low coverages, pyridine prefers a parallel orientation where dispersion interactions dominate. As coverage increases, pyridine adopts a perpendicular orientation, interacting with the surface via the nitrogen lone pair

Figure 5.4.2: The polarization density for the physisorption of pyridine on a copper surface in the perpendicular orientation. The green iso-surface indicates an accumulation and the blue iso-surface depletion in electron density, for the adsorbed species relative to the separated molecule and surface at fixed geometries. The dipole of pyridine polarizes the surface, which induces further polarization of the nitrogen lone pair. This iso-density value is 0.016 a.u.

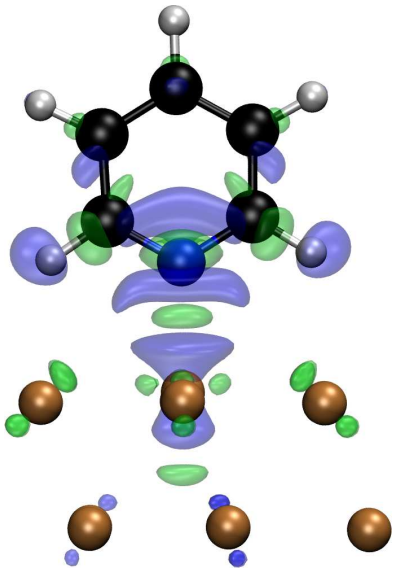

and the monolayer is further is stabilized by π-stacking.[159] In the parallel orientation, pyridine has an adsorption energy similar to benzene (see Table 5.4.4), which is dominated by dispersion. However, interactions between the nitrogen atom and the surface cause the molecule to tilt slightly.[198] The tilt angle is largest for the copper surface and is 24°, compared to 13° and 9° for Ag and Au, respectively. In the perpendicular orientation, the NCI plot shows the loss of dispersion interactions between the surface and the pyridine π-system and an increased interaction between the surface and nitrogen. Perpendicular pyridine has the largest density in the NCI regions of all the molecules considered here. Indeed, perpendicular pyridine is one of only two molecules predicted to adsorb on the surface by the base functional alone and the interaction energy is greatest for copper.

A plot of the polarization density, defined as the difference in electron density between the adsorbate and the isolated molecule and surface at fixed geometries, is shown for pyridine on the copper surface in Figure 5.4.2. In the perpendicular orientation, the dipole moment of pyridine is pointed directly down, towards the surface. This dipole polarizes the copper surface locally, inducing further polar-

ization of the adsorbed pyridine. The strength of this interaction for the silver and gold surfaces is found to be roughly equal to the extent of dispersion stabilization, such that the adsorption energies for perpendicular and parallel orientations are effectively equal. However, the results show that the perpendicular orientation of pyridine is favored for copper, where pyridine approaches the surface more closely. In this case, the induced electrostatic interactions become more favorable, as seen from the larger adsorption-energy contribution from the base functional (Table 5.4.4).

As discussed in the preceding section, 1,4-benzenediamine can adsorb as either a *cis* or *trans* isomer. Our results predict that the *cis* isomer has a weaker adsorption energy than the *trans* isomer. Adsorption of the *cis* isomer is entirely due to dispersion; it lies flat, with a near zero tilt angle and the amine hydrogens pointing down, towards the surface. As for perpendicular pyridine, a strong nitrogen-metal interaction appears in the NCI plot for the *trans* isomer and this results in a slightly tilted orientation on the surface with angles of 7-8°. Calculated adsorption energies for the *trans* isomer of BDA are approximately the sum of both perpendicular and parallel pyridine adsorption energies. The adsorption motif of *trans* BDA suggests that the *cis* isomer may adsorb more strongly if both nitrogen lone pairs were directed towards the surface, instead of away from it, as shown in Figure 5.4.1. However, the *trans* isomer experiences significant polarization, which is not possible in the *cis* isomer if both nitrogen lone pairs are directed towards the surface.

5.4.5 Nucleobases

Calculated adsorption energies for the nucleobases on the metal surfaces are given in Table 5.4.5. Our results show that adsorption is primarily driven by dispersion interactions. The dispersion energies follow the order cytosine < thymine < adenine < guanine, with greater molecular size leading to increased dispersion attraction. Adenine has a flat surface orientation since the nitrogen lone pairs all

conjugate with the π-system and have little direct interaction with the surface. Thymine has a slightly tilted geometry for copper and silver surfaces, but lies almost flat on gold, in agreement with STM images.[199,200] Conversely, cytosine and guanine adopt tilted geometries, at angles of 12-14° to the gold surface, each with the C=O group pointing slightly downward.

The NCI plots in Figure 5.4.1 offer a picture consistent with the adsorption geometries, showing that the oxygen atoms interact fairly strongly with the surface, in an analogous fashion to our results for *trans* 1,4-benzenediamine. Favorable interactions between the C=O groups and the surface also result in less repulsion from the base functional and the total adsorption energies follow the trend thymine < cytosine < adenine < guanine, though the ordering of cytosine and adenine are reversed for copper due to a stronger interaction of the oxygen atoms with this surface.

The calculated nucleobase adsorption energies are compared with experimental TPD adsorption for gold surfaces in Table 5.4.6. The computed adsorption energies are roughly half of those reported experimentally.[201,202] This is because the calculated energies correspond to the adsorption of a single, isolated molecule on the surface and lack the intermolecular interactions between adjacent nucleobases that are reflected in experiment, specifically hydrogen bonding. The experimental determination of single-molecule adsorption energies for nucleobases is difficult because of the formation of strong intermolecular hydrogen-bonds leading to the formation of molecular lines and clusters on metal surfaces, even at low coverages.[202] Since the TPD adsorption energies are measured for higher coverages, they contain contributions from intermolecular interactions within the monolayer[201–207] that must be included in the theoretical treatment as well. Note that these experimental values are also expected to have fairly large uncertainties given the high coverage sensitivity of Redhead analysis.[68]

To properly account for intermolecular hydrogen-bonding effects, periodic-boundary DFT calculations should be performed on a complete adsorbed mono-

Table 5.4.5: Calculated nucleobase adsorption energies for the copper, silver, and gold surfaces, in eV/molecule. The contributions to the total adsorption energies from the XDM dispersion correction and the base functional are also reported.

Molecule	Total			XDM			Base functional		
	Cu	Ag	Au	Cu	Ag	Au	Cu	Ag	Au
Guanine	1.07	1.03	0.94	1.22	1.14	1.00	-0.15	-0.11	-0.06
Cytosine	0.96	0.90	0.77	0.91	0.88	0.79	0.05	0.02	-0.02
Adenine	0.83	0.86	0.81	1.08	1.04	0.91	-0.25	-0.18	-0.10
Thymine	0.67	0.69	0.67	0.91	0.92	0.79	-0.24	-0.24	-0.12

Table 5.4.6: Comparison of calculated and experimental TPD adsorption energies for the nucleobases on the gold surface, in eV/molecule. The contribution of intermolecular hydrogen bonding is shown for both an estimated additive correction (Est.) and from the results of calculations on small nucleobase clusters (Calc.). The total DFT adsorption energies correspond to the sum of the single-molecule adsorption energies and these hydrogen-bond corrections.

Molecule	Surface	H-Bond		Total		Expt.
		Est.	Calc.	Est.	Calc.	
Guanine	0.94	0.86	0.84	1.80	1.78	1.44,[202] 1.51[201]
Cytosine	0.77	0.65	0.73	1.42	1.50	1.26,[202] 1.35[201]
Adenine	0.81	0.65	0.60	1.46	1.41	1.41,[202] 1.36[201]
Thymine	0.67	0.43	0.53	1.10	1.20	1.08,[202] 1.15[201]

layer. However, this presents considerable practical difficulty since the cell lengths corresponding to the monolayer and metal surface are not necessarily commensurate. Thus, to approximately account for intermolecular hydrogen-bonding, it was assumed that all possible donor and acceptor sites on the nucleobases would participate in hydrogen bonding, with an average strength of 0.22 eV (5 kcal/mol). Since two molecules are needed to form each hydrogen bond, this results in an energetic contribution of 0.11 eV (2.5 kcal/mol) per hydrogen-bond per molecule. The estimated hydrogen-bonding contributions are given in Table 5.4.6, considering that the four nucleobases can form four (thymine), six (cytosine and adenine), and eight (guanine) hydrogen bonds in total. Naturally, this is a rough estimate, but it serves to illustrate the origin of the missing stabilizing contribution.

As an alternative, approximate hydrogen-bond energies were also computed using the small nucleobase clusters whose structures are shown in Appendix A. These structures were chosen to match previous STM/DFT studies.[199,204,205,207] The calculations were performed with Gaussian09[208] using the LC-ωPBE[209,210] functional, XDM dispersion,[150] and the pc-2-spd basis set.[211] The results are given in Table 5.4.6 and show that the calculated and estimated hydrogen-bond contributions are in good agreement, and are generally on the same order as the single-molecule adsorption energies. Adding either of these hydrogen-bonding corrections gives total physisorption energies that are in good agreement with the experimental TPD values.[201,202]

5.5 Summary

This chapter investigated the ability of the XDM dispersion model to predict surface adsorption energies. Adsorption energies for a collection of molecules (benzene, furan, pyridine, thiophene, thiophenol, benzenediamine, and the four DNA nucleobases) on the (111) surfaces of coinage metals were calculated using the B86bPBE-XDM functional.

The adsorption energies are found to be dominated by dispersion interactions

and increase with molecular size. Inclusion of polarizable heteroatoms also tends to increase the adsorption energies and leads to a preferential molecular adsorption orientation (e.g. perpendicular). The non-covalent interaction (NCI) plot technique was applied to probe the nature of the molecule-surface adsorption in real space. In general, NCI reveals incipient chemisorption contributions in cases where a molecular lone pair interacts with the surface and there is an increased adsorption contribution from the base density functional.

The calculated adsorption energies are in excellent agreement with experimental best-estimates for benzene on the various metal surfaces, with a mean absolute error (MAE) of 0.04 eV, which is comparable to the experimental precision. The MAE from similar dispersion-corrected functionals for benzene on the three metal surfaces is 0.19 (PBE-D3), 0.20–0.25 (PBE-TS), 0.08–0.11 (PBE-TS$^{\text{surf}}$), $0.04 - 0.08$ for MBD, and a range of $0.03 - 0.15$ eV from several vdW-DF functionals.

Our results dispel previous doubts about whether pairwise dispersion corrections can be used for the modeling of surface adsorptions. Contrary to previous applications of XDM and in contrast to PBE-TS$^{\text{surf}}$, physisorption can be reliably modeled with the canonical implementation of XDM combined with the usual B86bPBE base functional, which is known to give very accurate results for intermolecular interactions. Hence, we conclude that B86bPBE-XDM is an excellent approach to reliably model chemical processes occurring on material surfaces, with a cost comparable to any semilocal density functional.

Chapter 6: Adsorption of Graphene to Nickel (111) Using the Exchange-Hole Dipole Moment Model

Original reference: M. S. Christian, A. Otero-de-la-Roza and E. R. Johnson, Carbon **118**, 184 (2017).

6.1 Abstract

Graphene is a promising material for a number of technological applications due to its unique electronic properties. It can be mass produced by depositing carbon atoms on metal scaffolds, such as nickel. This chapter presents a detailed study of graphene adsorption on the nickel (111) surface using the exchange-hole dipole moment (XDM) dispersion correction. XDM is shown to model accurately graphene-nickel interactions, providing adsorption energies in excellent agreement with available experimental data and with RPA calculations. All six graphene-nickel orientations studied present a physisorption energy minimum, but only three exhibit chemisorption. The physisorption and chemisorption minima are close in energy, and are separated by a barrier of $\sim$ 1 kJ/mol per carbon. The relative strength of the chemisorption and physisorption interactions is found to depend heavily on the nickel lattice constant. Thermal expansion stabilizes chemisorption relative to physisorption. The pairwise dispersion coefficients depend strongly on the graphene-nickel distance, and their variation is determined by the exchange-hole dipole moments. If this dependence of the dispersion coefficients with the environment is properly captured, a pairwise dispersion correction (like XDM) is suitable to model surface adsorption.

6.2 Introduction

Graphene and its potential applications have received much attention over the past decade. Interest in this material grew as a result of the seminal investigation by Novoselov et al., in which the authors presented an experimental procedure, the "scotch-tape" method, to isolate high-quality stable graphene layers from graphite.[17] In the past few years, numerous papers have detailed graphene's unique electronic structure and properties.[4,9,17,18,45,212–220] Though the scotch-tape method is well suited to creating laboratory samples of graphene, the process is not applicable in the industrial scale. A promising scalable method for commercial graphene manufacturing involves depositing carbon atoms on metallic scaffolds,[20,22,221,222] via processes such as chemical vapor deposition (CVD).

In the CVD method, small molecules, such as methane and ethanol, are vaporized at high temperature ($\sim$ 1000 K). The resulting carbon soot is deposited on a metal surface, producing a single monolayer of adsorbed graphene. Once the monolayer is synthesized, a polymer resin is applied to the graphene surface and the metal is typically removed with an acid bath. The graphene layer can then be transferred to the desired substrate and the polymer resin dissolved.[22,23,223,224] Nickel is an excellent substrate for graphene synthesis because it is both inexpensive and its (111) surface has cell dimensions commensurate with graphene.[50,52,87,225,226] It has been shown that multi-layer graphene can be manufactured similarly, although the exact mechanism as to how multi-layers form is still under debate.[9,18,22,223]

Multiple studies of the graphene-nickel system using density-functional theory (DFT) have been published.[35–37,49,50,53,227,228] These articles show that generalized gradient approximation (GGA) functionals alone grossly fail to predict experimental adsorption energies and geometries of the graphene-nickel system because GGAs do not adequately describe London dispersion interactions. Even when dispersion interactions are taken into account (e.g. by using one of the

multiple available dispersion corrections[56,58,60,164,165,229]), reproducing the experimental graphene-nickel adsorption energies and interlayer distances is a challenge.[36,37,49,53] The difficulties arise from the competing factors that determine the nature of the metal-graphene interaction in this system. Experimentally, graphene is known to chemisorb on the nickel (111) surface;[87,230] its adsorption energy and distance depend critically on a fine balance between Pauli repulsion, dispersion, and the strength of the incipient chemical bond between graphene and the metal surface.[38]

The random phase approximation (RPA) method[50,231] is a significant improvement over both the local density approximation (LDA) and GGA functionals regarding the calculation of intermolecular interactions. Unlike dispersion-corrected GGAs, RPA incorporates dispersion interactions in a non-empirical seamless fashion, albeit at a much higher computational cost. Mittendorfer *et al.*[50] and Olsen *et al.*[231] used RPA calculations to show that graphene not only chemisorbs on nickel, but also physisorbs at larger interlayer distances, giving the adsorption potential energy surface (PES) a characteristic double-minimum profile, with the chemisorption and physisorption minima being very close in energy. Since RPA is too expensive for large surface models, GGA-based functionals have been proposed in the past that include dispersion either via an explicit non-local correlation contribution[133,232,233] or by adding a dispersion energy correction.[56–58,60,61,124,140] Janthon *et al.*[53] recently examined the ability of several of these density functionals to predict the graphene-nickel adsorption energy. Good adsorption energies and interlayer distances were obtained with optB86b-vdW[232,234] and DFT-D.[57] The latter is somewhat surprising given that both vdW-TS and DFT-D overestimate the strength of molecular physisorption on noble metal surfaces.[168,171,172] More recent developments of the same functionals (DFT-D3 and MBD) offer better performance.[235]

In this work, we investigate the adsorption of graphene on nickel (111) using GGA functionals combined with the exchange-hole dipole moment (XDM) disper-

sion correction.[60,61,236] XDM has been previously shown to accurately model a wide variety of systems where dispersion interactions play an important role: small noble gas clusters,[237,238] molecular dimers,[149,150,239] supramolecular systems,[240] and molecular crystal absolute[151] and relative lattice energies.[241,242] More relevant to this paper, we have demonstrated previously that XDM successfully predicts physisorption of molecules to surfaces.[64,243] An important point to note in these studies is that XDM shows good performance in widely different systems without any change to the formalism, implementation, or damping parameters, hence making it an ideal candidate for studying chemistry on surfaces and the interaction between inorganic materials and organic molecules.

In the remainder of this work, we show that XDM describes the graphene-nickel system accurately. Our results reproduce reported RPA potential energy surfaces[50,231] and agree with available experimental adsorption energies.[244] We also show that the predicted mode of adsorption (chemisorption or physisorption) is highly sensitive to the nickel lattice constant, and that accounting for thermal effects favors the chemisorption state. The results are discussed in the context of the mechanism of bilayer graphene formation on nickel substrates.

6.3 Computational Methods

Periodic-boundary DFT calculations were performed using the pseudopotential plane-wave approach and the Projector Augmented Wave (PAW) formalism.[114] Calculations were carried out using the XDM implementation in Quantum ESPRESSO[61,179] with the B86bPBE functional,[126,180] known to perform well in conjunction with XDM.[150,151] Calculations using the LDA[245] and PBE[126] exchange-correlation functionals were also conducted for comparison. PAW datasets for each functional were generated using LD1 version 4.3.2 using pslibrary 0.2.5 inputs. The datasets also included scalar relativistic effects and non-linear core corrections.[181] All datasets were checked to ensure that there was no PAW sphere overlap for each optimized geometry. An $8 \times 8 \times 1$ Γ-centered $\mathbf{k}$-point grid was

used, with a plane-wave cutoff of 60 Ry, a density expansion cutoff of 800 Ry, and cold smearing[108] with a smearing parameter of 0.01 Ry. All calculations used an initial spin-polarization and were checked for convergence to the correct spin state.

The XDM dispersion functional is a correction to the base DFT energy:

$$E = E_{\text{base}} + E_{\text{XDM}}, \tag{6.3.1}$$

$$E_{\text{XDM}} = -\frac{1}{2} \sum_{n=6,8,10} \sum_{i \neq j} \frac{C_{n,ij} f_n(R_{ij})}{R_{ij}^n}. \tag{6.3.2}$$

In this equation, i and j run over atoms in the system and R_{ij} is the interatomic distance. f_n is a damping function that attenuates the dispersion correction at short range, and the $C_{n,ij}$ are pairwise dispersion coefficients. Each $C_{n,ij}$ is approximated non-empirically via second-order perturbation theory using the multipole moments of the electron plus exchange-hole distribution and atom-in-molecule polarizabilities for the interacting atoms.[60]

The nickel (111) surface was modeled as an infinite slab consisting of six atomic layers. All calculations used a (1×1) surface unit cell, with a vacuum of 25 Å inserted in the z-direction to separate each slab from its periodic image. Six orientations of graphene on nickel were considered for this study (see Figure 6.3.1). The adsorption energies were calculated as the difference between the graphene-nickel system and the energies of the bare surface and isolated graphene sheet, whose geometries were optimized independently:

$$E_{\text{adsorption}} = -\left(E_{\text{adsorbate}} - E_{\text{surf}} - E_{\text{graph}}\right). \tag{6.3.3}$$

Throughout the article, adsorption energies are reported per carbon atom.

Potential energy surfaces (PES) for adsorption were generated by systematically varying the z distance between graphene and the nickel surface and performing a series of single-point energy calculations. The experimental lattice constants

Figure 6.3.1: Six orientations of graphene on nickel. The nickel top layer is shown in light gray, the second layer is blue, and the third layer from the surface is green. The nomenclature for the different graphene orientations follows previous works.[52,227]

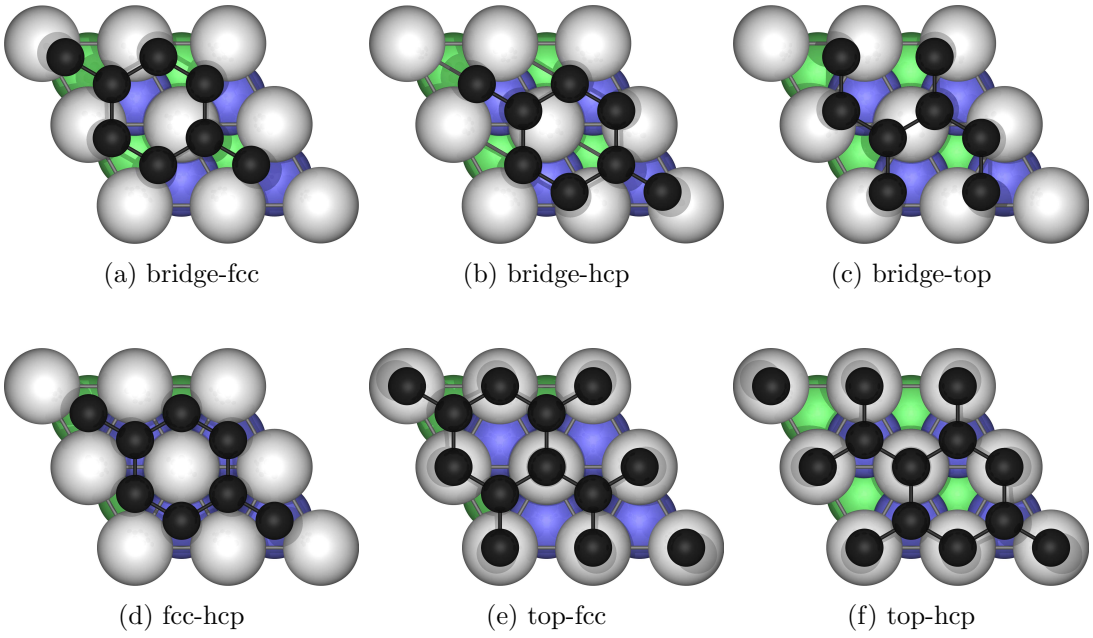

(a) bridge-fcc (b) bridge-hcp (c) bridge-top

(d) fcc-hcp (e) top-fcc (f) top-hcp

of graphene and nickel at room temperature are similar, but not exactly equal, and lattice vibrations cause a small, but not negligible, thermal expansion. As such, the dependence of the adsorption energy on the bulk lattice constant of the nickel slab was analyzed. Note that this lattice constant defines the length of the two symmetry-equivalent x, y-axes for the nickel slab, and the nickel-nickel interlayer distances as well. Calculations were performed with the lattice constant ranging between 2.45 Å and 2.50 Å in 0.01 Å increments. This range encompasses the minimum-energy interatomic distances in bulk nickel (2.450 Å with B86bPBE-XDM and 2.451 Å with PBE-XDM) and in graphene (2.462 Å with both functionals), as well as the minimum-energy lattice constant of a pure nickel (111) surface (2.465 Å with B86bPBE-XDM and 2.464 Å with PBE-XDM). It also encompasses the experimental interatomic distances in graphite (2.46 Å[246]), in bulk nickel (2.49 Å[246]), and in the nickel (111) surface (2.49 Å[247]). The final PES, minimum-energy structures, and adsorption energies for all orientations were obtained by quadratic interpolation between the results for each discrete value of

Table 6.4.1: Calculated B86bPBE-XDM interlayer distances and adsorption energies for all orientations of graphene on the nickel (111) surface at the minimum-energy nickel lattice constants. For the orientations in which chemisorption occurs, both the chemisorption (C) and the physisorption (P) values are given. Experimental distances[87,249] and adsorption energies[53,244] are shown for comparison. Distances are in Ångstrom (Å) and energies are in kJ/mol per carbon.

Orientation		Interlayer Distance	Adsorption Energy
bridge-fcc	P	3.25	8.00
bridge-hcp	P	3.26	7.97
fcc-hcp	P	3.34	7.54
bridge-top	C	2.14	7.31
	P	3.18	8.33
top-fcc	C	2.22	7.79
	P	3.15	8.50
top-hcp	C	2.28	6.48
	P	3.17	8.40
Expt.		2.04–2.18	7.20–11.20

the nickel lattice constant. This was done due to the strong dependence of the XDM dispersion coefficients on both the lattice constant and graphene-nickel separation (see Appendix B).

Finally, The nature of the graphene-nickel interaction was investigated using Bader's Quantum Theory of Atoms in Molecules (QTAIM).[116,248] QTAIM atomic charges were calculated using the Yu-Trinkle algorithm[118] implemented in the CRITIC2 program.[182] The differences between the QTAIM charges for the isolated nickel and graphene sheet and the adsorbate determines the degree of charge transfer.

6.4 Results and Discussion

6.4.1 Orientation Effects on Adsorption

The computed B86bPBE-XDM interlayer separations and adsorption energies for all six graphene orientations are reported in Table 6.4.1. Reference distances taken from microscopy experiments[87,249] are given for comparison. The reference

Figure 6.4.1: Adsorption energies as a function of interlayer distance for the six graphene-nickel orientations using the B86bPBE-XDM functional. At a given graphene-nickel distance, the minimum-energy lattice constant is used.

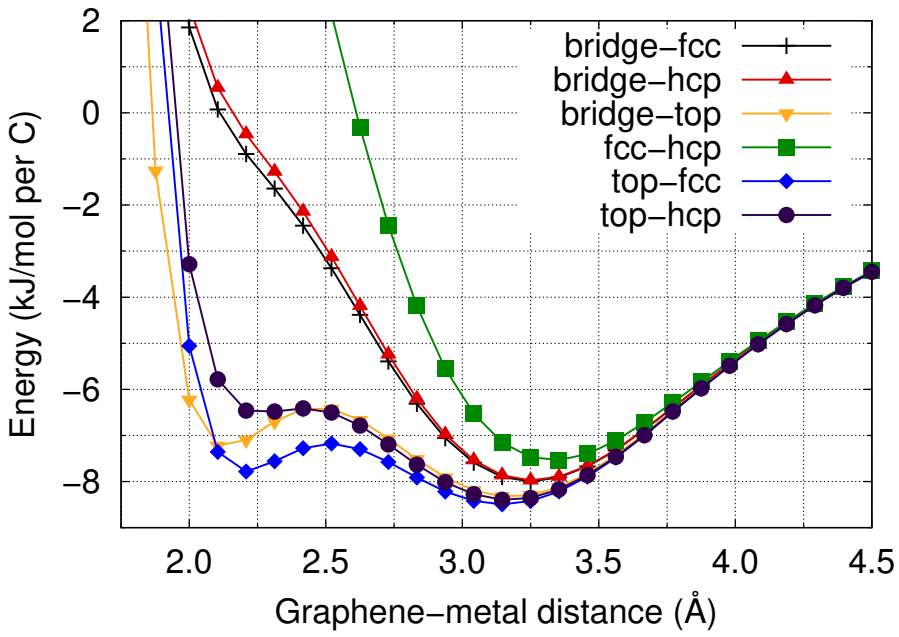

adsorption energy range is reported as in the work of Janthon *et al.*[53] and is based on the energies for graphene-nickel adsorption[244] relative to the interlayer adsorption in graphite.[250,251]

Figure 6.4.1 presents the calculated PES for adsorption of graphene in all six orientations, which clearly show the previously reported competing chemisorption and physisorption minima.[50,231] The PES for all six orientations show a physisorption minimum at interlayer distances between 3.15 Å and 3.35 Å. However, only three of the six orientations exhibit a chemisorption minimum, consistent with previous DFT studies.[52,226–228] The top-fcc orientation is found to be the most stable, in agreement with experimental observations.[87,228] Both the chemisorption and physisorption energies fall well within the experimental range. The predicted interlayer distances for the chemisorbed geometries are also close to experiment, although slightly longer. The PES show that the energy barrier between the chemisorption and the physisorption regions is small, in agreement with previous RPA results,[50,231] and varies depending on the orientation. Although physisorption has not been experimentally observed for graphene on the nickel (111) surface,

it has been observed in rotated Moiré patterns.[225,252,253]

All orientations present essentially the same physisorption energy, which is in line with Olsen *et al.*'s RPA results.[231] Analysis of the separate base functional and XDM dispersion contributions to the adsorption potential energy surfaces (Appendix B) shows that the XDM dispersion energy is effectively independent of the graphene-nickel orientation. Thus, all variations in the shape of the PES for the various graphene orientations originate at the base functional level, from differences in both exchange-repulsion and charge-transfer between the surface and substrate.

The ordering of the adsorption energies for the different orientations can be understood by examining the interactions between the individual carbon and nickel atoms, as shown in Figure 6.3.1. For the physisorption minima, the bridge-fcc and bridge-hcp orientations show slightly stronger adsorption than fcc-hcp because there is slight, though significant, carbon-nickel overlap. At shorter interlayer distances, these three orientations (bridge-fcc, bridge-hcp, and fcc-hcp) all show a steep repulsive wall whereas the other three (top-fcc, top-hcp, and bridge-top) show the formation of a chemisorption energy minimum. In the chemisorbed orientations, one carbon is either directly on top of a nickel atom (top-fcc and top-hcp) or two carbons straddle a single nickel (bridge-top), which is indicative of a weak chemical bond between both layers. The sub-surface nickel atoms lie directly under the second carbon atom in the top-hcp orientation, which provides less stabilization than if the sub-surface nickel atoms lie below the center of each graphene ring, as in the top-fcc orientation. The bridge-top orientation has a shorter interlayer separation despite its lower adsorption energy because the two carbon atoms bridge two nickel atoms, allowing the graphene to approach the surface more closely.

The small energy barrier between chemisorption and physisorption minima for the most-stable, top-fcc orientation suggests that physisorbed states may be accessible through thermal fluctuations.[252] It also may provide insight into graphene

Figure 6.4.2: Adsorption energies as a function of interlayer distance for the top-fcc orientation using the B86bPBE-XDM (black), PBE-XDM (red), and LDA (orange) functionals. The RPA results digitized from the work by Mittendorfer *et al.*[50] (blue circles) and by Olsen *et al.*[231] (green squares) are also shown. The experimental distance and energy ranges are shown as a shaded box.[53,87,244,249] For B86bPBE-XDM and PBE-XDM, two results are shown: energies using a minimum-energy lattice constant (solid lines) and the experimental bulk nickel lattice constant (dashed lines).

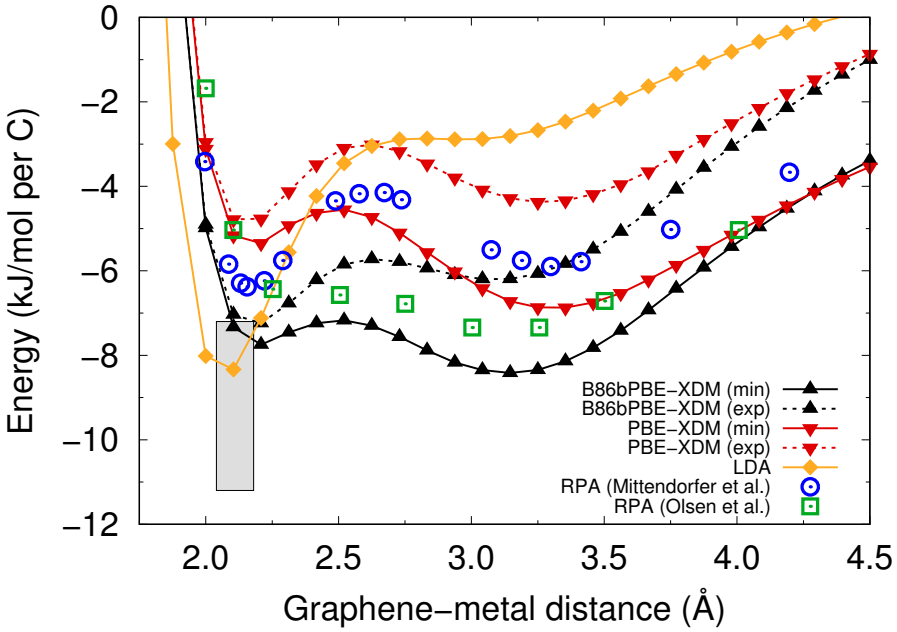

bilayer formation mechanisms. A graphene bilayer forms from the creation of a new graphene layer under an existing nickel-adsorbed graphene layer.[20,226,252] The proposed mechanism is based on nickel's carbon solubility during CVD.[20,226,252] Upon cooling, the carbon atoms exit the bulk, but are trapped beneath the existing chemisorbed graphene monolayer. The carbon atoms must push up the adsorbed graphene to assemble at the nickel surface and form a second underlying layer of graphene. The presence of a small energy barrier between the chemisorbed and physisorbed minima means that it would take little energy to displace an existing graphene monolayer, allowing for the facile accumulation and migration of carbon on the surface necessary to the formation of the graphene bilayer.

6.4.2 Comparison of Selected Density Functionals

Calculated adsorption energies as a function of interlayer distance for the top-fcc orientation using B86bPBE-XDM, PBE-XDM, and the LDA are compared with reference RPA values[50,231] in Figure 6.4.2. For the XDM-corrected functionals, two sets of potential-energy curves are shown, using either the minimum-energy nickel lattice constant (as in Figure 6.4.1) or using the experimental nickel lattice constant to allow direct comparison with the RPA results.

Figure 6.4.2 shows remarkable agreement between the minimum-energy B86bPBE-XDM potential-energy surface and experiment; the chemisorption energy is in the experimental energy range, and the distance is only 0.04 Å higher. Additionally, the equilibrium distances and absorption energies at the experimental nickel lattice constant are in good agreement with the analogous RPA calculations.[50,231] The B86bPBE-XDM chemisorption and physiorption energies are within 1 kJ/mol and 0.5 kJ/mol, respectively, of the RPA equivalents. Interlayer distances are also in excellent agreement with RPA. PBE-XDM provides similar potential energy surfaces to B86bPBE-XDM, although the PBE-XDM curves are slightly higher in energy and also have higher energy barriers between the chemisorbed and physisorbed minima.

It has been suggested that accurate modeling of surface adsorption can only be achieved through use of many-body dispersion corrections and not with "simple pairwise" methods.[63,147,148,254] A significant advantage of the XDM dispersion model over simple pairwise methods is that the dispersion coefficients are sensitive to the chemical environment in a physically-motivated way and this dependence was key to the high accuracy of the method in studies of molecular physisorption on noble metal surfaces.[64] In the present study, the surface nickel-carbon C_6 dispersion coefficients were found to exhibit a strong dependence on both the interlayer separation and the lattice constant (see Appendix B). In particular, these C_6's decrease substantially as graphene approaches the nickel surface, due to a decrease in the exchange-hole dipole moment integral caused by compaction of

the interface region between the graphene and the nickel surface. This behavior is only seen for nickel atoms at or near the surface; beyond the top two layers, there is no longer any change in the dispersion coefficients upon graphene adsorption. It is clear from the good agreement between the B86bPBE-XDM results and both RPA and experimental data that environmental effects captured by XDM's use of the self-consistent ground-state electron density are at least as important as non-pairwise many-body effects when modeling dispersion.

Comparison with literature adsorption energies and interlayer distances for the other orientations is included in Appendix B. B86bPBE-XDM and PBE-XDM both predict chemisorption for the bridge-top and top-fcc orientations and physisorption at the fcc-hcp orientation. These are two of the three criteria set by Janthon *et al.*[53] for accurate modeling of graphene-nickel interactions. The third criterion proposed by these authors is that graphene-nickel adsorption energies must be greater than the exfoliation energy of graphite, which is also met by B86bPBE-XDM (5.27 kJ/mol[61]) and PBE-XDM (4.76 kJ/mol[61]). These values are in good agreement with RPA's graphite exfoliation energy (4.63 kJ/mol[50]), as well as the reference experimental value (5.07 kJ/mol[250]).

Finally, although the LDA predicts a chemisorption energy and interlayer distance in good agreement with experiment, the chemisorption energy is less than the calculated LDA graphite exfoliation energy (2.39 kJ/mol[50]), in violation of the last of Janthon's criteria. Figure 6.4.2 shows that the LDA potential-energy surface is quite different than the DFT-XDM or RPA curves. The LDA physisorption minimum is very shallow and lies much higher in energy, due to the neglect of long-range dispersion stabilization. Thus, while the LDA predicts adequate adsorption energies and interlayer distances for chemisorption, the failure to correctly describe physisorption means that LDA cannot be recommended for any applications involving surface chemistry.

6.4.3 Lattice Effects on Adsorption

Our calculations reveal a strong dependence of the calculated chemisorption and physisorption energies on the nickel lattice constant. The optimum lattice constant for the graphene monolayer is predicted to be 2.46 Å with B86bPBE-XDM which is the same as seen in experiment.[255] However, there is notable difference between theory and experiment for the nickel lattice constant. The energy minimum for the bare nickel surface was found to occur at a lattice constant equal to 2.465 Å for B86bPBE-XDM (as well as PBE-XDM), which is smaller than the experimental value of 2.49 Å.[247] This underestimation of the nickel lattice constant is characteristic for relatively soft materials, and occurs due to neglect of vibrational and other thermal-expansion effects. These are more significant in nickel than graphene because of the more compressible nature of the nickel surface.

Figure 6.4.3 illustrates how small changes in the lattice constant affect the graphene-nickel potential energy surface. At the smallest tested lattice parameter, there is no chemisorption and only a physisorption minimum. Increasing the lattice constant lowers the repulsive shoulder significantly and the chemisorption minimum appears. The strongest physisorption occurs for a lattice constant of 2.46–2.47 Å, which corresponds to the graphene lattice constant. However, the strongest chemisorption occurs when the lattice constant is equal to 2.48 Å. At this lattice constant, the C-C bonds are slightly stretched from 1.421 Å to 1.432 Å, but the energy penalty incurred in this process is offset by the much stronger C-Ni interactions. Thus, the physisorption minimum is destabilized and the chemisorption minimum stabilized as the lattice-constant approaches the experimental nickel lattice constant of 2.49 Å.[247]

Figure 6.4.4 is a two dimensional potential energy surface that shows how the top-fcc adsorption energy changes as a function of lattice constant and interlayer distance. The chemisorption minimum begins to stabilize at 2.46 Å and is competitive with the physisorption minimum near 2.47 Å. At 2.48 Å, the physisorption minimum is destabilized and the chemisorption minimum becomes the more stable

Figure 6.4.3: The B86bPBE-XDM potential energy surface for the top-fcc graphene-nickel orientation for lattice constants ranging from 2.45 Å to 2.49 Å.

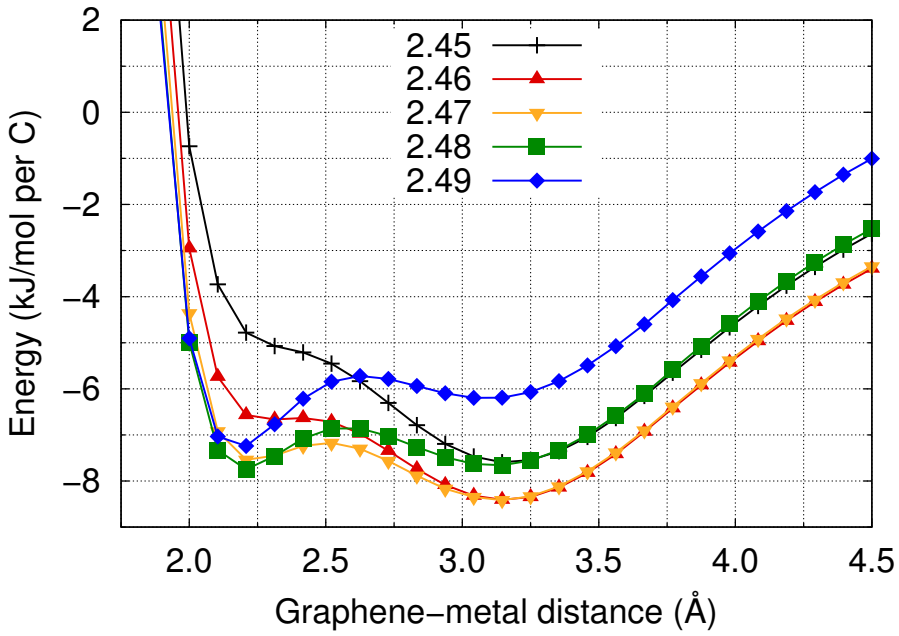

region of the potential. Above 2.50 Å, the entire system destabilizes due to the highly stretched C-C bonds. Generally, the physisorbed configuration is preferred when the lattice constant is closer to the experimental graphene lattice constant and the chemisorption configuration is preferred as the lattice constant approaches the experimental nickel lattice constant.

The important result coming from Figures 6.4.3 and 6.4.4 is that, for all lattice constants above a given threshold value (ca. 2.48 Å), the chemisorption minimum is more stable than the physisorption minimum. The simple but reasonable assumption can be made that the adsorption free energy is given by Figure 6.4.4, after adjusting the geometry for the effects of thermal expansion. This approximation is equivalent to a combination of a quasi-harmonic approach and a neglect of the differences in the free-energy contributions as a function of temperature, which we expect to be smaller than the differences in electronic energies. Under this assumption, our data predicts that chemisorption is favored compared to physisorption at the experimental geometry, in agreement with the experimental observations. We therefore expect chemisorption to be somewhat preferred over

Figure 6.4.4: Two-dimensional B86bPBE-XDM potential energy surface, illustrating the dependence of the adsorption energy for the top-fcc graphene-nickel orientation on the lattice constant.

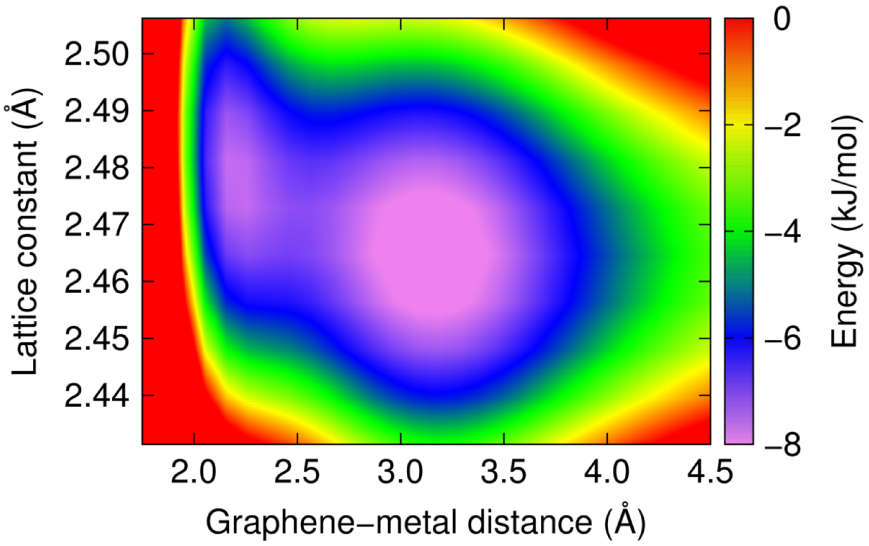

physisorption if thermal expansion of the nickel surface were taken into account in our calculations. In addition, we also predict that a decrease in temperature may eventually result in a physisorbed state, although the zero-point vibrational contribution to thermal expansion may already send the system over the threshold at 0 K.

6.4.4 Charge Transfer

Analysis of the charge transfer between nickel and graphene is presented in Table 6.4.2. This table reports the atomic charges for the three chemisorbed geometries at the experimental lattice constant for nickel (2.49 Å). The charge transfer for all of the physisorbed structures is zero, and is not shown. The largest charge transfer from nickel to graphene occurs for the bridge-top orientation since both carbon atoms in the periodic cell bridge the surface nickel atoms equally, leading to the shortest interlayer separation. The top-fcc and top-hcp orientations have similar interlayer distances, but the top-fcc has a stronger adsorption energy and higher charge transfer.

Table 6.4.2 also shows that charge transfer from the graphene to the nickel

Table 6.4.2: Charge of the two unique carbon atoms in the (1×1) cell and the surface nickel atom obtained from QTAIM analysis of the B86bPBE electron densities. Results are shown for the three chemisorbed orientations at a lattice constant of 2.49 Å and for the top-fcc orientation with lattice constants ranging from 2.46 to 2.49 Å. In all cases except bridge-top, C_{top} represents the carbon directly above a nickel atom.

	Ni	C_{top}	C_{other}
bridge-top	0.084	-0.049	-0.050
top-fcc	0.082	-0.069	-0.028
top-hcp	0.080	-0.069	-0.027
2.46	0.077	-0.067	-0.028
2.47	0.079	-0.067	-0.028
2.48	0.080	-0.068	-0.028
2.49	0.082	-0.069	-0.028

surface increases as lattice constant increases for the top-fcc orientation. The charge transfer from nickel to graphene correlates with the optimum graphene-nickel distance for the chemisorption minimum of the PES shown in Figure 6.4.1. Experimentally, it has been confirmed that graphene carbon-carbon bonds expand upon chemisorption, distorting the structure such that the graphene lattice constant becomes commensurate with that of nickel.[87,226,247] Spectroscopic measurements have shown that graphene's band structure is strongly perturbed upon adsorption.[255–257] Taken together with our results, this provides evidence that charge transfer is related to the stabilization of the deformed graphene layer.[226]

6.5 Summary

This chapter presented a detailed density-functional study of graphene adsorption on the nickel (111) surface. Our results show that both the B86bPBE-XDM and PBE-XDM methods predict optimum interlayer distances and adsorption energies in excellent agreement with previously reported reference RPA results[50,231] and available experimental data.[53,87,244,249] Thus, surface adsorption can be accurately modeled by a pairwise atomic dispersion correction provided that the dispersion coefficients have an appropriate dependence on the chemical environ-

ment.

Graphene was found to physisorb to the nickel surface in all six graphene orientations considered (see Figure 6.3.1), at a distance between 3.15 and 3.35 Å. The physisorption energies increase slightly with the number of close carbon-nickel atomic contacts. In this state, there is no significant chemical bond between graphene and nickel, and the adsorption is determined by dispersion plus closed-shell repulsion between both surfaces.

Three of the studied orientations (bridge-top, top-fcc and top-hcp) have chemisorption minima with optimum graphene-metal distances between 2.00 and 2.25 Å. The top-fcc orientation was found to be the most stable, in agreement with previous theoretical studies.[52,87,226–228,249] The potential energy as a function of interlayer distance for these orientations is a double-minimum curve, with the barrier between the physisorption and chemisorption minima being less than 1 kJ/mol per carbon. This suggests that physisorbed states may be accessible through thermal fluctuations,[252] and offers insight into the double-layer graphene formation in CVD experiments.[20,226,252] Both the chemisorption and physisorption energies are higher than the calculated graphite exfoliation energies.

The B86bPBE-XDM chemisorption energies are in the experimental energy range[53,244] and they also agree with RPA results[50] to within 1 kJ/mol (chemisorption) and 0.5 kJ/mol (physisorption) per carbon when the same lattice constant is used. We note, however, that the precision of the experimental data is 4 kJ/mol, and the two previously reported RPA potential energy surfaces are somewhat in disagreement with each other (up to about 2 kJ/mol), specifically regarding the presence of a double minimum in the energy profile. Hence, higher-quality reference data is required before the accuracy of B86bPBE-XDM can be precisely quantified.

In the chemisorbed state, there is significant charge transfer between graphene and nickel, which increases with the lattice constant. This is indicative of the formation of a weak chemical bond and the disruption of the nickel and graphene band

structures, as previously observed.[38,255–257] The differences in the chemisorption behavior between orientations are determined by whether there is a direct carbon-nickel contact that facilitates the approach between both surfaces. Therefore, it is the base functional contribution, and not the dispersion correction, that determines the behavior in the chemisorption distance range, although the dispersion correction is a major component of the adsorption energy in all orientations.

It was also found that the graphene-nickel adsorption is strongly dependent on the lattice geometry, which somewhat hinders the comparison to experimental results. At the electronic-energy minimum (lattice constant around 2.46 Å), physisorption is preferred over chemisorption. However, as the lattice constant increases, chemisorption becomes the preferred state at a surface lattice constant equal to 2.48 Å. Thermal expansion pushes the lattice constant over this threshold (the experimental lattice constant is 2.49 Å for the nickel (111) surface), resulting in a stabilization of the experimentally observed chemisorption state.

Chapter 7: Adsorption of Graphene to Metal (111) Surfaces using the Exchange-Hole Dipole Moment Model

Original reference: M. S. Christian, A. Otero-de-la-Roza and E. R. Johnson, Carbon **124**, 531 (2017).

7.1 Abstract

Graphene has a unique electronic structure and excellent tribological properties. A promising method for graphene production involves depositing vaporized carbon on metal substrates, which can also be used to modify graphene's electronic structure through charge transfer. In this work, graphene adsorption on the (111) surface of seven metals (Al, Cu, Ag, Au, Ni, Pd, and Pt) is investigated computationally using density-functional theory with the exchange-hole dipole moment (XDM) dispersion correction. Two distinct graphene-metal orientations, corresponding to 0° and 30° relative rotation of the graphene layer, are considered to investigate how lattice mismatch affects adsorption. Our results reproduce reference data from the random phase approximation more closely than any other dispersion-corrected density functional, confirming that XDM is an excellent method for surface chemistry. The rotational orientation of graphene is found to strongly affect its interaction with the substrate. There is an energetic drive for graphene to align with the metal lattice, particularly for Pd and Pt, which causes the formation of multiple Moiré patterns, in agreement with experimental observations.

7.2 Introduction

Graphene is a material that holds the potential to revolutionize the semiconductor industry. Various applications have been proposed that utilize graphene's unique two-dimensional electronic structure.[4,9,17,18,45,212–220] Graphene has also been shown to be an excellent solid lubricant[9,258,259] that can reduce friction and wear in mechanical devices either through direct surface deposition or as an additive to petroleum-based lubricants.[11,45] While the original scotch-tape method for graphene isolation[17] easily produces laboratory samples, it is not scalable for mass production. Lack of a suitable mass-production method has hindered commercialization of graphene-based technologies,[18,23] but several methods have showed promising results. One such method is chemical vapor deposition (CVD),[20,22,221,222] where a carbon feedstock is vaporized to produce pure carbon that is deposited onto a metal surface. Additionally, charge transfer from the underlying metal substrate[20] provides a mechanism to tune graphene's electronic structure through the alteration of its valence band.[260]

Graphene-metal systems have been investigated experimentally[23,28–34,88,89,261–266] to understand electronic and tribological properties as well as monolayer growth mechanisms. These investigations have shown that graphene can either chemisorb, physisorb, or form a carbide phase on the surface.[23,30] Metals on which graphene chemisorbs or physisorbs are of the most practical interest because the adsorbed graphene will retain its unique electronic structure.

The most promising substrates for graphene mass production are Cu and Ni. Not only are these metals inexpensive, but their surface lattice constant is close to that of graphene. This excellent lattice match results in a limited number of observed Moiré patterns and reliable formation of large continuous graphene monolayers on the surface.[50,52,87,225,226] In particular, a CVD method using Cu has shown promising results for graphene mass production.[21] Metals such as Pd,[33,34,261] Pt,[28,32,88,262–265] and Au[28,31,89,266] have also been investigated

for graphene synthesis, but their lattice mismatch results in multiple Moiré patterns on single surface samples. Indeed, experiments suggest that there exist an infinite number of Moiré patterns for Pt and Pd.[33,88,261–263] In the early stages of graphene patterning on Pd and Pt, local graphene domains will bind strongly to the surface, but as the monolayer size increases, the overall surface-substrate interaction weakens because of the lattice mismatch. Light emitting electron diffraction (LEED) experiments have shown that strong surface-substrate interactions occur on Pd and Pt but depend on the rotational alignment,[34,265] which has resulted in conflicting reports as to the nature of graphene-Pd/Pt interactions.

Many previous publications have used density-functional theory (DFT) to investigate graphene adsorption on metal surfaces.[36,37,39,50,53,267] Most studies employed the local density approximation (LDA) because it predicts reasonable chemisorption geometries.[34,35,38,54,88,268,269] However, the LDA is known to overestimate chemisorption energies and under-estimate physisorption because it does not include the physics of London dispersion. This results in narrow potential energy surfaces (PES) at chemisorption distances, with only shallow adsorption at typical physisorption distances, in disagreement with higher levels of theory, such as the random phase approximation (RPA).[39]

Generalized-gradient-approximation (GGA) type functionals combined with a dispersion correction are quite accurate for van der Waals complexes.[56,58,60,164,165,229] However, the majority of these dispersion corrections are less reliable for metal surfaces due to the empirical nature of the dispersion coefficients[64,168,169,171,172,235] and it has been argued that many-body effects may be important for accurate modeling of surface adsorption.[148] Non-local van der Waals density functionals (vdW-DF)[133,184,232,233] are typically more reliable for molecular physisorption on metal surfaces.[64,173] Several groups[36,37,53] have studied adsorption of graphene on multiple metals using vdW-DF functionals; however, there are massive differences between the results depending on the base GGA functional used. For example, vdW-DF2[184] (which uses revPBE[270]) predicts weak physisorption on Cu and Ni,

while vdW-DF-C09[271] predicts stronger chemisorption.[37] The best available theoretical reference data for graphene adsorption is a study using the random phase approximation (RPA) by Olsen and Thygesen.[39] Though the RPA agrees with most experimental observations, the scope of this investigation was limited to a single Moiré pattern on each studied metal that minimized lattice strain,[39] which precludes prediction of the orientation dependence.[268]

This chapter is the second part of a series[272] investigating graphene-metal adsorption using DFT paired with the exchange-hole dipole moment (XDM) dispersion correction.[60,61,273] The XDM model is a non-empirical dispersion correction that uses the electron density to generate environment-dependent dispersion coefficients. As a result, XDM is uniquely suited to model dispersion interactions across a wide range of chemically diverse systems, such as molecular dimers,[61,150] supramolecular systems,[240] organic crystals,[151,241] and most closely related to this work, molecular physisorption.[64] The first part of this series was limited to graphene adsorption on nickel, for which XDM was found to provide excellent agreement with both RPA reference calculations and the experimental adsorption energy.[272] However, this is no guarantee that the high accuracy of XDM will be transferable to modeling graphene adsorption on other metals.

In the present work, we have broadened our study to include six additional metals: Al, Cu, Ag, Au, Pd, and Pt. The XDM results are found to more closely reproduce RPA interlayer distances and adsorption energies[39] than other, previously-applied density functionals. Additionally, this is the first dispersion-corrected DFT study to investigate graphene adsorption in two rotational orientations, corresponding to 0° and 30° Moiré patterns. It is shown that the graphene-substrate interaction strength is highly dependent on rotational orientation. The XDM calculations predict particularly strong graphene-surface interactions in the 0° orientation for Pd and Pt, which explain the experimental observation of multiple Moiré patterns with locally-ordered graphene domains. Finally, our results suggest that larger units cells (impractical for DFT calculations) are needed to properly model

graphene-metal interactions for substrates with large surface-lattice mismatches.

7.3 Computational Methods

The computational methods used here are consistent with our previous work on Ni(111)-graphene.[272] All DFT calculations were performed using periodic boundary conditions with the projector augmented wave (PAW) formalism[114] as implemented in Quantum ESPRESSO.[61,179] The exchange-correlation functional chosen was B86bPBE,[126,180] as it provides the best accuracy when paired with the XDM dispersion model.[64,151] PAW datasets were generated using LD1 version 4.3.2 using pslibrary 0.2.5 inputs. The datasets also included scalar relativistic effects and non-linear core corrections.[181] All datasets were checked to ensure that there was no PAW sphere overlap for each optimized geometry. An $8 \times 8 \times 1$ Γ-centered **k**-point grid was used, with a plane-wave cutoff of 60 Ry, a density expansion cutoff of 800 Ry, and cold smearing[108] with a smearing parameter of 0.01 Ry.

The XDM dispersion energy is a post-SCF correction to the B86bPBE (base) energy:

$$E = E_{\text{base}} + E_{\text{XDM}}, \tag{7.3.1}$$

$$E_{\text{XDM}} = -\frac{1}{2} \sum_{n=6,8,10} \sum_{i \neq j} \frac{C_{n,ij} f_n(R_{ij})}{R_{ij}^n}. \tag{7.3.2}$$

In this equation, i and j run over atoms in the system, R_{ij} is the interatomic distance, f_n is a damping function that attenuates the dispersion correction at short range, and the $C_{n,ij}$ are pairwise atomic dispersion coefficients. Each $C_{n,ij}$ is evaluated using the multipole moments for the interacting atoms arising from a reference electron together with its corresponding exchange-hole distribution, as well as atom-in-molecule polarizabilities.[60,273]

In this work, calculations were performed for graphene adsorption on six metal surfaces: aluminum, copper, silver, gold, palladium, and platinum. Additionally, our previous results for nickel[272] are reported again here for comparative purposes. All calculations for the Ni-group metals used an initial spin-polarization

and checked for convergence to the correct spin state, while those for Al and the Cu-group metals did not. All metals considered have a face-centered cubic (fcc) crystal structure and adsorption of graphene on the (111) surface was studied. Two different orientations, or Moiré patterns, were modeled to compare how rotational orientation affects graphene-substrate interactions. These were constructed using the (1×1) surface unit cell for the 0° orientation, where the lattice vectors of graphene's primitive cell align with the (111) metal surface's primitive cell (Figure 7.3.1(b,c)). The $(\sqrt{3} \times \sqrt{3})$ surface unit cell was obtained by rotating the metal substrate by 30° relative to the graphene sheet (Figure 7.3.1(a)). Both of these orientations have been established in previous works,[36,37,39,267] with the (1×1) cell commonly used for Ni and Cu and the $(\sqrt{3} \times \sqrt{3})$ cell used for the remaining metals to minimize lattice strain.

Geometries for graphene adsorbed in the 30° orientation and two of the possible structures (top-fcc and fcc-hcp, using the common nomenclature[36,37,39,50,272]) for the 0° orientation are illustrated in Figure 7.3.1. Calculations were also performed for the four remaining structures in the 0° orientation (bridge-fcc, bridge-hcp, bridge-top, and top-hcp). The larger $(\sqrt{3} \times \sqrt{3})$ cell for the 30° orientation results in a periodic graphene layer with eight carbon atoms per cell, as the graphene unit cell is 2 times longer in each direction compared to the 0° orientation. The carbon atoms are equally split over void and on-top sites, such that the interactions are degenerate upon x-y translation, and only the structure shown in Figure 7.3.1(a) need be considered. In the following sections, the geometries for each of these cells will be discussed using the cell lengths represented in Figure 7.3.1. The relations between these quantities are: $a_{1\times1} = r$, $a_{\sqrt{3}\times\sqrt{3}} = r\sqrt{3}$, $a_{\text{cubic}} = r\sqrt{2}$, where r is the nearest-neighbor metal-metal distance, a_{cubic} is the cell length of the conventional (cubic) cell for the bulk metal (fcc), and $a_{1\times1}$ and $a_{\sqrt{3}\times\sqrt{3}}$ are the cell lengths of the (1×1) and $(\sqrt{3} \times \sqrt{3})$ cells, respectively, as depicted in Figure 7.3.1. The primitive cell length of graphene is matched to the (1×1) cell on the metal surface, and a 2×2 graphene supercell matches the metal surface's $(\sqrt{3} \times \sqrt{3})$ cell.

Figure 7.3.1: Structure of graphene adsorbed on a (111) metal surface for (a) the $(\sqrt{3} \times \sqrt{3})$ unit cell (30° rotation, see text) and (b,c) two selected translational orientations in the (1×1) unit cell (0° rotation). The metal top layer is shown in light gray, the second layer is blue, and the third layer from the surface is green. Unit cells for the 0° and 30° rotations are shown in red.

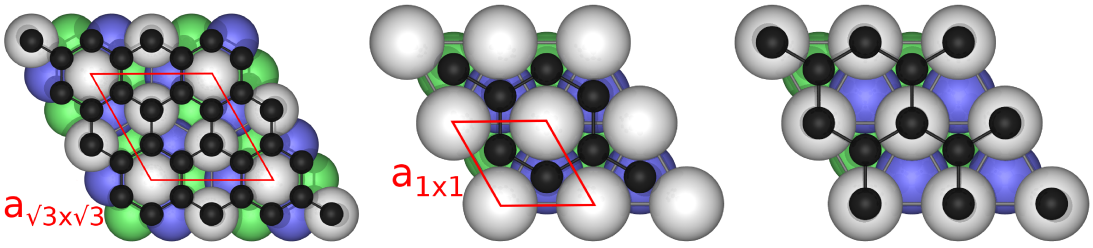

(a) $(\sqrt{3} \times \sqrt{3})$ (b) (1×1) fcc-hcp (c) (1×1) top-fcc

Potential energy curves for graphene adsorption were computed for all metals. As in our previous work for nickel,[272] the metal was represented by a six-layer slab and a cell 70 atomic units long in the vacuum direction to separate each slab from its periodic image. The adsorption energies are defined as

$$E_{\text{ads}} = -\left[E_{\text{surf+graph}}(a^{\text{ads}}) - E_{\text{surf}}(a^{\text{surf}}) - E_{\text{graph}}(a^{\text{graph}})\right], \tag{7.3.3}$$

where $E_{\text{surf+graph}}(a^{\text{ads}})$ is the energy of the graphene plus metal system at its equilibrium geometry (a^{ads}) in the chosen orientation, and $E_{\text{surf}}(a^{\text{surf}})$ and $E_{\text{graph}}(a^{\text{graph}})$ are the energies of the metal surface and graphene at their respective minimum energy geometries. Occasionally, two adsorption energies are possible when chemisorption and physisorption minima coexist on the same potential energy surface.[272]

In addition, to allow direct comparison between the results for the (1×1) and $(\sqrt{3} \times \sqrt{3})$ cells, we define the constrained adsorption energy as

$$E_{\text{ads}}^{\text{cons}} = -\left[E_{\text{surf+graph}}(a^{\text{ads}}) - E_{\text{surf}}(a^{\infty}) - E_{\text{graph}}(a^{\infty})\right], \tag{7.3.4}$$

where $E_{\text{surf}}(a^{\infty})$ and $E_{\text{graph}}(a^{\infty})$ are the energies of the infinitely separated metal surface and the graphene sheet, constrained to have the same lattice constant (a^{∞}). The sum of these two energies is easily obtained as the surface lattice constant that minimizes the total value of $E_{\text{surf}}(a) + E_{\text{graph}}(a)$, where the surface

and graphene energies are calculated independently. Relaxed, not constrained, adsorption energies were reported in our previous study of graphene adsorption on nickel.[272] The lattice strain energy is defined as the difference between the constrained and the relaxed adsorption energies:

$$E^{\text{strain}} = [E_{\text{surf}}(a^{\infty}) - E_{\text{surf}}(a)] + [E_{\text{graph}}(a^{\infty}) - E_{\text{graph}}(a)]\,. \tag{7.3.5}$$

The strain energy is always positive, and it is low compared to the constrained adsorption energy only when graphene and metal surface have matching lattices in the selected orientation. Positive adsorption energies indicate favorable adsorption relative to the separated surfaces.

Due to current limitations regarding the calculation of XDM forces for the particular case of metal surfaces,[272] the minimum-energy structures were determined by calculating multiple adsorption potential energy surfaces, varying the surface lattice constants in 0.01 Å intervals. Minimum-energy PES were obtained by performing quadratic fits to the energy as a function of surface lattice constant at every graphene-metal distance. This procedure determines the minimum-energy surface lattice constant, graphene-metal distance, and adsorption energy. Throughout the article, adsorption energies are reported in kJ/mol per carbon atom.

Finally, the extent of charge transfer between metal and graphene was investigated using Bader's Quantum Theory of Atoms in Molecules (QTAIM).[116,248] QTAIM atomic charges were calculated using the Yu-Trinkle algorithm[118] (YT) implemented in the CRITIC2 program.[182] The QTAIM charges for the carbon atoms of the adsorbed graphene sheet determine the degree of charge transfer.

Table 7.4.1: Comparison of calculated and experimental bulk and (111) surface lattice constants for the considered metals and graphene. All metals have a face-centered cubic (fcc) structure. The calculated surface lattice constants are reported for both the (1×1) and $(\sqrt{3} \times \sqrt{3})$ unit cells. The metal surfaces that minimize the strain energy, as defined in Eq. 7.3.5, are indicated in bold. Lattice constants are also given for the combined graphene+metal system for both the minimum-energy adsorbed configuration (a^{ads}) and for the infinitely separated constrained system (a^{∞}, Eq. 7.3.4). For Ni and Pt, chemisorption and physisorption minima are present. All lengths are in Å and all energies are in kJ/mol per carbon atom.

	Bulk		Clean surface			Graphene + metal					
	$a_{\text{cubic}}^{\text{expt}}$ [246]	a_{cubic}	$a_{1\times1}^{\text{expt}}$	$a_{1\times1}$	$a_{\sqrt{3}\times\sqrt{3}}$	$a_{1\times1}^{\text{ads}}$	$a_{1\times1}^{\infty}$	$E_{1\times1}^{\text{strain}}$	$a_{\sqrt{3}\times\sqrt{3}}^{\text{ads}}$	$a_{\sqrt{3}\times\sqrt{3}}^{\infty}$	$E_{\sqrt{3}\times\sqrt{3}}^{\text{strain}}$
Al	4.050	4.001	2.86[274]	2.855	**4.946**	2.721	2.722	75.6	4.931	4.930	**0.1**
Cu	3.615	3.576	2.56[275]	**2.555**	4.425	2.520	2.520	**4.1**	–	4.671	–
Ag	4.086	4.081	2.89[276]	2.944	**5.100**	2.818	2.817	116.1	5.030	5.023	**4.8**
Au	4.078	4.136	2.88[31]	2.956	**5.120**	2.858	2.858	128.4	5.045	5.049	**4.9**
Ni	3.524	3.462	2.49[247]	**2.477**	4.291	2.481, 2.466	2.464	**0.0**	–	4.574	–
Pd	3.890	3.933	2.75[33]	2.806	**4.856**	2.751	2.726	66.9	4.865	4.868	**1.8**
Pt	3.923	3.968	2.78[277]	2.822	**4.887**	2.787, 2.760	2.760	78.1	4.878	4.881	**1.1**
Graphene (calc.)				2.474	4.948						
Graphene (expt)				2.46[255]	4.92						

7.4 Results and Discussion

7.4.1 Lattice Constants and Adsorption Energies

The computed lattice constants for graphene, the bulk metals, and adsorbed graphene are compared to the available experimental values in Table 7.4.1. B86bPBE-XDM performs quite well for the lattice constants of the bulk metals, with errors for the conventional (cubic) cell length of 0.06 Å or less. Similarly, the errors are 0.08 Å or less for the (1×1) surface lattice constants.

For the (1×1) cell, the lattice constants for the graphene-metal system are typically below the optimum values for the clean metal surface to reduce the lattice strain from stretching the graphene C-C bonds. The lattice mismatch between graphene and the metal surface results in highly stretched C-C bonds for Al, Ag, Au, Pd, and Pt in this orientation, which results in extremely high strain energies for these metals. As a result, previous DFT studies have all used a rotated $(\sqrt{3} \times \sqrt{3})$ unit-cell, corresponding to the 30° Moiré pattern, for all metals except Cu and Ni.[36,37,39,267] For this cell, the strain within the graphene sheet is minimized, with the C-C bonds stretched no more than 0.04 Å relative to their equilibrium values. In the $(\sqrt{3} \times \sqrt{3})$ orientation, the lattice constants for the graphene-metal system are quite close to the optimum values for the clean metal surfaces and the strain energies are low (5 kJ/mol or less) compared to their (1×1) counterparts. However, consideration of only the $(\sqrt{3} \times \sqrt{3})$ precludes prediction of interaction energies for an adsorbed layer with direct carbon-metal contacts, as occur for several orientations of the (1×1) cell. Graphene adsorption on Cu or Ni was not studied with the rotated $(\sqrt{3} \times \sqrt{3})$ unit cell due to the lack of experimental evidence of its existence and the highly compressed C-C bonds that would result from this geometry.

Table 7.4.2 shows the calculated constrained and relaxed adsorption energies for all metals and orientations. The results for Ni are reproduced from our previous study and are included for comparison, while all other results are original to the

Table 7.4.2: Constrained ($E_{\text{ads}}^{\text{cons}}$, Eq. 7.3.4) and relaxed (E_{ads}, Eq. 7.3.3) adsorption energies for all metals and orientations in this work. The "Type" column indicates whether the entry is a physisorption (P) or chemisorption (C) minimum. Negative energies reflect that the orientation is not energetically stable. The maximum constrained and relaxed adsorption energies for each metal are indicated in bold. The units are kJ/mol per carbon atom.

		Al		Cu		Ag		Au	
Orientation	Type	$E_{\text{ads}}^{\text{cons}}$	E_{ads}	$E_{\text{ads}}^{\text{cons}}$	E_{ads}	$E_{\text{ads}}^{\text{cons}}$	E_{ads}	$E_{\text{ads}}^{\text{cons}}$	E_{ads}
1×1 bridge-fcc	P	4.2	-71.4	6.8	2.6	9.1	-107.0	7.2	-121.2
1×1 bridge-hcp	P	4.3	-71.3	6.7	2.6	9.1	-107.1	7.2	-121.3
1×1 bridge-top	P	4.4	-71.3	7.0	2.8	9.6	-106.5	7.5	-120.9
1×1 fcc-hcp	P	4.1	-71.6	6.5	2.3	8.4	-107.8	6.7	-121.7
1×1 top-fcc	P	4.2	-71.4	**7.1**	**2.9**	**9.9**	-106.3	**7.7**	-120.7
1×1 top-hcp	P	**4.6**	-71.0	7.0	2.9	9.7	-106.4	7.6	-120.8
$\sqrt{3} \times \sqrt{3}$	P	3.2	**3.2**	—	—	6.9	**2.1**	6.4	**1.5**

Orientation	Type	Ni		Pd		Pt	
		$E_{\text{ads}}^{\text{cons}}$	E_{ads}	$E_{\text{ads}}^{\text{cons}}$	E_{ads}	$E_{\text{ads}}^{\text{cons}}$	E_{ads}
1×1 bridge-fcc	C	—	—	10.2	-56.7	—	—
	P	8.0	8.0	—	—	6.9	-71.3
1×1 bridge-hcp	C	—	—	9.8	-57.1	—	—
	P	8.0	8.0	—	—	6.8	-71.4
1×1 bridge-top	C	7.3	7.3	**20.5**	-46.5	**14.6**	-63.5
	P	8.3	8.3	—	—	7.3	-70.9
1×1 fcc-hcp	P	7.5	7.5	6.7	-60.2	6.4	-71.8
1×1 top-fcc	C	**7.8**	**7.8**	16.3	-50.7	7.8	-70.3
	P	**8.5**	**8.5**	—	—	**7.6**	-70.6
1×1 top-hcp	C	6.5	6.5	14.9	-52.0	5.9	-72.3
	P	8.4	8.4	—	—	7.2	-71.0
$\sqrt{3} \times \sqrt{3}$	P	—	—	6.3	**4.5**	6.8	**5.7**

present work. In agreement with the lattice constants and strain energies in Table 7.4.1, the (1×1) orientation is stable for Ni and Cu only, and the $(\sqrt{3} \times \sqrt{3})$ is favorable for the rest of the metals. Importantly, only nickel and platinum present adsorption energies higher than the exfoliation energy of graphite[53,61,272] (experimental value = 5.1 kJ/mol[250]). The group 11 metals all show relatively low stabilization relative to the graphite exfoliation energy (Cu, 2.9 kJ/mol; Ag, 2.1 kJ/mol; Au, 1.5 kJ/mol). However, for a real surface, the graphene can adopt rotational orientations with much longer periodicity, or the surface can undergo reconstruction, to further reduce the lattice strain. Unfortunately, such orientations cannot be modeled practically with DFT methods due to the very large unit-cell dimensions required. As is common practice in DFT studies, the remainder of this work will focus on the constrained adsorption energies, which should provide a more representative view of the local graphene-metal interactions.

Table 7.4.2 shows striking differences in the graphene-metal interaction strengths between metals in group 10 and 11. Whereas Ni and Cu have similar constrained adsorption energies (slightly larger for Ni), Pt and particularly Pd show a strong tendency towards chemisorption that is absent in their group-11 counterparts (Au and Ag, respectively). Despite this, the lack of a suitable orientation makes Pt and Pd unable to bind graphene strongly, due to the very high strain energy. These results serve to reconcile some of the experimental observations[34,265] where Pt and Pd show either weak or strong adsorption, depending on the orientation (see Section 7.4.6). It should also be noted that both the graphene and the Pd and Pt surfaces are severely distorted in the 1×1 orientation, which may increase their reactivity (although the same effect is not observed on Ag and Au).

7.4.2 Potential Energy Surfaces

Computed B86bPBE-XDM PES for adsorption of graphene on all seven metals are shown in Figure 7.4.1 for all six orientations of the (1×1) cell and for the $(\sqrt{3} \times \sqrt{3})$ cell. To compare the behavior of all orientations in the same plot, constrained

adsorption energies are used. The dotted lines correspond to orientations with significant lattice strain (which would otherwise appear at much higher energies). As shown in Appendix C, the dispersion contribution to the PES is effectively independent of the orientation. Hence, the differences in the PES between the various orientations are primarily due to differences in the direct C-metal contacts and the extent of *d*-band hybridization and charge transfer (Section 7.4.4) arising at the base-functional level.

For the (1×1) cell, the PES in Figure 7.4.1 show local chemisorption minima for all three Ni-group metals in the top-fcc, top-hcp and bridge-top orientations. For Pd, there is also chemisorption in the bridge-fcc and bridge-hcp orientations, although it is significantly weaker. As noted in our previous study on the Ni surface,[272] chemisorption is made possible by the direct C-metal atomic contacts, as are present for top-fcc, top-hcp and bridge-top. However, only physisorption is seen for the fcc-hcp orientation, in which graphene C atoms are all above surface voids. Chemisorption similarly does not occur for the $(\sqrt{3} \times \sqrt{3})$ unit cell, for which the adsorption PES are nearly equivalent to the fcc-hcp curves for Pd and Pt. Therefore, it is the graphene-carbon interaction, or lack thereof, that results in the presence of a chemisorption minima for the Ni-group metals, likely arising from the hybridization between the graphene p orbitals and the d band of the metal surface. Although the chemisorption minima are relatively much deeper for Pd and Pt than for Ni, the lattice mismatches prevent clean monolayer formation on these metals.

For Al and the Cu-group metals, the PES in Figure 7.4.1 show no chemisorption minima. Compared to the Ni-group metals, the d bands of the Cu-group are lower in energy relative to the Fermi level, which precludes hybridization with graphene's p orbitals. Therefore, the differences between the six possible (1×1) orientations are much smaller than for the Ni-group, with the net adsorption energies varying by 0.5-0.6 kJ/mol C between the various orientation for Al and Cu. These differences increase somewhat for the other two members of the group,

Figure 7.4.1: Computed B86bPBE-XDM PES for adsorption of graphene on selected metals in the $(\sqrt{3} \times \sqrt{3})$ cell and all six possible orientations of the (1×1) cell. The left column shows results for the Ni-group metals, while the right column shows results for Al and the Cu-group metals. Constrained adsorption energies are used in this plot (i.e. metal and graphene are forced to have the same surface lattice constant at infinite separation). The orientations with significant lattice mismatch, which would be much higher in energy if the relaxed adsorption energies were used, are shown as dotted curves.

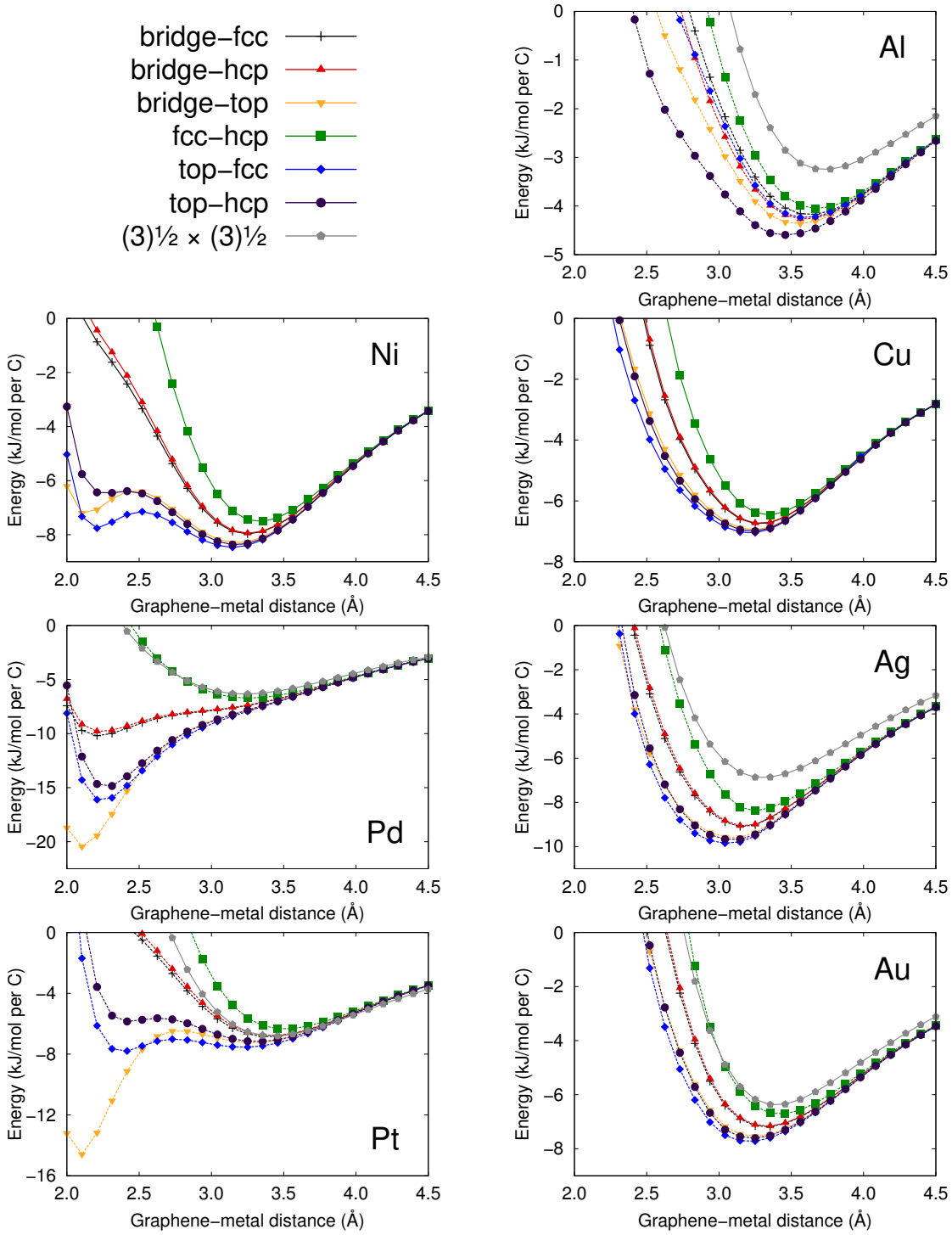

with a spread between the most- and least-stable orientations of 1.0 kJ/mol C for Au and 1.5 kJ/mol C for Ag. It is more energetically favorable for the carbon atoms to lie directly above the surface atoms rather than the void sites, resulting in deeper PES for the top-fcc, top-hcp and bridge-top orientations than for the fcc-hcp orientation, in which there are no direct C-metal contacts (Figure 7.3.1). The $(\sqrt{3} \times \sqrt{3})$ PES are significantly more shallow than the (1×1) PES for Al and Ag. As will be shown in Section 7.4.4, this is due to the significant surface-substrate charge transfer that occurs in the (1×1) cell for Al and Ag at the physisorption minima. Al and Ag have the lowest work functions of the series of metals considered.

7.4.3 Dispersion and Periodic Trends

Optimal B86bPBE-XDM graphene-metal interlayer distances and metal-carbon C_6 dispersion coefficients are reported in Table 7.4.3. The C_6 dispersion coefficients are the main factor that determines the equilibrium distances and adsorption energies at the physisorption minima. The optimum interlayer distances for the physisorption minima are nearly degenerate for each periodic row, due to the similar atomic sizes. Al has the lowest C_6 coefficient, resulting in the lowest physisorption energy and the largest interlayer distance. The C_6's, optimum interlayer distances, and adsorption energies generally increase down the periodic groups, with the exception of Au and Pt, for which the C-metal C_6 and graphene adsorption energy are lower than for Ag and Pd, respectively. This is due to relativistic effects, which cause Au/Pt to be significantly more electronegative than Ag/Pd, resulting in a lower polarizability and weaker dispersion attraction.[64,149]

Ni and Pt display both chemisorption and physisorption minima, while graphene only chemisorbs on Pd. This occurs because of a combination of a higher base-functional contribution to the adsoprtion PES due to *d*-band hybridization and charge transfer and a lower dispersion contribution to the adsorption energy due to a smaller C-metal C_6 coefficient for Pd (Table 7.4.3). For metals with both

Table 7.4.3: Calculated B86bPBE-XDM carbon-metal C_6 dispersion coefficients (in a.u.), minimum-energy interlayer distances (in Å), and constrained adsorption energies (in kJ/mol C) for both (1×1) and $(\sqrt{3}\times\sqrt{3})$ surface unit cells of selected metals. Chemisorption states are denoted with a C and physisorption states are denoted with a P.

Metal	Orientation	Type	C_6 (a.u)	d (Å)	E_{ads}^{cons} (kJ/mol C)
Al	1×1 top-hcp	P	34.7	3.48	4.6
	$\sqrt{3}\times\sqrt{3}$	P	36.4	3.75	3.2
Cu	1×1 top-fcc	P	42.8	3.22	7.1
Ag	1×1 top-fcc	P	61.2	3.06	9.9
	$\sqrt{3}\times\sqrt{3}$	P	59.4	3.31	6.9
Au	1×1 top-fcc	P	60.3	3.22	7.7
	$\sqrt{3}\times\sqrt{3}$	P	56.5	3.41	6.4
Ni	1×1 top-fcc	C	39.3	2.22	7.8
	1×1 top-fcc	P	44.1	3.15	8.5
Pd	1×1 bridge-top	C	38.6	2.12	20.5
	$\sqrt{3}\times\sqrt{3}$	P	43.1	3.24	6.3
Pt	1×1 bridge-top	C	45.9	2.10	14.6
	1×1 top-fcc	P	54.3	3.22	7.6
	$\sqrt{3}\times\sqrt{3}$	P	51.5	3.44	6.8

chemisorbed and physisorbed minima, the C_6's are typically smaller for the former, because of the partial positive charge on the surface atoms that result from metal-graphene charge transfer. Lastly, the carbon-metal dispersion coefficients are slightly larger for physisorbed minima in the (1×1) cell than for the $(\sqrt{3}\times\sqrt{3})$ cell due to the larger lattice constants in the former, which result in stretched C-C bonds.

7.4.4 Charge Transfer

QTAIM results for the extent of metal-to-graphene charge transfer are presented in Table 7.4.4. Generally the extent of charge transfer is inversely related to the graphene-surface distance, with the 1×1 bridge-top orientation giving the largest charge transfer, followed by 1×1 top-fcc. In our previous work on Ni, only the chemisorbed orientations showed significant charge transfer[272] and the present results indicate negligible charge transfer for all physisorption minima in the $(\sqrt{3}\times\sqrt{3})$ cell. However, considerable charge transfer is seen for several ph-

Table 7.4.4: Charge transfer from the metal to the graphene layer (per C) obtained from QTAIM analysis of the B86bPBE electron densities.

Metal		bridge-fcc	bridge-hcp	bridge-top	fcc-hcp	top-fcc	top-hcp	$\sqrt{3} \times \sqrt{3}$
Al	P	0.019	0.020	0.022	0.018	0.020	0.024	0.008
Cu	P	0.003	0.003	0.004	0.003	0.005	0.004	–
Ag	P	0.021	0.021	0.022	0.023	0.023	0.021	0.008
Au	P	0.008	0.008	0.009	0.007	0.010	0.010	0.000
Ni	C	–	–	0.054	–	0.047	0.042	–
	P	0.003	0.003	0.003	0.003	0.004	0.003	–
Pd	C	0.044	0.043	0.051	–	0.043	0.040	–
	P	–	–	–	0.004	–	–	0.000
Pt	C	–	–	0.049	–	0.028	0.024	–
	P	0.000	0.000	0.000	0.001	0.001	0.000	-0.006

ysisorption minima in the (1×1) unit cell of metals other than Ni, particularly for Al and Ag (which have the lowest work functions), indicating that the stretched C-C bonds make charge transfer more favorable. This result explains why the PES in Figure 7.4.1 show significantly less adsorption for Al and Ag in the $(\sqrt{3} \times \sqrt{3})$ configuration as compared to (1×1) fcc-hcp.

Pd has the largest charge transfer of all metals; taken together with its relatively low dispersion coefficient (Table 7.4.3) and its readiness to form covalent bonds to graphene's p orbitals, this explains the presence of only a single deep chemisorption minimum for most (1×1) orientations. Generally, charge transfer from the metal is proportional to the interlayer distances and adsorption energies, with Pd>Pt>Ni. LEED studies have previously shown evidence of strong interactions between graphene and these metals in commensurate orientations.[34,262,265] Additionally, a tribology experiment[265] involving graphene on platinum has shown graphene interacts more strongly with the metal substrate under stress, suggesting that greater charge-transfer is achievable with even closer graphene-metal contacts.

7.4.5 Comparison with Previous Theory

Previous density-functional studies of graphene adsorption limited their scope to the (1×1) cell for Cu and Ni and the $(\sqrt{3} \times \sqrt{3})$ cell for other metals in order

Table 7.4.5: Constrained adsorption energies ($E_{\text{ads}}^{\text{cons}}$ in kJ/mol C) and interlayer distances (d in Å) for graphene on selected metal surfaces. Data for Cu and Ni is given for the top-fcc orientation of the (1×1) cell while all other metals use the $(\sqrt{3} \times \sqrt{3})$ cell. The B86bPBE-XDM results are from the present work, except for Ni, where the values are correspond to the chemisorbed minimum from Chapter 6; all other results are from the literature. Two sets of LDA results are given, using either relaxed[36] or experimental lattice parameters.[39]

		LDA[36,39]	vdW-DF2[37]	vdW-DF-C09[37]	RPA[39]	B86bPBE-XDM
Al	d	3.44, 3.46	–	–	3.51	3.75
	E_{ads}	2.41, 2.80	–	–	5.02	3.25
Cu	d	2.21, 3.21	3.73	2.94	3.09	3.22
	E_{ads}	3.38, 6.95	4.44	5.98	6.56	7.05
Ag	d	3.22, 3.32	3.73	3.23	3.31	3.31
	E_{ads}	2.89, 4.34	4.05	5.11	7.53	6.90
Au	d	3.32, 3.35	3.69	3.29	3.22	3.41
	E_{ads}	2.99, 3.28	4.73	5.69	9.17	6.40
Ni	d	2.00, 2.08	3.68	2.07	2.19	2.22
	E_{ads}	11.87, 18.14	4.25	13.60	6.75	7.79
Pd	d	2.33, 3.00	3.59	2.92	3.34	3.24
	E_{ads}	4.15, 7.62	5.02	6.95	8.68	6.34
Pt	d	3.25, 3.35	3.71	3.24	3.42	3.44
	E_{ads}	3.18, 3.47	5.21	6.56	8.10	6.81

to minimize C-C bond distortion. Our B86bPBE-XDM results for the minimum-energy graphene-metal separations and constrained adsorption energies are compared with selected results from previous theoretical studies in Table 7.4.5. Literature data is reported for the RPA,[39] two vdW-DF functionals[37] and the LDA.[36,39]

Table 7.4.5 shows that B86bPBE-XDM is in the closest agreement with RPA[39] for both interlayer distances and adsorption energies. This adds to our previous results showing excellent agreement between B86bPBE-XDM and the RPA for graphene adsorption on Ni[272] and for graphite exfoliation.[61,272]

The LDA tends to under-estimate the adsorption energies relative to both B86bPBE-XDM and the RPA for physisorption, as expected due to the neglect of dispersion. Additionally, the LDA predicts chemisorption minima for Cu and Pd, which are not present with either B86bPBE-XDM or the RPA, and the chemisorption energy on Ni is significantly over-estimated. The two sets of LDA results differ

significantly depending on whether relaxed lattice parameters[36] or experimental lattice parameters[39] were used in the calculations.

While several authors[36,37,39] have performed calculations on these systems with the original vdW-DF method,[133] we focus on the more-recent vdW-DF2[184] and vdW-DF-C09,[271] which are typically more accurate.[278] The vdW-DF2 results appear to systematically under-bind, predicting longer interlayer distances and lower adsorption energies than B86bPBE-XDM or the RPA. Conversely, vdW-DF-C09 significantly under-estimates the interlayer distances and, like the LDA, drastically overestimates the energy for graphene chemisorption on Ni.

7.4.6 Connection with Experiment

Our calculations along with previous experimental results,[33,34,88,261–265] and one LDA study,[268] suggest that the interaction between graphene and both Pd and Pt is strongly dependent on the graphene-metal orientation. Our calculated adsorption energies in Table 7.4.2 explain conflicting experimental observations that graphene forms both strong[33] and weak[261] interactions with the Pd surface. Notably, Murata *et al.*[34] observed a strong dependence on rotational orientation; the 30° orientation interacts weakly with the surface and the interaction strength is proportional to the alignment between the substrate and surface lattice constants. Similarly, it has been found that the lattice mismatch results in formation of graphene ripples on Pt surfaces, leading to strong local interactions,[32,262,263,265] but weak interactions overall.[88,264] While our results predict strong chemisorption of graphene in the bridge-top orientation of the (1×1) cell, the energy penalty due to C-C bond strain is prohibitive for graphene to adopt this orientation globally, in agreement with experiment.[263] However, our results suggest that strong chemisorption behavior is possible locally between individual carbon and Pd/Pt atoms, or between small domains with favorable atomic alignment. For physisorbed orientations of graphene on Pt, the global average interlayer distance was found to be 3.30 Å,[88] which is intermediate between the distances of 3.21

Å and 3.44 Å for the (1×1) and $(\sqrt{3} \times \sqrt{3})$ cells predicted by B86bPBE-XDM (Table 7.4.3).

In contrast to the Ni-group, the constrained results in Table 7.4.2 show that graphene physisorbs on each of the coinage metals regardless of the rotational orientation on the surface. This is consistent with LEED and STM experiments that have shown that graphene interacts with copper and gold weakly.[89,266,275,279,280] Also, the (1×1) constrained adsorption energies are generally greater than for the $(\sqrt{3} \times \sqrt{3})$ cell (Table 7.4.2). This is in agreement with experiments showing that graphene prefers the strained 0° orientation instead of the less-strained 30°-rotated Moiré pattern on Au. To minimize the C-C bond strain, the graphene sheet is observed to fold into a herringbone orientation.[89,266]

Our results suggest that there is a significant energetic drive for graphene to adopt an aligned on-top orientation on a substrate's surface. This interaction drives the initial Moiré structure formation until the graphene sheet grows large enough so that either the surface or graphene reconstruct globally to minimize the C-C bond strain, as occurs on Pd, Pt, and Au.

7.5 Summary

This chapter studied graphene adsorption on seven different (111) face-centered cubic metal surfaces (Al, Ni, Pd, Pt, Cu, Ag, and Au). The 0° orientation, corresponding to a (1×1) surface unit cell was studied for all seven metals, using six different graphene-metal geometries (top-fcc, top-hcp, fcc-hcp, bridge-top, bridge-hcp, and bridge-fcc, in the usual nomenclature[36,37,39,50,272]). In addition, the 30° orientation, corresponding to a $(\sqrt{3}\times\sqrt{3})$ surface unit cell, was also studied for all metals except Ni and Cu. The exchange-hole dipole moment (XDM) dispersion correction combined with the B86bPBE functional was used, and our calculations were compared to previous theoretical and experimental observations. In particular, excellent agreement is found between B86bPBE-XDM and reported RPA adsorption energies and graphene-metal distances.

Our results show that graphene-substrate interactions depend both on rotational orientation and lattice commensurability. Ni and Cu have lattices that match graphene in the (1×1) surface unit cell, whereas the remaining metals match with graphene in the $(\sqrt{3} \times \sqrt{3})$ cell. Surface adsorption is strongly unfavorable in the incommensurate orientations due to the high lattice strain. Experimentally, graphene can adopt rotational orientations with longer periodicity to reduce this lattice strain. However, to obtain proper energy rankings of Moiré patterns on these substrates, much larger unit cells than can be efficiently modeled with DFT are required.

To quantify physisorption and chemisorption effects as a function of graphene-metal distance, the lattice strain energy was eliminated from the adsorption energy by taking the graphene and metal contributions to correspond to an infinitely separated graphene sheet and metal surface, constrained to have equal lattice constants. This "constrained" adsorption energy is largest in the (1×1) unit cell, which maximizes direct on-top contacts between the graphene carbon atoms and underlying surface metal atoms. The results for the (1×1) cell showed that Pt displays both physisorption and chemisorption minima for the top-fcc, top-hcp, and bridge-top orientations. This behavior is similar to Ni, although the chemisorption interaction is stronger on Pt. Only chemisorption minima occur for Pd in the on-top orientations due to greater charge transfer and weaker dispersion interactions relative to Pt. Conversely, only physisorption is observed for the noble metals and Al, where there are only small energy differences on the order of ~ 1 kJ/mol C between the various (1×1) orientations. In the rotated $(\sqrt{3} \times \sqrt{3})$ cell, only physisorption minima are present for all metals considered. Because half of the graphene carbon atoms reside over voids, the $(\sqrt{3} \times \sqrt{3})$ adsorption PES resemble those for the fcc-hcp orientation of the (1×1) cell. The dispersion coefficients and adsorption-energy contributions are nearly invariant with respect to both graphene rotation and lateral translation, indicating that the changes in PES arise due to the presence or absence of direct C-metal contacts.

Our results indicate that there is a strong driving force for graphene to align with the surface, particularly for the Ni-group metals. This explains the observation that the 0° Moiré pattern is dominant on gold despite the high degree of C-C bond strain. Experimentally, it appears that the graphene's lattice strain is reduced by adoption of a herringbone orientation on the surface.[89,266] The energetic drive for local surface-substrate alignment, along with incommensurate graphene-metal lattice constants is the likely cause for formation of multiple Moiré patterns on metal surfaces. In particular, the combination of the strong chemisorption seen on Pd and Pt in the incommensurate (1×1) cell and weak physisorption in the commensurate $(\sqrt{3} \times \sqrt{3})$ cell explains experimental observations that graphene has multiple Moiré patterns on Pd and Pt, forming strong interactions locally, but weak interactions globally.[28,34,261,263,264]

Chapter 8: Effect of the Metal Substrate on Interlayer Interactions in Bilayer Graphene

Original reference: M. S. Christian and E. R. Johnson, J. Phys. Chem. C (2018) doi:10.1021/acs.jpcc.7b12743.

8.1 Abstract

Bilayer graphene (BLG) has been shown to have advantageous electronic and physical properties relative to single-layer graphene (SLG) and is a model system for probing the tribology of graphene-based lubricants. However, few studies have investigated how metal substrates affect interlayer interactions, as quantified by the exfoliation energy and the sliding barrier of the upper graphene layer. In this work, we present a study of adsorbed BLG on several transition-metal surfaces using density-functional theory (DFT) incorporating the exchange-hole dipole moment (XDM) dispersion model. Our results show that physisorption of BLG on a surface does not significantly perturb the interlayer interactions, exfoliation, or sliding. Conversely, chemisorption of BLG increases the exfoliation energy and decreases the sliding barriers due to stronger dispersion contributions from the metal substrate. Changes in translational and rotational orientations massively impact the sliding friction for Ni-group metals that can facilitate both chemisorption and physisorption.

8.2 Introduction

Due to its unique two-dimensional electronic structure, graphene has attracted a great deal of recent attention for its wide range of of potential device applica-

tions. A common route to graphene synthesis involves chemical vapor deposition on metal substrates, which can result in formation of adsorbed single-layer graphene (SLG) or bilayer graphene (BLG).[20,22,223,224,226,252] Few-layer graphene is an excellent friction modifier for metal contacts as its properties lead to a high lubricity, reducing the sliding barrier relative to that of the unadorned bimetallic interface.[9,219,220]

The interaction of graphene with metal surfaces varies with substrate type and lattice commensurability.[20,30] Graphene can either physisorb, bound by weak dispersion interactions,[86,89,281] or chemisorb, bound by a combination of electrostatic and dispersion interactions.[87,275] Physisorption is characterized by SLG–metal interlayer distances of >3Å and effectively zero charge transfer, as occurs for Al and the Cu-group metals.[282] Alternatively, graphene can either physisorb on chemisorb on Ni-group metals, depending on the rotational orientation. Chemisorption is characterized by interlayer distances of < 2.5Å and significant charge transfer.[282]

Tribologists have studied substrate effects on bilayer sliding,[41,42,46,95,96,283,284] demonstrating that the energy barriers are dependent on the number of graphene layers and on the strength of their surface adhesion. In general, the friction tends to decrease with increasing numbers of layers,[41,42] as this increases the smoothness of the graphene. Similarly, strong interactions with the substrate result in smoother graphene layers and decrease the sliding barrier, while weak interactions lead to increased roughness or corrugation and cause greater friction.[42,46,96] However, relatively little is known regarding how an underlying metal substrate can affect the adsorption and frictional properties of the upper graphene layer in adsorbed BLG beyond such changes in roughness.

Investigations of friction on highly-planar graphene surfaces can be conducted using a quartz crystal microbalance (QCM), rather than by atomic force microscopy (AFM) where the tip causes graphene wrinkling. QCM studies have examined adsorption and friction of noble-gas atoms on graphene/Ni(111) surfaces[102] and found the effect of the underlying substrate to be negligible.[101] How-

ever, this is at odds with combined DFT and Raman-spectroscopy results that a hexagonal boron nitride substrate strengthens the adsorption of molecular bromine on graphene.[285] Additionally, a further QCM study found a significantly greater interaction strength between gold nanocrystals a graphite substrate compared to SLG graphene.[286]

Several previous computational studies investigated BLG adsorbed on various metal surfaces, but either concentrated on carbon-metal distances and energies rather than interactions between the graphene layers,[48,287] or used the local density approximation,[288] which lacks a treatment of dispersion interactions needed to describe these systems. A study of BLG adsorbed on the Cu and Ni (111) surfaces using PBE functional[126] and the D2 dispersion correction[57] found that the interlayer interaction is significantly stronger on Ni, relative to freestanding BLG.[289] Another PBE-D2 study found that a Ni(111) substrate both increases interlayer adhesion and decreases the lateral sliding force for trilayer graphene.[219]

Use of a density-dependent dispersion correction has been shown to yield far more accurate graphene-metal distances and energetics[272,282] than the empirical dispersion corrections used in previous BLG studies.[219,289] The exchange-hole dipole moment (XDM) model,[60,273] is a non-empirical dispersion correction that uses the electron density to generate C_6 (and higher-order) dispersion coefficients. These dispersion coefficients are used to evaluate the dispersion energy between all pairs of atoms, i and j:

$$E_{\mathrm{XDM}} = -\frac{1}{2}\sum_{n=6,8,10}\sum_{i\neq j}\frac{C_{n,ij}f_n(R_{ij})}{R_{ij}^n}, \tag{8.2.1}$$

where R_{ij} is the interatomic distance and f_n is a damping function that attenuates the dispersion correction at short range. Each pairwise-atomic dispersion coefficient, $C_{n,ij}$, is determined from integrals involving the exchange-hole multipole moments for the interacting atoms, as well as the atom-in-molecule polarizabilities. The XDM dispersion energy is added to the base DFT energy as a post-SCF

correction:

$$E = E_{\text{base}} + E_{\text{XDM}}. \tag{8.2.2}$$

The non-empirical and environment-dependent nature of the dispersion coefficients allows XDM to model dispersion interactions accurately for diverse systems ranging from molecular dimers to supra-molecular systems to organic crystals.[273] Most relevant to this paper, XDM has been shown to accurately model physisorption of molecules[64] and of SLG[272,282] on metal surfaces.

This article is the first to systematically consider substrate effects on bilayer graphene for the late transition metals with state-of-the-art dispersion-corrected DFT methods. It represents the third part of an investigative series on graphene-metal interactions using DFT paired with the XDM dispersion correction.[272,282] In this work, we investigate if and how metal substrates affect BLG interfacial distances and interaction energies, as well as energy barriers for interlayer sliding. In the first section, we compare properties of BLG with graphite as a reference to gauge how the graphite substrate affects BLG energies and distances. In the remainder of the article, we consider BLG adsorbed on the (111) surface for seven metals in two rotational orientations. The second section assesses how the metal substrates affect exfoliation energies for the upper graphene layer, while the third section investigates how the substrates affect the energy barriers for interlayer sliding of the adsorbed BLG. Our results show that the substrate does significantly affect the energetics and interlayer distances of BLG for cases where the lower graphene layer is chemisorbed on the metal due to stronger dispersion attraction between the substrate surface and the upper graphene layer.

8.3 Computational Methods

As in our previous publications on graphene-metal interactions,[272,282] all DFT calculations were carried out using periodic boundary conditions with the projector augmented wave (PAW) formalism[114] as implemented in Quantum ESPRESSO.[179]

The B86bPBE[180] exchange-correlation functional was used as it provides the best accuracy when paired with the XDM dispersion model.[61,151] PAW datasets were generated using LD1 version 4.3.2 using pslibrary 0.2.5 inputs. The datasets also included scalar relativistic effects and non-linear core corrections.[181] All datasets were checked to ensure that there was no PAW sphere overlap for each optimized geometry. An $8 \times 8 \times 1$ Γ-centered **k**-point grid was used, with a plane-wave cutoff of 60 Ry and a density expansion cutoff of 800 Ry. Cold smearing[108] was employed with a smearing parameter of 0.01 Ry.

The metal substrates considered here are the same as in our previous paper:[282] aluminum, copper, silver, gold, nickel, palladium, and platinum. Calculations for the Ni-group metals used an initial spin-polarization and were checked for convergence to the correct spin state. All metals have a face-centered cubic (fcc) crystal structure and we consider only the (111) surface. The 0° and 30° rotational orientations, or Moiré patterns, are considered for all cases except for Cu and Ni, where only the 0° orientation is considered due to the excessive compression of the adsorbed graphene that would occur in the 30° orientation.[282] The (1×1) surface unit cell is used for the 0° orientation, where the lattice vector of graphene and the metal are aligned, and the $(\sqrt{3} \times \sqrt{3})$ unit cell is used for the 30° orientation, where the graphene surface vector is rotated about the metal lattice vector by this angle. Adsorption of graphene in the 30° orientation is more stable for Al, Ag, Au, Pd, and Pt due to better lattice commensurability. However, this orientation does not allow for chemisorption, which occurs in the 0° case for Pd and Pt.[282] While many other Moiré patterns are possible experimentally, they would require much larger units cells in the DFT modeling and hence are not considered.

For the (1×1) cell, six unique translational orientations of SLG graphene layer, with respect to the metal, are possible.[282] In this work, only the minimum-energy of these orientations are considered and were used to define the configuration of the lower graphene layer in contact with the surface. These are top-hcp for Al; top-fcc for Ni, Cu, Ag, and Au; and bridge-top for Pd and Pt.[282] For nickel, we

consider the chemisorption minimum favored after inclusion of thermal-expansion effects.[272] Additionally, we also studied the chemisorbed top-fcc orientations of graphene for Pd and Pt in the (1×1) cell for consistency with the other metals and because graphene has been seen to have a combination of the bridge-top and top-fcc orientations experimentally.[88,261,262,264] Finally, calculations were also performed for freestanding BLG and for BLG adsorbed on a graphite surface.

Each surface is modeled as a slab containing six layers of metal atoms, or six layers of carbon atoms for the graphite substrate. A sufficiently large vacuum region was inserted between the slabs to separate the periodic images, yielding unit-cells 70 Bohr in length. BLG is adsorbed on the surface, with the lower layer in the orientations described above. The carbon-metal distances for this layer were set to the optimum values from our previous paper[282] and were held fixed in all subsequent calculations to simplify computation of the exfoliation and sliding potential-energy surfaces (PES). For each combined BLG-metal system, the (x, y)-unit-cell dimensions, which control the surface lattice constants, were systematically varied in 0.01 Å increments and the minimum-energy geometry obtained from quadratic interpolation. These optimum values of the lattice constants are given in Table 8.3.1 and were also held fixed in all subsequent PES calculations. Alternatively, instead of optimizing the lattice constant for the combined BLG-metal system, PES were also generated using substrate lattice constants fixed to the experimental values (see Table 7.4.1); the results are effectively identical and are presented for comparison in Appendix D.

Table 8.3.1 shows a comparison of the optimum lattice constants for the combined BLG-metal system with those of freestanding BLG, which demonstrates the magnitude of the lattice strain. The strain energies resulting from this lattice distortion for a single graphene layer, also reported in Table 8.3.1, are

$$E_{\text{strain}} = E_{\text{SLG}}(a_{\text{surf}}) - E_{\text{SLG}}, \tag{8.3.1}$$

where the latter value corresponds to the minimum energy for SLG. The values of

Table 8.3.1: Comparison of calculated surface lattice constants (a_{surf} in Å) for BLG adsorbed on the (111) surface of selected metals for the (1×1) and $(\sqrt{3} \times \sqrt{3})$ unit cells. Also shown are the differences in lattice constant, relative to graphite (Δa_{surf} in Å), and the strain energies resulting from the changes in lattice constant for a single-layer graphene (E_{strain} in kJ/mol per C).

Metal	(1×1)			$(\sqrt{3} \times \sqrt{3})$		
	a_{surf}	Δa_{surf}	E_{strain}	a_{surf}	Δa_{surf}	E_{strain}
Al	2.66	0.19	33.9	4.95	0.00	0.1
Cu	2.51	0.04	1.8	—	—	—
Ag	2.76	0.29	68.0	4.98	0.03	1.2
Au	2.80	0.33	88.0	5.02	0.07	2.2
Ni	2.47	0.00	0.1	—	—	—
Pd	2.71[a]	0.24[a]	47.7	4.88	-0.07	0.7
	2.70[b]	0.23[b]	46.0			
Pt	2.75[a]	0.28[a]	64.1	4.90	-0.05	0.5
	2.74[b]	0.27[b]	60.1			
SLG	2.47			4.95		

The lower graphene layer is: [a]chemisorbed, bridge-top; [b]chemisorbed, top-fcc.

the strain energy are quite high for Al, Ag, Au, Pd, and Pt in the (1×1) cell (or 0° Moiré pattern), where there is a large lattice mismatch. However, these aligned orientations are still considered as they facilitate graphene chemisorption[282] and are seen experimentally for Au, Pd, and Pt, where the graphene distorts over large length scales to reduce the lattice strain.[32–34,89,262,263,265,266]

Potential energy curves for adsorption/exfoliation of the upper graphene layer were computed to assess the strength of the BLG interlayer interaction for all substrates. The exfoliation PES were generated by translating the upper graphene layer in the z-direction, with respect to the surface, while fixing all other geometric parameters. The adsorption energy of the upper graphene layer is defined relative to the infinitely-separated, strained components, as in our previous paper.[282] Potential energy surfaces for interlayer sliding of BLG were also computed for all substrates and orientations. Starting from the minimum-energy structures, the top graphene layer was translated diagonally across the unit cell to generate the PES. This allows for the entire sliding PES to be sampled while minimizing the number of calculations by exploiting graphene's symmetry. For each point,

the z-position of the upper graphene layer was varied in 0.05 Å increments and the minimum-energy PES obtained from quadratic interpolation. Because we are interested in the relative energies along the sliding PES, we define the energies with respect to the most stable geometry for each substrate.

8.4 Results and Discussion

8.4.1 Comparison of Bilayer Graphene versus Graphite

We begin by considering the differences between BLG and graphite as a reference to understand basic substrate effects. Figure 8.4.1(a) shows a comparison of the potential energy surfaces for exfoliation of the upper graphene layer in BLG and in graphite, while Figure 8.4.1(b) shows a decomposition of these PES into base-functional and dispersion contributions. The base-functional contribution is entirely repulsive along the PES, as expected from analogy to the benzene dimer.[164] The base-functional contribution can be thought of as describing the Pauli repulsion between the graphene sheets and is off-set by dispersion to give adsorption in the overall PES. From Figure 8.4.1(a), the magnitude of the exfoliation energy for BLG is 0.5 kJ/mol C less than for the graphite slab, demonstrating that the graphite support causes stronger interlayer binding. Figure 8.4.1(b) reveals that the increased binding is due to additional dispersion interactions with the underlying substrate in the graphite case. This is in agreement with a combined QCM and molecular-dynamics study that found that a reduced Lennard-Jones interaction strength was needed to reproduce experimental results for a graphene substrate, relative to graphite.[286] The stronger binding also affects the equilibrium interlayer distance; the distance between the top two layers of the graphite slab is 3.37 Å, intermediate between the values of 3.39 Å in BLG and 3.35 Å in bulk graphite.

Figure 8.4.1(c) shows a comparison of the potential energy surfaces for sliding of the upper graphene layer in BLG and on the graphite surface. Both of the PES show two minima, which are equivalent for BLG and nearly degenerate for

Figure 8.4.1: Comparison of the potential energy surfaces for (a) exfoliation and (c) sliding of the upper graphene layer in BLG and on a graphite surface. In (b) and (d), the PES are decomposed in to the XDM-dispersion (solid lines) and base-functional (dashed lines) contributions.

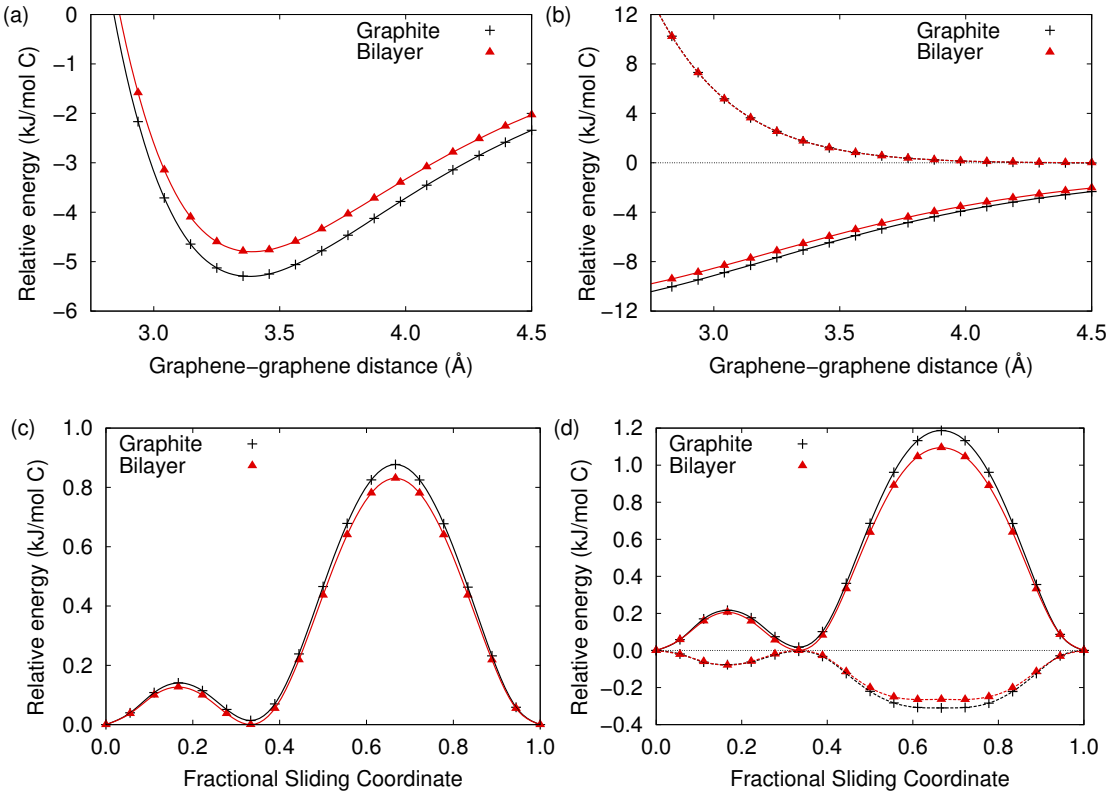

Figure 8.4.2: Geometries of three extrema on the sliding PES for graphite. The top two graphene layers are shown in the "tube" representation; black is the upper layer and grey the lower layer. The underlying substrate is represented by the "ball" motif. The green atoms constitute the third carbon layer, or the top of the graphite substrate. The purple atoms are the fourth carbon layer, or the second layer of the graphite substrate.

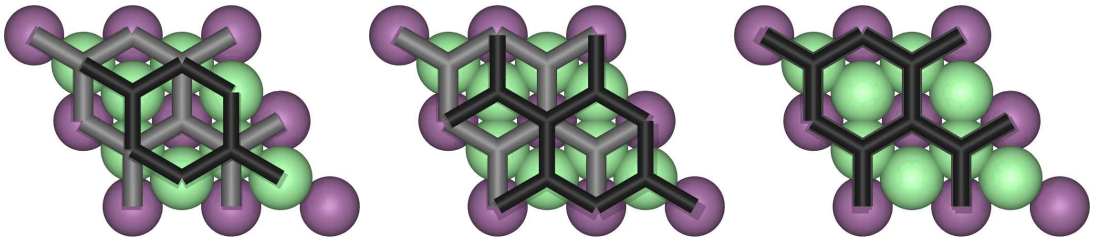

(a) global minimum (b) local minimum (c) maximum

graphite. The global minimum-energy configuration, shown in Figure 8.4.2(a), corresponds to the zero of energy for the interlayer-sliding PES. For graphite, this is the "ABA" Bernal stacking seen experimentally.[290,291] The local minimum corresponds to "ABC" stacking, shown in Figure 8.4.2(b), and occurs one third of the way along the fractional sliding coordinate. ABC stacking is marginally higher in energy than ABA stacking due to slightly weaker dispersion stabilization. The maximum-energy point on the sliding PES occurs two thirds of the way along the fractional sliding coordinate. As shown in Figure 8.4.2(c), this transition state has "AA" stacking, where the top two graphene layers are exactly aligned.

The sliding PES are decomposed into base-functional and dispersion contributions in Figure 8.4.1(d). Note that this plot shows the various energy terms at the B86bPBE-XDM optimized geometries and will not match the sliding potential for an uncorrected generalized-gradient functional in the absence of a dispersion correction. The figure reveals that the sliding barrier is primarily controlled by the XDM dispersion contribution. The AA orientation, where the carbon atoms in the two graphene sheets lie directly above each other (as in Figure 8.4.2(c)), gives rise to less dispersion attraction than when they are staggered, as in the AB orientations shown in Figure 8.4.2(a,b). The dispersion-only barrier is even somewhat higher than the overall barrier because the base functional contribution favors the stacked AA orientation. To understand the reason for this behavior,

recall from Figure 8.4.1(b) that the base-functional contribution to the adsorption energy is purely repulsive at all points along the PES, while the dispersion contribution is purely attractive. At the local minima (AB orientations) on the sliding PES, there is greater dispersion binding, leading to a shorter interlayer distance (3.37Å for graphite and 3.38Å for BLG), and this is offset by greater repulsion from the base functional. Conversely, at the maximum (AA orientation), there is less dispersion binding, leading to a longer interlayer distance (3.57Å for graphite and 3.58Å for BLG), so this results in less repulsion from the base functional.

From Figure 8.4.1(c,d), the graphite substrate does not significantly affect the sliding PES. The upper graphene layer is far enough from the substrate that the additional dispersion attraction from interaction with the support is largely invariant with respect to its translation. This result is expected since it is well established that graphene rippling, and not other electronic effects, is the dominant factor that causes the observed reduction in interlayer friction with increasing numbers of graphene layers.[41,42,96]

8.4.2 Exfoliation

The previous section showed that a graphite base increases the BLG exfoliation energy. In this section, we investigate the exfoliation energy of the upper graphene layer of BLG adsorbed on the various metal surfaces. The resulting interlayer distances and exfoliation energies are reported in Table 8.4.1 and the exfoliation PES are illustrated in the first column of Figure 8.4.3. Results for graphite are also included as a reference to gauge how each metal affects the exfoliation energy. The dispersion energies along the PES for interactions between the upper graphene layer and the metal are shown in the second column of Figure 8.4.3. These results are expressed relative to analogous energies for graphite, where only the interaction between the upper layer and the substrate base are included in the dispersion energy. As such, the curves represent the additional dispersion stabilization gained by replacing the graphite substrate with a given metal surface.

Table 8.4.1: Optimum BLG interlayer distances (d_{BLG}), distances between the top graphene layer and the upper layer of the metal surface ($d_{\mathrm{M-top}}$), and graphene adsorption energies (E_{ads}). Relative values, with respect to results for the graphite surface, are also shown. All distances are given in Å and all energies in kJ/mol C.

		d_{BLG}	Δd_{BLG}	$d_{\mathrm{M-top}}$	$\Delta d_{\mathrm{M-top}}$	E_{ads}	ΔE_{ads}
Al	1×1 top-hcp	3.39	0.02	6.87	0.38	5.1	-0.2
	$\sqrt{3} \times \sqrt{3}$	3.37	0.00	7.12	0.63	5.0	-0.3
Cu	1×1 top-fcc	3.38	0.01	6.60	0.11	5.3	0.0
Ag	1×1 top-fcc	3.39	0.02	6.45	-0.04	5.4	0.1
	$\sqrt{3} \times \sqrt{3}$	3.37	-0.01	6.68	0.19	5.3	0.0
Au	1×1 top-fcc	3.40	0.03	6.62	0.13	5.4	0.1
	$\sqrt{3} \times \sqrt{3}$	3.38	0.01	6.79	0.30	5.5	0.2
Ni	1×1 top-fcc	3.29	-0.08	5.51	-0.98	6.2	0.9
Pd	1×1 bridge-top	3.33	-0.04	5.45	-1.04	5.9	0.6
	1×1 top-fcc	3.32	-0.05	5.57	-0.92	5.9	0.6
	$\sqrt{3} \times \sqrt{3}$	3.36	-0.01	6.60	0.11	5.5	0.2
Pt	1×1 bridge-top	3.30	-0.07	5.40	-1.09	6.3	1.0
	1×1 top-fcc	3.30	-0.07	5.70	-0.79	6.0	0.7
	$\sqrt{3} \times \sqrt{3}$	3.36	-0.01	6.80	0.31	5.4	0.1
BLG		3.39	0.02	—	—	4.8	-0.5
Graphite		3.37	—	6.49	—	5.3	—

The results in Table 8.4.1 show that the interlayer distances and energies are nearly equivalent for all metals in the $(\sqrt{3}\times\sqrt{3})$ cell. All BLG distances are within 0.01 Å of graphite and most exfoliation energies are similar to graphite, differing by no more than 0.3 kJ/mol C. The dispersion contributions from the substrate are also quite similar to graphite, except for Al, which has the lowest dispersion coefficient of the metals considered here.[282]

The results for physisorbed BLG in the (1×1) cell are similar to those for the $(\sqrt{3}\times\sqrt{3})$ cell; the exfoliation energies and distances, again, vary little from those seen for graphite. The dispersion contributions follow the same ordering as the C_6 dispersion coefficients for the metals,[282] namely Al < Cu < Au < Ag. The C_6 coefficients increase down the periodic group, except for gold, where relativistic effects increase the electronegativity and reduce the dispersion coefficient.[149] The slight increases in the surface dispersion contributions relative to graphite (between 0.2-0.4 kJ/mol per C) are offset by the increased graphene strain in this cell,

Figure 8.4.3: PES for exfoliation of graphene from a graphene-metal or graphite base (left column). Also shown are dispersion energies for interaction between the exfoliated graphene layer and the metal slab, relative to analogous values for graphite (right column).

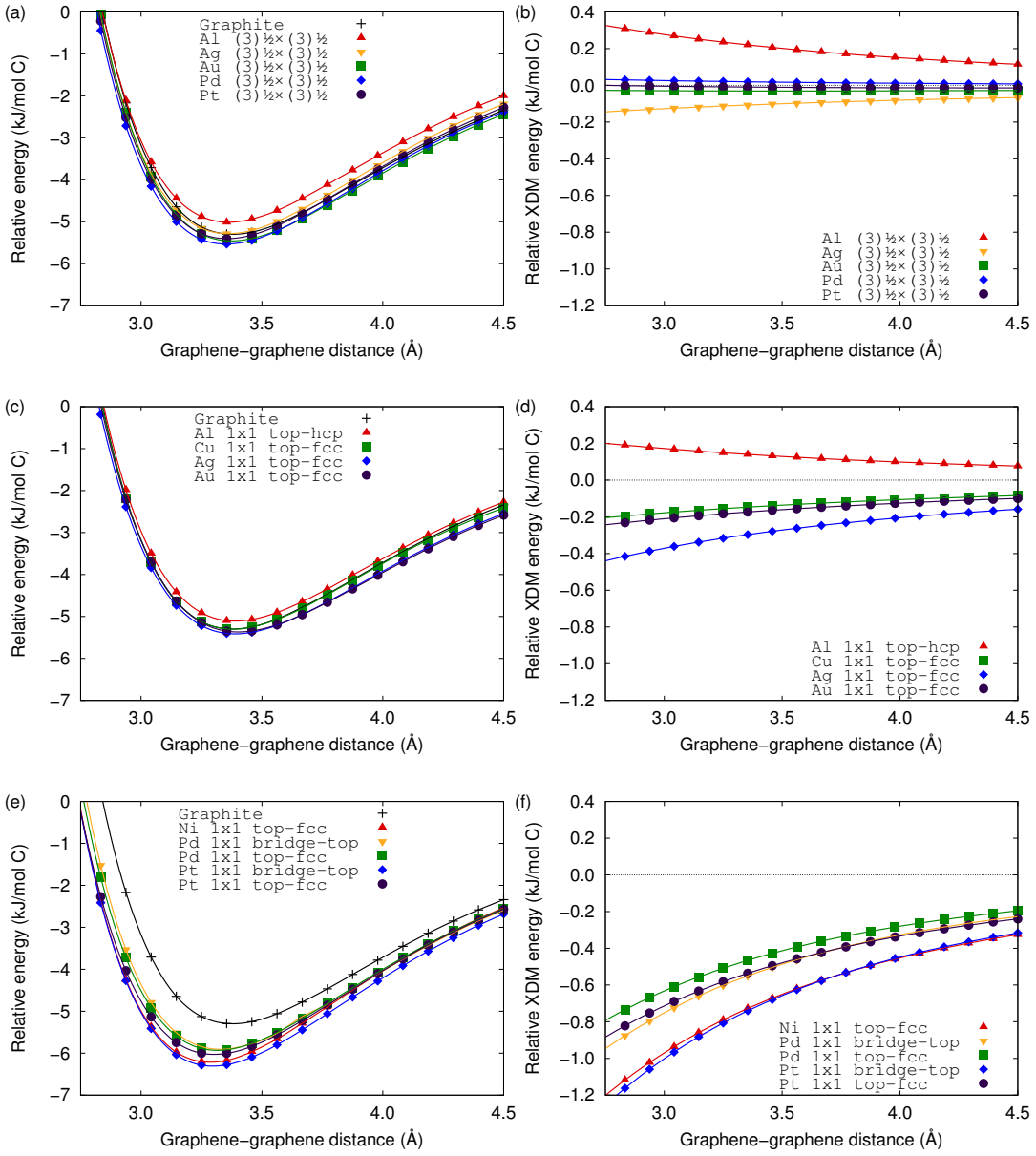

resulting in negligible overall changes in the exfoliation PES. Thus, our results show that rotational orientation and lattice commensurability have little affect on BLG exfoliation energies when the BLG is physisorbed on Cu-group metals.

Graphene chemisorbs on Ni, Pd and Pt in the (1×1) cell and, therefore, the graphene-metal interlayer distances are much shorter for these metals.[272] Figure 8.4.3 and Table 8.4.1 show that the exfoliation energies are somewhat higher when BLG is adsorbed on these metals, by up to 1 kJ/mol C for Pt when the

lower graphene layer is chemisorbed in the bridge-top orientation. The stronger interlayer interactions also manifest in the BLG interlayer distances, which are up to 0.08 Å shorter than in graphite. The additional binding can be attributed to a higher dispersion contribution from the substrate, due to the much shorter distances between the top graphene layer and the surface (0.8-1.1 Å in Table 8.4.1). Thus, dispersion contributions from the underlying substrate can significantly affect the strength of the interlayer interactions in BLG when it is chemisorbed on a metal surface; such substrates should not be neglected in computational modeling.

Finally, we compare our results with those of Wang *et al.*[289] obtained using PBE-D2,[57,126] who reported exfoliation energies of 5.8, 4.8, and 8.2 kJ/mol C for freestanding BLG and BLG adsorbed on Cu and Ni substrates, respectively. Their result for freestanding BLG is counter-intuitive as it is not physical to have a weakening of the BLG interlayer interaction when it is adsorbed on a substrate. In the limit of extremely weak adsorption, the substrate would have no effect, and the lower bound for the interlayer interaction energy would match that of freestanding BLG. For stronger adsorption, the substrate will contribute additional dispersion interactions to the interlayer binding, so the interlayer interaction energy must increase. To test their prediction, we calculated the exfoliation energy of freestanding BLG with PBE-D2 and obtained a value of 4.8 kJ/mol C, in agreement with our B86bPBE-XDM value in Table 8.4.1, as well with the result of Ref. 289 for BLG on Cu. We conjecture that the reported values in Ref. 289 for freestanding BLG and for BLG adsorbed on the Cu surface may have been switched accidentally. If this were indeed the case, the PBE-D2 exfoliation energy for BLG on Cu would be slightly higher than the corresponding XDM result, which is reasonable given the tendency of the D2 method to overestimate dispersion interactions for metals.[64] For BLG adsorbed on Ni, our calculated interlayer interaction energy is 2 kJ/mol C lower than that obtained in Ref. 289. This is expected due to the tendency of the empirical D2 method to overestimate dispersion interactions with Ni due to an overestimated Ni-C C_6 dispersion coefficient (75.4 a.u. with D2[57]

versus 39.3 a.u. with XDM[282]). This overestimation of C_6 will cause the "extra" dispersion contribution from the substrate to be overestimated, explaining the difference between the two sets of results.

8.4.3 Graphene Sliding

Graphene sliding PES are reported on the left side of Figure 8.4.4; the panels on the right show only the XDM dispersion contribution to the sliding PES. Figure 8.4.4(a) shows the PES for interlayer sliding of BLG adsorbed on metal substrates in the $(\sqrt{3} \times \sqrt{3})$ cell. The computed sliding barrier is highest for gold, which has the largest lattice mismatch with BLG, as shown in Table 8.3.1.

To investigate the effect of lattice mismatch on the sliding barriers, additional calculations were performed on freestanding BLG with a series of lattice constants spanning the full range of a_{surf} values listed in Table 8.3.1. The results are illustrated by a 2D representation of the sliding PES as a function of the lattice constant in Figure 8.4.5(a). The figure shows that stretching of the graphene lattice constant beyond the equilibrium value of 2.47 Å serves to increase the sliding barrier (from 0.8 kJ/mol C to 1.1 kJ/mol C over the range considered). Figures 8.4.5(b,c) present the decomposition of the 2D PES into base-functional and dispersion contributions. The dispersion contribution to the barrier is largely constant and the increase in sliding barrier with lattice constant is shown to originate from changes in the base-functional repulsion between the layers. Stretching the lattice constant beyond the BLG equilibrium value decreases base-functional repulsion between the graphene layers for the minimum-energy AB configuration, but increases base-functional repulsion for the maximum-energy AA configuration. The net result is a higher sliding barrier due this change in the base-functional contribution.

As shown in Figure 8.4.4(c), the sliding PES for the (1×1) cell exhibit a larger spread between the various metals than for the $(\sqrt{3} \times \sqrt{3})$ cell. This occurs because of the greater range of lattice constants and increasing strain for BLG

Figure 8.4.4: PES for sliding of the upper graphene layer over a fixed graphene-metal or graphite base, along the long diagonal of the unit cell, with the z-position of the translated layer allowed to relax. The left column shows the total sliding PES and the right column shows the XDM dispersion contribution only; both are relative to the lowest-energy orientation.

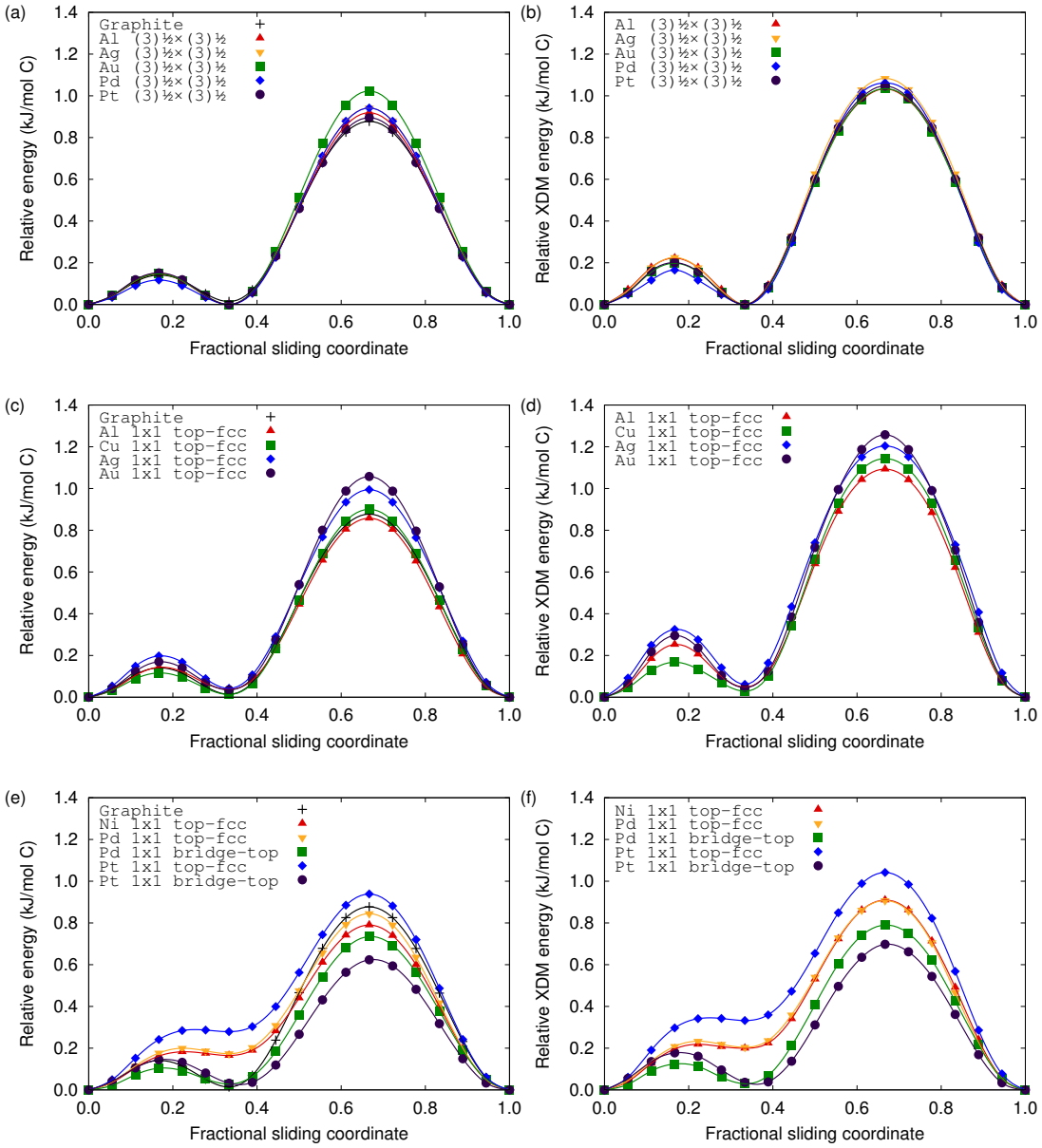

on the (1×1) surfaces (see Table 8.3.1). Physisorption on the (1×1) Ag and Au surfaces causes the greatest lattice mismatch and hence the highest sliding barriers. Conversely, for Cu in the (1×1) cell, there is almost no lattice mismatch and, consequently, the sliding barrier for BLG on this surface is almost identical to that for graphite. Al has an intermediate lattice mismatch, but the increase in barrier from the base functional is offset by a lower dispersion contribution, as

Figure 8.4.5: 2D PES illustrating the dependence of BLG interlayer sliding on the lattice constant. The total BLG interaction energy (a), as well as the XDM-dispersion (b), and base-functional (c) contributions are shown.

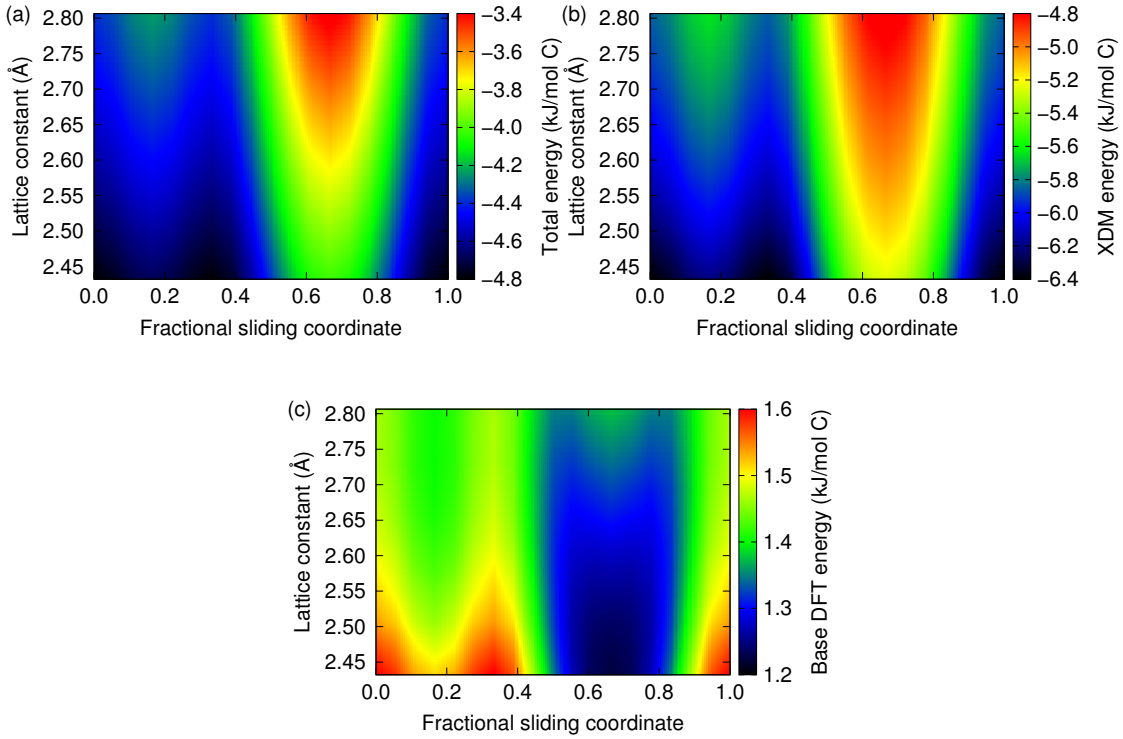

shown in Figure 8.4.4(d) and as expected due to the reduced dispersion binding for BLG on Al compared to the other metals.

The PES shown in Figure 8.4.4(e), for cases where BLG is chemisorbed on the metal substrate in the top-fcc orientation, are significantly different than those discussed above. The global and local minima, shown in Figure 8.4.6(a,b), are no longer nearly degenerate. Rather, the local minimum, in which the upper graphene layer is translated one third of the way across the unit cell, is significantly higher in energy. At the local minimum, the carbon atoms of the upper graphene layer lie directly above the surface metal atoms. This can be contrasted with the global minimum, where the carbons of the upper layer lie between the surface metal atoms. The latter arrangement results in more close carbon-metal contacts and consequently greater dispersion stabilization. However, it is only for the chemisorbed cases where the upper graphene layer is sufficiently close to the surface (see Table 8.4.1) for this difference to be significant. The destabilization of the local minimum is not seen for the bridge-top orientations as this breaks

Figure 8.4.6: Geometries of the extrema on the sliding PES for BLG adsorbed on Cu in the top-fcc orientation (top row) or Pt in the bridge-top orientation (bottom row). The top two graphene layers are shown in the "tube" representation; black is the upper layer and grey the lower layer. The underlying substrate is represented by the "ball" motif.

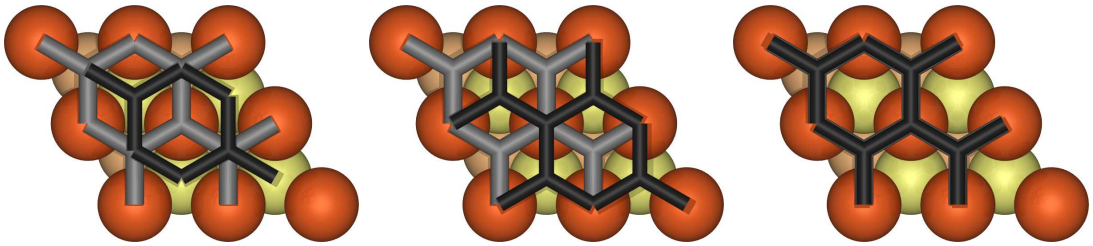

(a) top-fcc, global min (b) top-fcc, min (c) top-fcc, max

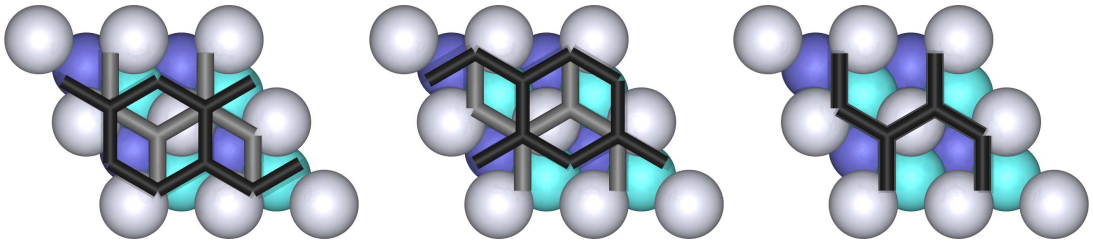

(d) bridge-top, global min (e) bridge-top, local min (f) bridge-top, max

the symmetry between the lower graphene layer and the surface. The global and local minima, shown in Figure 8.4.6(d,e), are nearly degenerate. In the first case the C-C bonds lie above metal atoms of the second surface layer (cyan) resulting in greater stabilization from dispersion interactions, while in the second case, the C-C bonds lie above the metal atoms of the third surface row (dark blue).

For the chemisorbed cases (Figure 8.4.4(e)) the sliding energy barriers are much lower than for the physisorbed cases and this arises from the dispersion contribution (Figure 8.4.4(f)). The additional dispersion from the substrate causes a reduction in the graphene interlayer distance, by 0.08 Å or less at the minimum-energy configuration. At the maximum-energy configuration, the contraction in the interlayer distance is as much as 0.18 Å. This reduction in the interlayer distance serves to preferentially increase the dispersion attraction between the two graphene layers at the maximum-energy configuration, lowering the barrier. The finding that chemisorption of BLG on a metal surface simultaneously increases the interlayer adhesion and decreases the sliding friction is a generalization of the previous PBE-D2 results for Ni(111) in Ref. 219.

The sliding barriers for chemisorbed BLG are also particularly sensitive to the translational orientation of the lower graphene layer with respect to the surface. Relative to the top-fcc orientation discussed above, the sliding barriers are further reduced for the bridge-top orientation, due to more preferable dispersion interactions between the top graphene layer and the metal surface at the transition state. For the top-fcc orientation, the transition state has an all-aligned AAA configuration for the BLG and top layer of surface atoms, as in Figure 8.4.4(c). This can be contrasted with the transition state for the bridge-top orientation in Figure 8.4.4(f), in which the carbon atoms lie between the atoms of the top metal layer, resulting in more favorable dispersion interactions.

The results for the sliding barriers are qualitatively similar to exfoliation energies, in that physisorption effects are negligible, while chemisorption can significantly perturb the interlayer interactions. While the substrate contributes additional dispersion interactions not present in free BLG, the added dispersion is relatively constant with respect to translation for physisorbed BLG and thus will have little effect on the sliding barrier. The variations between substrates are instead due to changes in the surface lattice constant, which stretches the BLG and consequently affects the base functional repulsion between the layers. However, this is an artifact of the highly-strained unit cells employed in the calculations (to ensure commensurate lattice constants) and will be mediated in real systems by the adoption of different rotational orientations by the graphene to minimize lattice strain. Thus, sliding of physisorbed BLG is effectively independent of the choice of substrate. However, for chemisorbed BLG, the effect of the substrate is much more significant and can lower the dispersion contribution to the barrier by as much as 40%. Moreover, the translational orientations of the chemisorbed BLG strongly affect the frictional behavior.

8.5 Summary

This chapter investigated the effects of substrates on BLG interlayer interactions, as quantified by exfoliation energies and sliding-energy barriers. The substrates studied were face-centered cubic metal (111) surfaces of Al, Cu, Ag, Au, Ni, Pd, and Pt; a graphite substrate and freestanding BLG were also considered as reference systems for comparison. Potential-energy surfaces for exfoliation and translation of the top graphene layer were calculated using the B86bPBE exchange-correlation functional and the exchange-hole dipole moment (XDM) dispersion correction.

In the first section, we showed how the exfoliation energies and sliding barriers differ between graphite and BLG. The addition of a graphite support increases the exfoliation energy by 0.5 kJ/mol C, due to the added dispersion interactions between the top graphene layer and the substrate. However, the sliding PES for the two systems are almost equivalent, as this additional dispersion is effectively constant with respect to translation of the upper graphene layer.

Physisorption of BLG on metal substrates results in similar exfoliation energies and sliding barriers to graphite. The BLG sliding barriers are sensitive to the surface lattice constant, with greater lattice strain resulting in higher friction. However, this is an artifact of enforcing commensurate lattices in our calculations, resulting in highly strained graphene in some cases. In practice, the graphene can adopt differing rotational orientations to minimise lattice strain.

Chemisorption of BLG occurs for differing rotational orientations on Ni-group metals and results in shorter interlayer distances and increased dispersion attraction between the top graphene layer and the metal surface. The closer proximity to the substrate increases the BLG exfoliation energy by $\sim$ 20% relative to graphite. Dispersion attraction to the substrate preferentially stabilizes the maximum-energy "AA" stacked orientation of BLG, reducing sliding barriers by up to $\sim$ 30%. Additionally, when BLG is chemisorbed on a metal substrate,

changes in the translational orientations of the BLG with respect to the surface can alter the sliding barriers by as much as $\sim 50\%$. These results demonstrate the need to explicitly include dispersion contributions from the substrate in computational studies of chemisorbed BLG.

Chapter 9: Atomic-scale Frictional Properties of Graphene Multilayers on a Cu(111) Substrate

The work presented in this chapter is currently unpublished.

9.1 Abstract

Few-layered graphene (FLG) has been shown to be a robust solid lubricant due to the weak van der Waals interactions between layers. Consequently, it has been reasonable to assume that the sliding interface for FLG on a metal substrate would lie between the graphene layers and not at the graphene-metal interface. However, few studies have investigated the energetics of the various sliding motifs. In this work, we present a study of monolayer, bilayer, and trilayer graphene sliding over a Cu (111) surface using density-functional theory (DFT) incorporating the exchange-hole dipole moment (XDM) dispersion model. Our results demonstrate that the preferred sliding interface is between the graphene and the metal surface for all graphene multilayers, even when subjected to compression. Pressure increases the sliding barrier, but the effect is reduced with additional graphene layers, as the compression can be ameliorated through smaller changes in all interlayer distances.

9.2 Introduction

Two-dimensional materials have been actively researched because of their unique electronic properties.[4,17,212] However, their characteristic weak interlayer interactions also make them ideal solid lubricants.[9,216] Graphene, like its bulk allotrope graphite, is an excellent lubricant. It can be applied directly to a surface through

deposition[292] or mixed into a solvent,[44,293,294] where graphene flakes adsorb to a substrate through turbulence. The strong carbon-carbon bonds provide a resilient surface during frictional contact that reduces wear at the sliding interface.[45]

Tribologists have studied the frictional modification of metal surfaces by graphene using atomic-force microscopy (AFM).[41,42,46,95,96,283,284] In these studies, an AFM tip is dragged across the surface to measure the coefficient of friction. Layer-dependent friction has been investigated systematically via AFM techniques. The addition of a single layer of graphene (SLG) greatly reduces the sliding friction relative to a bare metal surface. Additional layers of graphene further decrease the surface friction, until the friction coefficient converges to the same value as for bulk graphite. This typically occurs after the addition of four or five graphene layers.[41,42] The lubricity also depends on the degree of graphene corrugation. Corrugation is reduced when graphene interacts strongly with the substrate, which in turn reduces the surface roughness and the sliding friction.[42,46,96] However, AFM results do not translate to shear sliding of the graphene layers, which is more relevant to understanding its lubricating properties at the interface of two metal surfaces, termed metal junctures.

The lubrication properties of few-layered graphene (FLG) for shear sliding at metal junctures has been studied experimentally for many applications.[44,45,284,293–295] Generally, there is a dramatic reduction of surface wear at the sliding interface upon graphene deposition.[293,295,296] It is typically assumed that the shear-sliding interface for these systems is between the graphene sheets,[45] which is reasonable given that the weak van der Waals interlayer interaction is significantly less than the adsorption energy of graphene on transition-metal surfaces.[34,53,265,272,282] However, a strong static interaction with the metal surface does not necessarily reflect the sliding barrier, as it is defined as the difference between the highest- and lowest-energy conformations along the sliding path. The possibility that FLG sliding may preferentially occur across a substrate, instead of between graphene sheets, was verified by Kitt *et al.*[284] for an SiO_2 surface. However, graphene is

known to interact weakly with SiO_2, so this may not be the case for substrates like transition metals that interact more strongly with graphene.

Computational investigations of graphene on metal substrates have largely focused on the interlayer distances and SLG exfoliation energies.[36,37,39,50,53] Conversely, several molecular-dynamics simulations have investigated interlayer sliding of bilayer graphene (BLG)[46,297,298] for a variety of experimental designs, but did not consider metal substrates. This was also the case for previous DFT calculations on shear sliding of the middle layer in trilayer graphene (TLG).[299] Neglecting a substrate inherently limits a computational study of friction because it removes a possible sliding interface. We previously assessed how a metal substrate affects the interlayer interactions and sliding barriers of BLG.[300] However, we did not consider coherent sliding of BLG over the metal surface. Two our knowledge, a systematic study of the coherent sliding motifs of multi-layered graphene on a substrate has not been conducted.

This article investigates the various sliding motifs of SLG, BLG and TLG on the copper (111) surface. The first section compares the sliding barriers of SLG across copper and nickel surfaces, as it is established that graphene strongly chemisorbs to Ni, but physisorbs on Cu. The weaker interactions with the Cu surface cause the various translational orientations to be nearly energetically degenerate. This results in a lower sliding barrier for graphene over copper than over a graphite substrate. Consequently, for BLG and TLG on Cu, the graphene-metal sliding interface is consistently the most energetically favorable. The sliding barrier for this interface is also found to be independent of the number of graphene layers. Additionally, we compare the energetics of the various sliding motifs while constraining the distance between the top graphene layer and the surface to mimic the effect of an applied normal force. As for unconstrained sliding, the FLG systems prefer to slide uniformly across the copper substrate, but additional graphene layers are found to decrease the sliding barrier by ameliorating the effect of the applied compression.

Figure 9.3.1: The various systems considered in this work: (a) monolayer graphene, (b) bilayer graphene, and (c) trilayer graphene, all adsorbed on the Cu (111) surface. The possible sliding interfaces are shown in blue (first layer), green (second layer), and red (third layer). For each sliding motif, all layers in a given colored box are translated with respect to the surface.

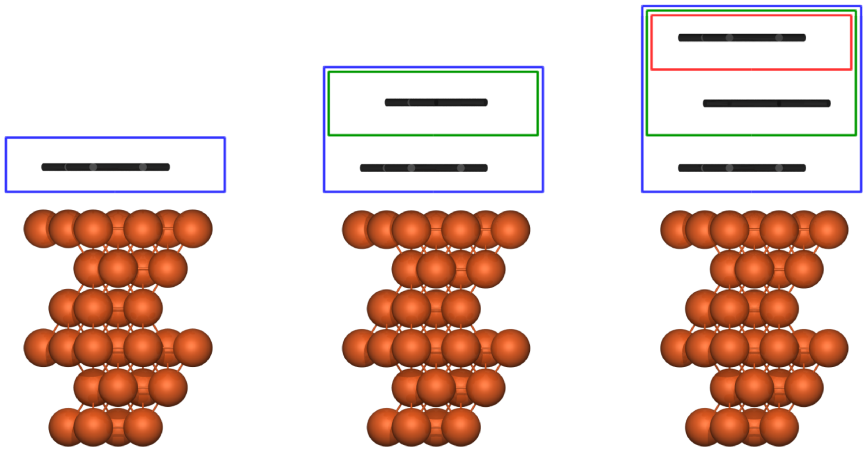

9.3 Computational Methods

In this work, we focus on the frictional properties of single-layer, bilayer, and trilayer graphene on a Cu (111) surface. For each N-layered system, there are N possible sliding interfaces (i.e. one for SLG, two for BLG, and three for TLG) either at the surface or between graphene layers. Potential energy surfaces (PES) were generated for the interlayer sliding of these three systems. Each of the possible sliding interfaces are shown in Figure 9.3.1. For comparison, additional calculations were performed for SLG sliding on the Ni (111) surface and over a graphite substrate. In all cases, we considered a (1×1) unit cell, which corresponds to a 0° orientation between the graphene and metal lattices. As in our previous work,[300] the sliding PESs were generated by sliding the graphene sheets across the long diagonal of the unit cell as this completely samples the sliding-interface PES due to the crystal's symmetry.

Each surface was modeled as a slab consisting of six atomic layers separated from its periodic images by a large vacuum region, with the total unit-cell length perpendicular to the surface set to be 70 Bohr for all systems. The metal lattice constants were chosen to correspond to minimum-energy values from our previous

work:[282] 2.461 Å for graphite, 2.482 Å for SLG on Ni, 2.521 Å for SLG on Cu, and 2.509 Å for BLG on Cu. The slight increase between the latter two values serves to reduce graphene lattice strain. The TLG calculations used the same lattice constant as obtained for BLG on Cu.

To generate the sliding PES, one, two, or three graphene layers were translated with respect to the surface, as shown in Figure 9.3.1. At each point along the PES, the graphene-metal and all graphene-graphene interlayer distances were systematically varied in 0.05 Å increments. The energy at each point was minimized by quadratic interpolation. Additionally, sliding PES with applied compression normal to the surface were also investigated. In these cases, the energies were minimized after constraining the total distance between the uppermost graphene layer and the surface.

All DFT calculations were carried out using periodic boundary conditions with the projector augmented wave (PAW)[114] formalism as implemented in Quantum ESPRESSO.[179] The same methodology was employed as in our previous publications on graphene-metal interactions.[272,282,300] Specifically, the B86bPBE exchange-correlation functional[126,180] was combined with the exchange-hole dipole moment (XDM) dispersion correction.[60,61,273] B86bPBE-XDM has been shown to be highly accurate for prediction of graphene-metal adsorption energies and interlayer distances.[282] PAW datasets were generated using LD1 version 4.3.2 using pslibrary 0.2.5 inputs. The datasets also included scalar relativistic effects and non-linear core corrections.[181] All datasets were checked to ensure that there was no PAW sphere overlap for each optimized geometry. All calculations used an $8 \times 8 \times 1$ Γ-centered $\mathbf{k}$-point grid, a plane-wave cutoff of 60 Ry, a density expansion cutoff of 800 Ry, and a cold smearing[108] parameter of 0.01 Ry. Ni calculations were carried out using an initial spin-polarization and checked for convergence to the correcet spin state.

Figure 9.4.1: Exfoliation (left) and sliding (right) potential energy surfaces for a graphene monolayer on either Ni or Cu (111) substrates. The PES for sliding of a single graphene layer on a graphite substrate is included for comparison.

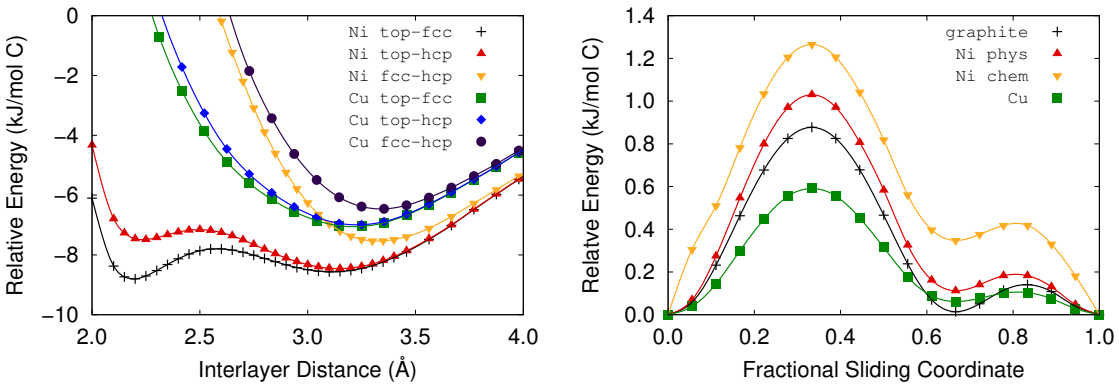

9.4 Results and Discussion

9.4.1 Comparison of Monolayer Graphene Sliding on Ni and Cu Substrates

In this section we contrast the potential-energy surfaces for exfoliation and sliding of SLG over Ni and Cu substrates. It is well established that graphene chemisorbs on Ni when the carbons are centered over a surface metal atom, and physisorbs when the carbons are centered over surface void sites.[87,228,272] There is significant charge transfer between the nickel metal and graphene in the chemisorbed orientations, and negligible charge transfer in the physisorbed orientations. In contrast, graphene physisorbs on Cu regardless of the translational orientation.[89,266,275,279,280,282]

The computed exfoliation PES for graphene on Ni and Cu are shown in Figure 9.4.1(a) for the three translational orientations depicted in Figure 9.4.2. For Ni, the top-fcc and top-hcp PES display both chemisorption and physisorption minima, while fcc-hcp permits only physisorption as all the graphene carbon atoms lie directly over void sites on the surface. Experimentally, the chemisorption minima is favoured and is characterised by an interlayer distance of 2.04–2.18 Å[87,249] and adsorption energy of 7.2–11.2 kJ/mol C.[53,244] These values are reproduced closely by our DFT-XDM calculations, which give an interlayer distance of 2.20 Å and

Figure 9.4.2: Geometries of three extrema on the sliding PES for graphene on the Cu(111) substrate. These structures correspond to fractional sliding coordinates of zero (top-fcc), one-third (fcc-hcp) and two-thirds (top-hcp). The graphene is shown in the "tube" representation, while the underlying substrate is represented by the "ball" motif and coloured according to the depth from the surface.

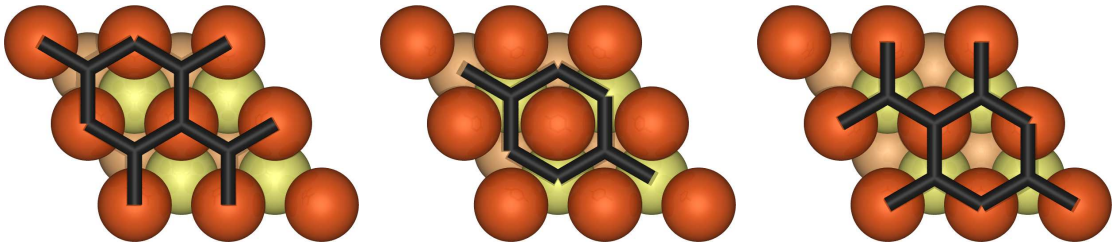

(a) top-fcc, global minimum (b) fcc-hcp, maximum (c) top-hcp, local minimum

adsorption energy of 8.80 kJ/mol C, using a fixed lattice constant for the isolated slab calculations. In contrast to Ni, graphene physisorbs to Cu, having a much longer interlayer distance of 3.21 Å and weaker adsorption energy of 7.06 kJ/mol C, as calculated with DFT-XDM using a fixed lattice constant. These differences between chemisorption and physisorption binding result in significantly different frictional behavior at the graphene-metal interface.

Figure 9.4.1(b) shows the PES for interlayer sliding across the long diagonal of the unit cell for these same systems. The top-fcc orientation corresponds to the global minimum in both cases, while top-hcp corresponds to the local minimum two-thirds of the way along the fractional sliding coordinate. The fcc-hcp orientation is the global maximum, one-third of the way along the sliding coordinate. The sliding barrier corresponds to the energy difference between the minimum-energy top-fcc and maximum-energy fcc-hcp orientations, which is 1.27 kJ/mol C for Ni and 0.59 kJ/mol C for Cu. The near degeneracy of the various translational orientations for graphene on copper results in a significantly lower sliding energy barrier.

For Ni, the strong interaction between the graphene and the surface results in a higher sliding barrier than that of graphite. The "Ni phys" curve in Figure 9.4.1(b) is for sliding between the theoretical physisorbed minima. This PES is a significant underestimation of the true graphene-Ni sliding barrier as graphene preferentially

chemisorbs for the top-fcc orientation. Adding the energy difference between the chemisorbed and physisorbed minima shifts the PES higher in energy (by 0.24 kJ/mol C) to give the "Ni chem" curve in Figure 9.4.1(b). However, molecular-dynamics simulations are required to capture the true sliding behavior here due to the complicated nature of the PES. Nonetheless, the sliding barrier for graphene on Ni is higher than that of graphite, (by $\sim$ 0.4 kJ/mol per C), and this is consistent with literature involving graphene multilayers sandwiched between two Ni(111) surfaces.[219] This chapter found that the graphene sheets strongly adhere to the Ni surfaces and that the sliding interface lies between graphene layers, in agreement with the results of Figure 9.4.1. Indeed in most cases where graphene acts as a coating on metal surfaces it is thought to strongly adhere to the surface and that the frictional interface will be between graphene layers.[44,45,294,295]

For Cu, evaluation of the sliding PES is straightforward as only a single physisorption minimum is present for all translational orientations, as shown in Figure 9.4.1(a). The near degeneracy of these various translational orientations results in a very low sliding barrier, even lower than that of graphite (by $\sim$ 0.3 kJ/mol C), as seen in Figure 9.4.1(b). This result implies the possibility that a graphene-metal frictional interface may be preferable to graphene-graphene shear for FLG on copper.

9.4.2 Few-Layer Graphene Sliding on Cu

The sliding PES for the various monolayer, bilayer, and trilayer sliding motifs of graphene on Cu(111) are presented in Figure 9.4.3. These PES are expressed relative to the lowest energy orientation for each system and, due to the increasing numbers of graphene layers, are expressed per unit cell (or equivalently unit area) rather than per carbon atom. We should note that because the energies are expressed relative to the most-stable configuration, these plots do not reflect the differing adsorption energies of the multiple layers to the metal surface. Additionally, they do not represent the energy required to slide a tip over the surface, but

Figure 9.4.3: Potential energy surfaces for various sliding motifs of monolayer, bilayer, and trilayer graphene on Cu (111). The PES for sliding of a single graphene layer on a graphite surface is included for comparison.

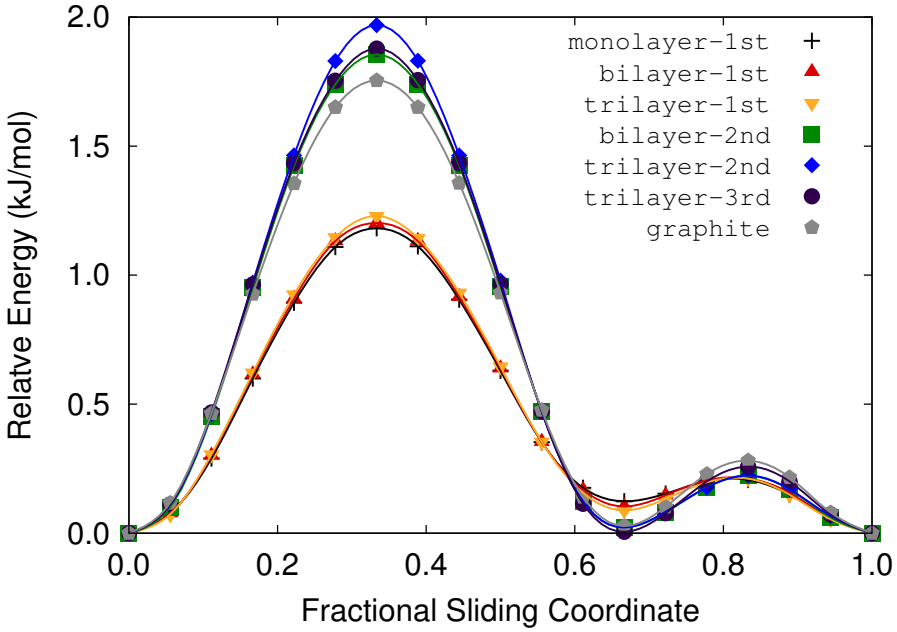

rather the energy difference required to slide 1-3 graphene layers, as depicted in Figure 9.3.1.

The results in Figure 9.4.3 show that the favored sliding interface is between the graphene and the copper surface. The sliding energy barriers for the graphene-graphene interfaces are all higher than for the graphene-copper interface and this difference relates to the graphene stacking orientations during sliding. For graphene-copper sliding, the graphene layers remain in their most stable orientation, AB (bilayer) and ABA (trilayer), as they are translated in unison with respect to the copper surface. In contrast, a graphene-graphene sliding interface results in high-energy AA (bilayer-second), AAB (trilayer-second), and ABB (trilayer-third) stacking configurations. The increased non-bonded repulsion in these AA (or BB) stacks results in a greater energy penalty than for translation from the top-fcc to the hcp-fcc orientation of the bottom graphene layer on the substrate.

Figure 9.4.3 also shows that the graphene-copper sliding PES is independent of the number of graphene layers. As argued in our previous paper detailing substrate affects on BLG,[300] this is because the second and third graphene layers

are sufficiently distant from the substrate that the dispersion attraction between them has a negligible contribution to the PES. The bilayer-second and trilayer-third motifs result in a slightly higher barrier than for sliding of the top graphene layer over a graphite substrate, which is due to the differences in lattice constants. We have shown previously that the BLG sliding barrier increases with the lattice constant, as this destabilizes the maximum-energy AA orientation relative to the minimum-energy AB orientation.[300] Lastly, the trilayer-second motif has a slightly higher barrier than for sliding of the top layer alone due to changes in the dispersion interactions between the first and third graphene layers along the PES.

The current results may be compared with the experimental findings of Kitt *et al.*[284] for FLG on SiO_2, as graphene also physisorbs on this substrate. In that work, a graphene-substrate sliding interface was observed for TLG, in agreement with our prediction for Cu. However, a graphene-graphene interface was seen for BLG on SiO_2. They reasoned that the difference was because the addition of the third graphene layer reduced the FLG-metal sliding barrier enough to make the graphene-metal interface more energetically favorable[284] and this was confirmed by molecular dynamic simulations. In the present study, the barrier for graphene-Cu sliding is consistently lower than for graphene-graphite sliding and is therefore the preferred interface for all graphene multilayers.

9.4.3 Variation of Interlayer Distances

We next consider how the graphene-metal and graphene-graphene interlayer distances change along the PES for each sliding motif. The changes in interlayer distances at the graphene-copper interfaces in Figure 9.4.4(a) mirror the shape of the PES, with the shortest interlayer distances occurring for the most strongly bound top-fcc orientation and the longest distances occurring for the most weakly bound fcc-hcp orientation.

Similarly, for a graphene-graphene interface, the changes in interlayer distances in Figure 9.4.4(b,c) again mirror the shape of the PES, with the AA stacked orien-

Figure 9.4.4: Changes in interlayer distances along the PES for each sliding motif. Results are shown for the distance between the copper surface and first graphene layer (left), the first and second graphene layers (middle), and the second and third graphene layers (right). The key is identical to Figure 9.4.3.

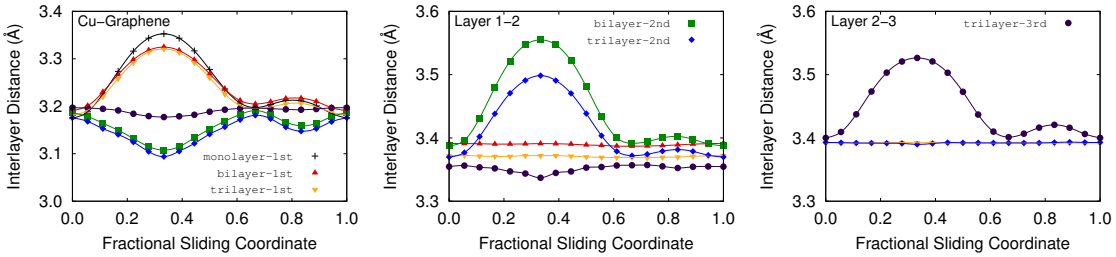

Figure 9.4.5: Exfoliation PES for graphene on either a graphite or copper surface. Curves are shown for both the minimum-energy (AB-stacked or top-fcc) and maximum-energy (AA-stacked or fcc-hcp) orientations. All distances and energies are expressed relative to the respective potential-energy minima.

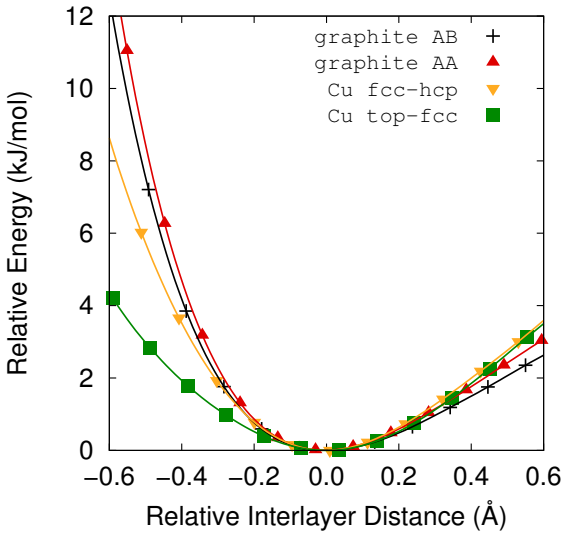

tations having much larger interlayer separations than AB stacking. Conversely, distances between AB stacked graphene layers that do not form the sliding interface are effectively constant along the PES. The distance between the first and second graphene layers is shorter by 0.02 Å in trilayer graphene than in bilayer graphene due to added dispersion interactions between the first and third layer, which result in greater interlayer adhesion. This is analogous to the shorter interlayer distances in bulk graphite (3.35 Å) relative to the upper two layers on a graphite surface (3.37 Å) and bilayer graphene (3.39 Å).[300]

For a graphene-graphene sliding interface, the first graphene layer is always in the top-fcc orientation with respect to the surface for the entirety of the PES.

Despite this, Figure 9.4.4(a) shows that the graphene-metal distances also vary for these sliding motifs. To understand these findings, we need to consider the relative compressibility of the various sliding interfaces, as shown in Figure 9.4.5. This figure presents exfoliation PES for two orientations of graphene on either a copper or graphite surface, expressed relative to the minimum of each potential to allow comparison of the steepness of the repulsive walls. The results indicate that the graphene-copper interface, particularly for the top-fcc arrangement, is more easily compressible than the graphene-graphene interface.

The sliding PES for the first and second graphene layers are AA stacked (or AAB stacked) at the maximum-energy points for the bilayer-second and trilayer-second motifs. Figure 9.4.5 showed that the top-fcc copper-graphene interface is highly compressible and experiences less repulsion than the AA-stacked graphene-graphene interface. Thus, to minimize repulsion between the AA stacked layers, the lower layer moves down towards the surface. This results in a contraction of the graphene-metal distance at the maxima, one-third of the way along the sliding coordinate, as seen in Figure 9.4.4(a). This contraction is less significant for the trilayer-third motif, in which the graphene layers are ABB stacked at the maximum-energy configuration, due the additional attraction between the consistently AB stacked first and second graphene layers.

9.4.4 Sliding Under Applied Pressure

The constrained sliding PES for monolayer, bilayer, and trilayer graphene on copper are illustrated in Figure 9.4.6. These PES display the relative energetics of the sliding motifs under an applied normal force, by imposing a constrained upper bound to the distance between the top graphene layer and the surface. As for the optimized sliding PES, the energies are shown relative to the minimum-energy configuration for each system. All of the sliding motifs behave as expected, with the sliding barrier increasing with applied pressure. As the constrained distance is shortened, the graphene sheets approach both the surface and each other more

Figure 9.4.6: PES for the various sliding motifs, with the distance between the top graphene layer and the metal (given in Å) constrained, to mimic an applied normal force.

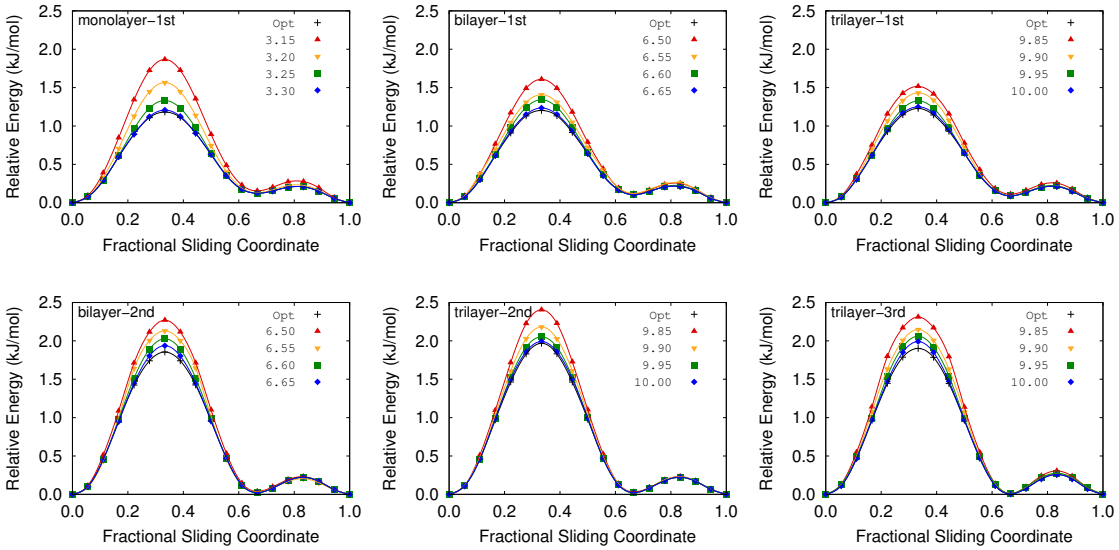

closely, such that the sliding barrier increases due to the increased non-bonded repulsion.

The relative increases in the barrier for each system and sliding interface can be explained by the results in Figure 9.4.5. With the exception of the monolayer-first motif, the constrained PES predict that the sliding barrier increases more rapidly with pressure for the graphene-graphene than for the graphene-metal interfaces. This is because of the slightly steeper repulsive wall for compression of AA-stacked graphene sheets compared to fcc-hcp graphene-copper.

Finally, for the graphene-metal interface, identical compression of the total distance between the surface and top graphene sheet results in smaller changes in the sliding barriers, going from the monolayer to the bilayer and trilayer. This is because it is more favorable to apply a fraction of the total compression to each of the interlayer distances. As such, for FLG on copper, the system can be significantly compressed by an applied force normal to the sliding interface, while still maintaining a low sliding barrier, and hence low friction.

9.5 Summary

This chapter investigated the sliding energy barriers of all possible sliding motifs for SLG, BLG, and TLG on Cu (111) under equilibrium and constrained conditions using dispersion-corrected DFT. In contrast to what occurs for Ni (111) surfaces,[219] but in agreement with results[284] for FLG on SiO_2, the sliding interface between the lowermost graphene sheet and metal surface is energetically preferred over any of the graphene-graphene sliding interfaces. This is because the various translational orientations of graphene on the Cu (111) surface are nearly degenerate.

Constraining the total distance between the surface and uppermost graphene layer was considered to predict the evolution of the sliding barriers under applied pressure. The top-fcc graphene-copper interface was found to be more readily compressible than fcc-hcp, or for either AB- or AA-stacked BLG. While the equilibrium graphene-copper sliding barrier is independent of the number of graphene layers, the increases in sliding barrier under applied load were found to be smaller when additional graphene sheets are present. This is because the total compression can be divided between the various interlayer distances, resulting in reduced repulsion. Consequently, FLG-copper interfaces should maintain low friction under applied pressure. These theoretical predictions could potentially be tested by experiments performed for junctions consisting of FLG confined between two copper surfaces. The results presented here complement experimental observations by providing new mechanistic insights into the atomic-scale frictional behavior of graphene on metal surfaces and suggest that determination of the preferred sliding interface is more nuanced than previously assumed.

Chapter 10: Conclusion

This thesis modeled various motifs of graphene on metal surfaces using the exchange-hole dipole moment (XDM) dispersion correction. XDM was shown to include the proper physics to accurately model physisorption energies of aromatic molecules on surfaces in Chapter 5. This demonstration was then extended to the adsorption of graphene on the Ni (111) surface in Chapter 6 and the (111) surface for six additional transition metals in Chapter 7. The results of this study prompted us to investigate substrate effects on bilayer graphene in Chapter 8. The results showed that metal substrates affect graphene interlayer interactions only when it chemisorbs on the surface. Finally, Chapter 9 presented an extensive investigation of graphene sliding motifs on the Cu (111) surface. It showed that multilayered graphene prefers to slide uniformly over a metal surface, rather than having the sliding interface located between the graphene layers.

At the start of this thesis, it was believed that pairwise density-functional dispersion corrections could not properly model van der Waals interactions between a metal surface and an adsorbed molecule or material.[47,124,148,171,172] This was because the pairwise methods implemented at the time used fixed semi-empirical dispersion coefficients that overestimated the dispersion interactions involving surface or bulk metal atoms. It was shown in Chapter 5 that the adsorption energies determined by XDM are accurate when compared to experimental data and that accurate surface interactions can be modeled by a variable-coefficient pairwise dispersion model such as XDM.[64]

The ability of XDM to properly describe dispersion interactions at metal surfaces was further benchmarked for graphene adsorption on the Ni (111) surface in

Chapter 6. This particular case had been difficult for DFT[35,37,53,227,228] because electrostatic base-functional contributions and the dispersion contribution must be balanced. Our results[272] were able to reproduce potential energy surfaces in agreement with those reported by the RPA method and with experimental adsorption energies. It was also shown that the potential energy surface of graphene on Ni (111) is sensitive to the surface lattice constant, indicating that thermal effects play an important role in graphene-nickel interactions. Analysis of the XDM contribution also showed that the dispersion coefficients change with graphene-metal distances and this is primarily because of variations in the exchange-hole multipole moments, not in the atomic polarizabilities that are obtained from atomic volumes. This result illustrated why DFT dispersion corrections that are based on atomic volume changes[58] do not properly model surface dispersion interactions.

Graphene adsorption was subsequently modeled for several additional (111) transition metal surfaces in Chapter 7. Previous computational investigations only modeled graphene-metal orientations that reduced carbon-carbon bond strain in the periodic cell.[36,37] However, experimental literature had indicated that graphene-metal interactions vary with orientation on some metal surfaces, forming a wide range of Moiré patterns.[33,88,261–263] We compared the energetics for the 0° and 30° orientations of graphene on the metal surfaces. Our results[282] showed that there is a significant energetic preference for graphene to have an aligned orientation with respect to the substrate-surface lattice vector because it maximizes both the electrostatic and dispersion interactions between the substrate and the graphene layer. These results agree with LEED observations of graphene on several metal surfaces.

The effect of substrates on interlayer graphene interactions were investigated with DFT in Chapter 8. The substrates chosen were the same metal surfaces asin our graphene-metal study. Adsorption energies of physisorbed bilayer-graphene–metal systems showed that the addition of a substrate gives similar bilayer-graphene exfoliation energies and interlayer distances as for a graphite substrate. However,

chemisorbed bilayer-graphene–metal systems were shown to significantly decrease interlayer distances and increase exfoliation energies. This was primarily because of the closer proximity of the metal to the second graphene layer that results in greater dispersion stabilization.

The results of Chapter 7 and Chapter 8 showed that graphene has similar adsorption energies on copper as on graphite. This prompted us to investigate various sliding motifs of monolayer, bilayer and trilayer graphene on the Cu (111) surface. The preferred sliding interface for few-layered graphene on copper was shown to be between the graphene and metal surface. In addition, this sliding interface remains preferred when the sliding is constrained, due to the greater repulsive wall for adsorption of two graphene layers than for the graphene metal contact. These results are in agreement with experimental observations of various graphene tribological experiments.[284,294]

There remain several questions to be further investigated. It was shown in Chapter 6 that the dispersion coefficients rapidly change for short graphene-metal distances.[272] This has resulted in an issue with the current XDM force implementation, which assumes constant dispersion coefficients with respect to atomic distances.[61] This issue was side-stepped in the studies presented here by optimizing interlayer distances through quadratic interpolation of the single-point energies. However, this method is insufficient for molecules or materials where the forces are highly anisotropic. Therefore, a method for calculating the forces using varying dispersion coefficients is required. However, doing so requires analytical derivatives of the exchange-hole multipole moment with respect to atomic distances, which have not yet been formulated or implemented.

One particular experimental observation that was not reproduced in our graphene-metal studies is the change in friction with additional graphene layers established by AFM studies.[41,42,96] This has been widely attributed to the corrugation of graphene on real metal surfaces, which is not replicated in our studies.[41,42] However, findings from Chapter 8 imply that an additional contribution could be dis-

persion interactions between an AFM tip and the metal substrate, which would decrease with additional graphene layers. This hypothesis could easily be tested by building upon the calculations carried out in Chapter 9. Instead of sliding various numbers of graphene layers over the metal surface, a metal slab would be slid across the graphene-metal surface, while varying the number of graphene layers. The dispersion interactions between the two metal slabs would be analyzed with the same approach outlined in Chapter 8. The exfoliation and sliding PESs will match the graphene-metal results only in the non-interacting limit.

Additionally, the role of thermal effects on the adsorption processes presented in this thesis could be investigated. All adsorption energies presented here are the electronic molecule-surface or graphene-surface interaction energies, as determined by DFT-XDM, and do not include zero-point or thermal vibrational energy contributions. Previous theoretical investigations of physisorbed molecules, such as those presented in Chapter 5, found that the vibrational energy contributions to be negligible (between 0.1 and 1.5 kJ/mol).[301] However, experiments have shown that thermal vibrational energy contributions play a significant role in surface adsorption of graphene, particularly with respect to its frictional properties.[302–304] Additionally, molecular dynamics simulations have shown that the sliding energy barrier for multilayer graphene decreases with increasing temperature.[305–307] It is therefore expected that including thermal effects would reduce the adsorption energy for graphene on metals, but to what extent is unknown.

Thermal effects play a greater role in modeling graphene frictional properties at larger length scales than the unit-cells of the systems modeled in this thesis. For instance, higher temperatures increase graphene rippling, which increases the sliding energy barrier.[302,308] Additionally, multi-layered graphene has a low rotational energy barrier, such that the layers can slide incommensurately.[303–307] Modeling these effects is beyond the scope of the calculations carried out in this thesis because of the very large unit-cells required to resolve graphene rotational domains and to model graphene rippling. However, these effects can, and have

been, quantified using classical molecular dynamics simulations.[305–307] The results presented for bilayer graphene physisorption in Chapter 8 support that molecular dynamics modeling of free-standing bilayer graphene, without explicitly including a substrate, is adequate for studying thermal effects on interlayer sliding mechanisms.

Though this thesis concentrated on graphene-metal interactions, the methods described here could be extended to other 2D materials, such as TMDs. As stated earlier, TMDs have a wide variety of applications, ranging from electronic sensors to catalysts.[8,12,13] TMDs have been shown to be very promising catalysts for the hydrogen evolution reaction (HER).[24] The structure's catalytic efficiency depends on the defect density and crystal stacking, which can be difficult to control in commercial manufacturing. A TMD's catalytic activity increases if coupled to a suitable second TMD to form a van der Waals heterostructure.[5,24,40,309,310] Charge transfer from a second suitable TMD creates a metallic-like surface state that enhances hydrogen affinity, making stacking orientation irrelevant and defect density less important. This makes the van der Waals heterostructure a more efficient HER catalyst than a single TMD layer.[5,24,40,309,310]

A promising TMD heterostructure is MoS_2 stacked on WS_2.[40] The alignment of the electronic bands of MoS_2 and WS_2 form a type II heterojunction with efficient charge transfer.[311] The experimental success of MoS_2/WS_2 make it a benchmark system to which hypothetical TMD heterostructures could be compared to screen for promising HER catalysts. Hydrogen affinities for each heterostructure can be evaluated by calculating the structural stability and hydrogen affinity for each heterostructure and comparing them to MoS_2/WS_2.

The NIST JARVIS-DFT 2D materials database[312] contains 60 examples of TMDs.[312] Evaluating all possible TMD heterostructures is beyond the scope of what can be efficiently fabricated and experimentally evaluated. Computational methods can efficiently calculate hydrogen affinities and stabilities for the thousands of possible structures for HER catalysis. Through methods proposed in this

thesis, it would be possible to reduce the thousands of possible TMD heterostructures to a few promising candidates for HER catalysis.

Appendix A: Supporting Information for Chapter 5

Table A.0.1: Calculated molecule-surface distances, in Å, measured as the distance from the heteroatom (or carbon in the case of benzene) to the surface. The angles between the surface and the molecular aromatic moiety, in degrees, are also indicated.

Molecule	Distances			Angles		
	Cu	Ag	Au	Cu	Ag	Au
Benzene	2.71	3.03	3.15	0.9	4.3	3.2
Furan	2.99	3.27	3.33	5.2	6.6	6.8
Furan perp.	3.06	3.16	3.28	58.4	68.3	68.0
Thiophene	2.99	3.04	2.95	2.2	2.2	4.6
Thiophene perp.	2.38	2.77	3.23	82.0	57.5	85.5
Thiophenol	2.43	2.81	2.75	5.1	3.8	6.6
Thiophenol perp.	2.78	2.97	3.02	79.4	77.9	77.1
Pyridine	2.17	2.68	3.04	24.5	13.1	8.6
Pyridine Perp.	2.08	2.40	2.38	82.1	77.3	65.9
1,4-Benzenediamine (cis)	2.94	3.16	3.26	1.0	1.7	0.1
1,4-Benzenediamine (trans)	2.22	2.52	2.52	8.0	6.8	8.4
Guanine	2.26	2.54	2.65	16.0	13.4	11.8
Cytosine	2.15	2.51	2.64	21.3	17.1	14.2
Adenine	3.02	3.09	3.18	0.8	2.0	1.4
Thymine	2.82	2.93	3.21	7.3	6.9	4.0

Table A.0.2: Comparison of calculated cubic lattice parameters for the three metals, in Å, with experimental results from R. Wyckoff, *Crystal structures* (Interscience publishers, New York, 1963).

	Calc	Exp.
Cu	3.573	3.615
Ag	4.080	4.086
Au	4.145	4.078

Table A.0.3: Convergence of the calculated adsorption energy of 1,4-benzenediamine (in the trans orientation) on the copper surface, with respect to changes in plane-wave cut-off (E_{cut}) and **k**-point grid. All results are for the 4-layer surface. For comparison, the adsorption energy on a 5-layer surface with a 4×4×1 **k**-point grid and a 60 Ry cut-off is 1.2579 eV/molecule.

E_{cut} (Ry)	**k**-points	E_{ads} (eV/molec)
50	4×4×1	1.2422
60	4×4×1	1.2429
70	4×4×1	1.2428
80	4×4×1	1.2420
60	3×3×1	1.2935
60	4×4×1	1.2429
60	5×5×1	1.2385
60	6×6×1	1.2401

Table A.0.4: Comparison of adsorption energies, in eV/molecule, for the cases where the isolated-molecule calculations were performed using the same cell as in the physisorbed complexes or in a supercell surrounded in all directions by a large vacuum ("Vac.").

Molecule	Cu	Vac.	Ag	Vac.	Au	Vac.
Benzene	0.59	0.60	0.68	0.68	0.64	0.64
Furan	0.53	0.53	0.52	0.52	0.51	0.51
Furan perp	0.24	0.24	0.25	0.25	0.22	0.22
Thiophene	0.66	0.64	0.67	0.64	0.62	0.60
Thiophene perp.	0.40	0.38	0.40	0.37	0.25	0.23
Thiophenol	1.00	1.00	0.90	0.90	0.91	0.91
Thiophenol perp.	0.35	0.35	0.36	0.36	0.33	0.33
Pyridine	0.69	0.68	0.58	0.56	0.60	0.58
Pyridine perp.	0.86	0.86	0.66	0.66	0.64	0.64
1,4-Benzenediamine (cis)	1.17	1.14	1.04	1.03	1.10	1.09
1,4-Benzenediamine (trans)	1.24	1.24	1.09	1.09	1.12	1.12
Guanine	1.07	1.17	1.03	1.09	0.94	0.99
Cytosine	0.96	1.03	0.90	0.94	0.77	0.81
Adenine	0.83	0.86	0.86	0.86	0.81	0.82
Thymine	0.67	0.72	0.69	0.72	0.67	0.70

Figure A.0.1: Nucleobase clusters used to estimate the intermolecular hydrogen-bonding energies

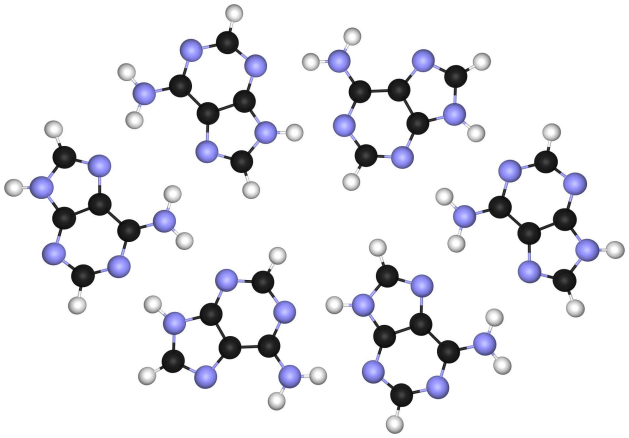

(a) adenine

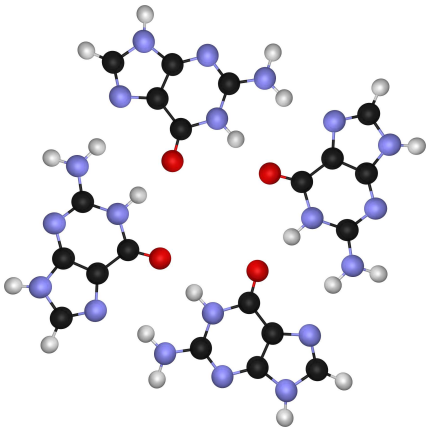

(b) guanine

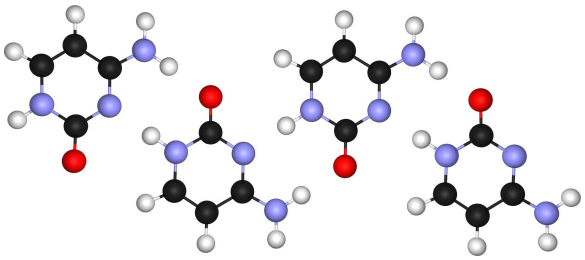

(c) cytosine

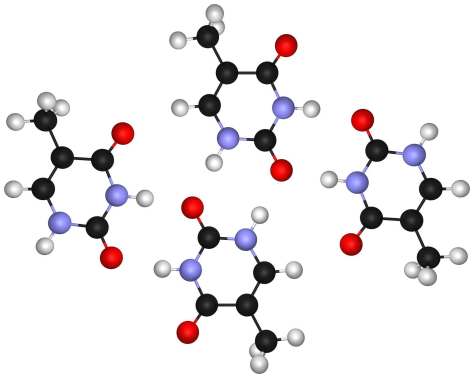

(d) thymine

Appendix B: Supporting Information for Chapter 6

A drawback of using dispersion coefficients that depend on the electron density and its derivatives is that the evaluation of the internuclear forces becomes more complex. In the Quantum ESPRESSO implementation of XDM,[61] it was assumed that the dispersion forces are dominated by the changes in the internuclear distances and the contribution from changes in the dispersion coefficients is negligible. While this assumption has proved valid for all previous applications of XDM, it was found to break down in the present case, due to the strong dependence of the dispersion coefficients on the graphene-nickel interlayer separation, as shown in Figure B.0.1. The resulting mismatch between the XDM dispersion forces and energies meant that we were not able to obtain reliable results from geometry optimizations on the graphene-nickel system. Rather, such optimizations resulted in underestimation of the interlayer distances and adsorption energies when compared to the results of the full PES scans. This problem means that full geometry optimization of graphene-metal interfaces must include derivatives of the dispersion coefficients in evaluation of the dispersion forces. This issue should be addressed in a future implementation of XDM.

Figure B.0.1: Effects of the XDM dispersion correction on the graphene-nickel PES. The total energies are decomposed into the base DFT (left) and XDM dispersion (middle) contributions. The values of the Ni-C C_6 dispersion coefficients are shown on the right. The upper row plots PES for all six orientations using the experimental nickel lattice constant (2.49 Å), while the lower row plots PES for the top-fcc orientation for five different lattice constants.

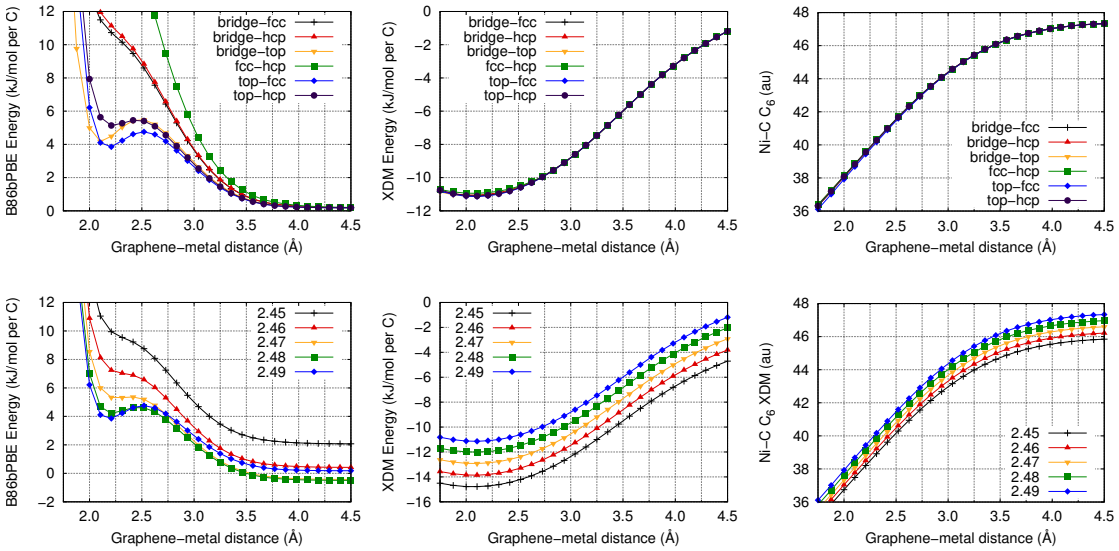

Figure B.0.2: Exchange-hole dipole moment integrals and atomic volumes for carbon and nickel as a function of interlayer distance using the B86bPBE base functional. The flat lines in the nickel plots correspond to the atoms within the interior of the slab, while the curves correspond to the surface atoms.

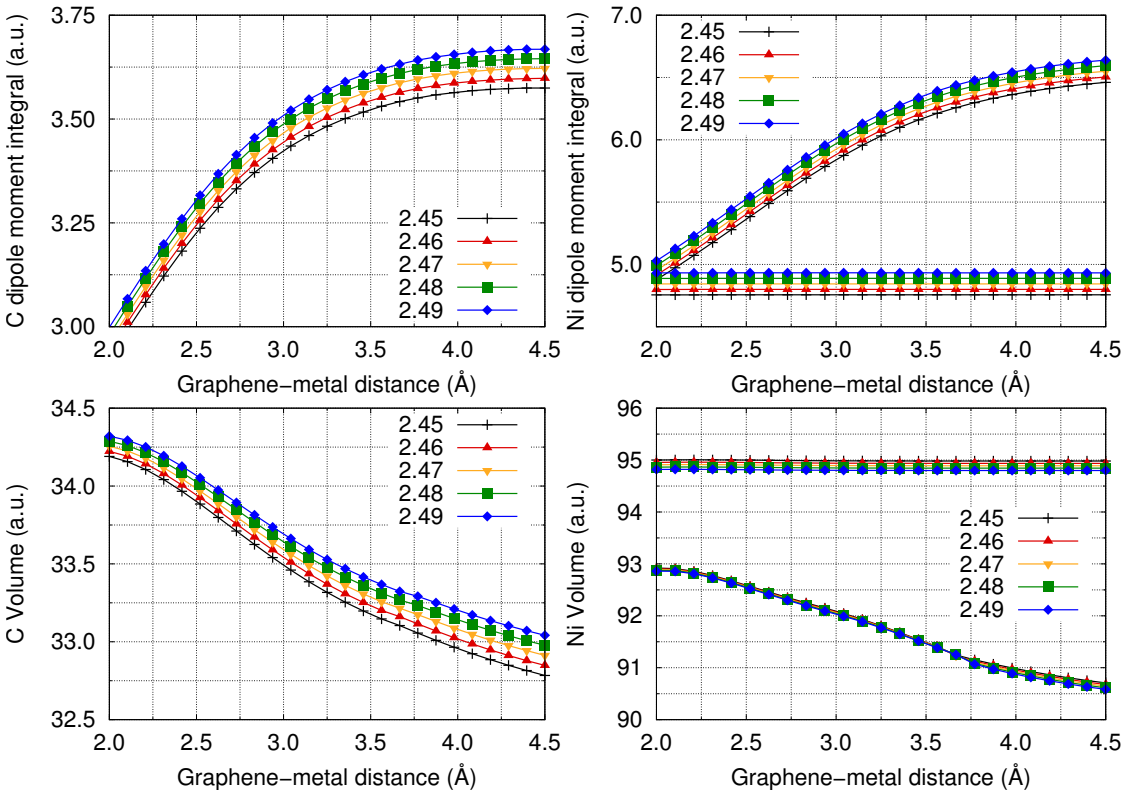

Figure B.0.3: B86bPBE-XDM potential energy surfaces for the six graphene-nickel orientations with lattice constants ranging from 2.45 Å to 2.49 Å

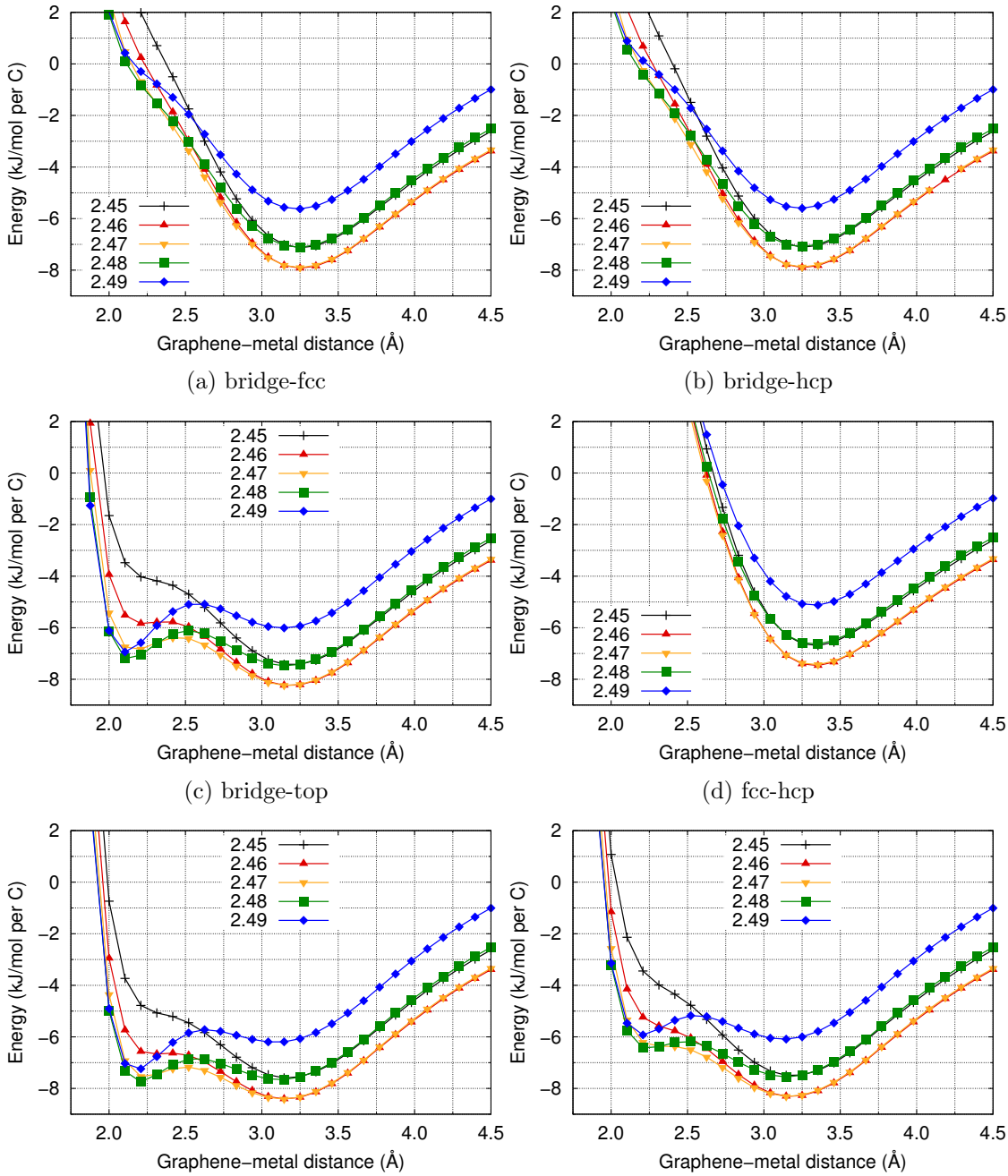

(a) bridge-fcc

(b) bridge-hcp

(c) bridge-top

(d) fcc-hcp

(e) top-fcc

(f) top-hcp

Figure B.0.4: PBE-XDM potential energy surfaces for the six graphene-nickel orientations with lattice constants ranging from 2.45 Å to 2.49 Å

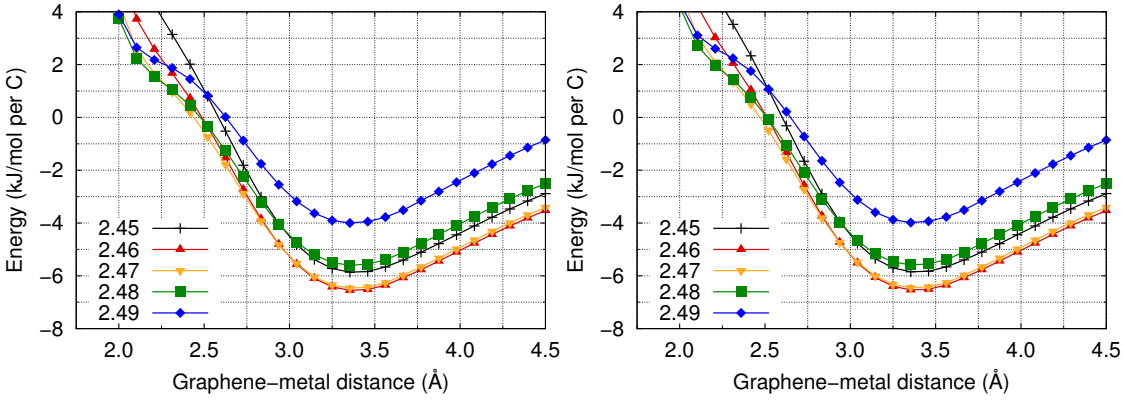

(a) bridge-fcc

(b) bridge-hcp

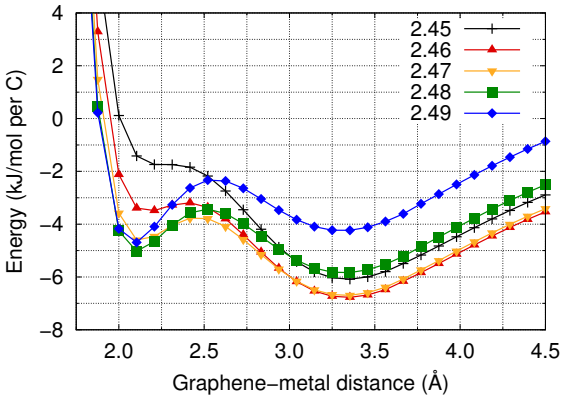

(c) bridge-top

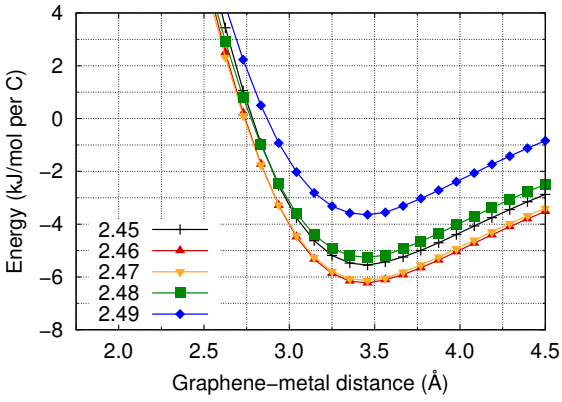

(d) fcc-hcp

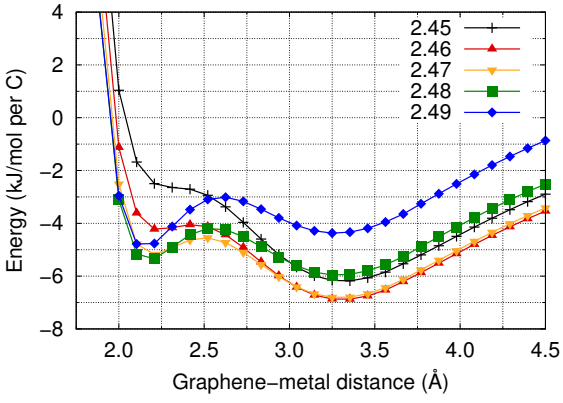

(e) top-fcc

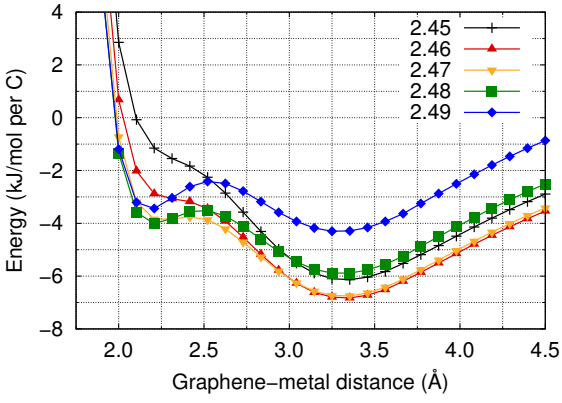

(f) top-hcp

Figure B.0.5: LDA potential energy surfaces for the six graphene-nickel orientations with lattice constants ranging from 2.45 Å to 2.49 Å

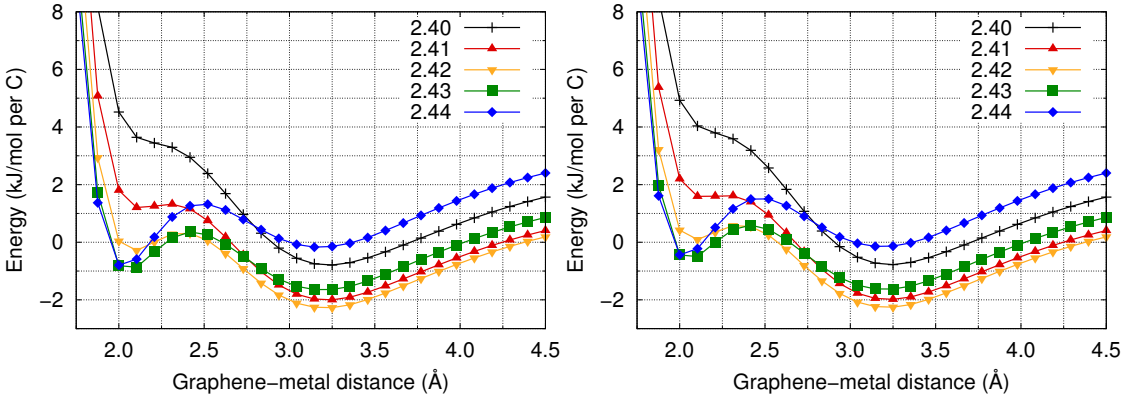

(a) bridge-fcc

(b) bridge-hcp

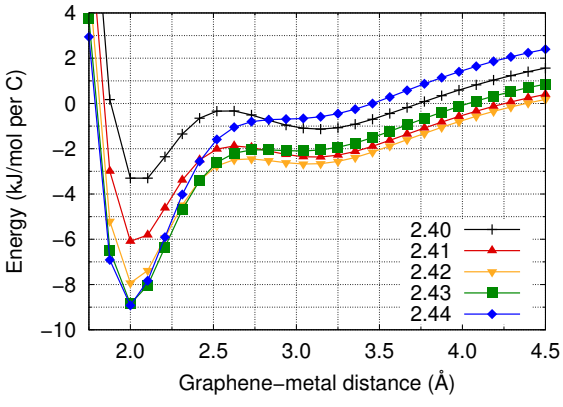

(c) bridge-top

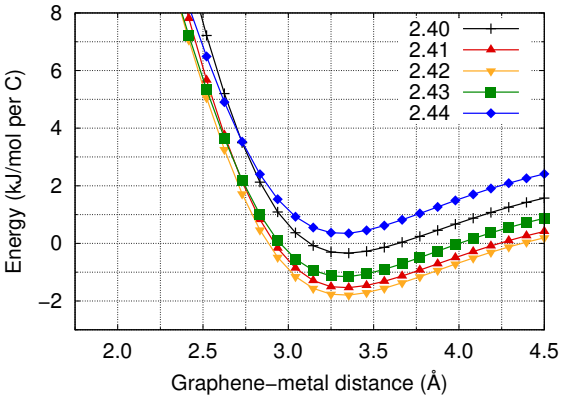

(d) fcc-hcp

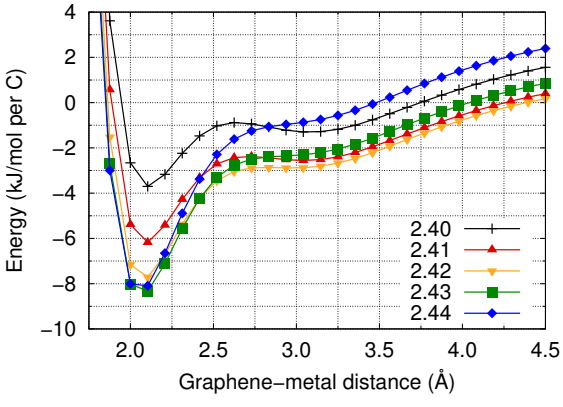

(e) top-fcc

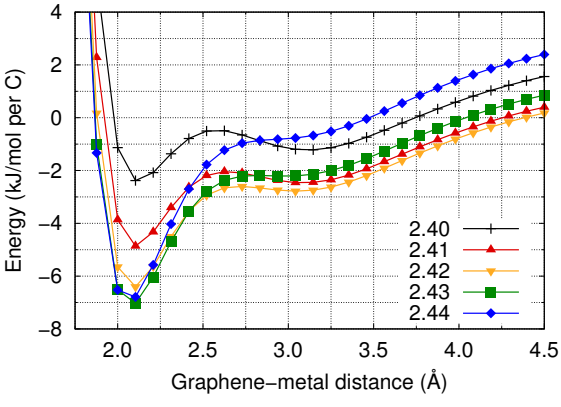

(f) top-hcp

Table B.0.1: Calculated interlayer distances (Å) and adsorption energies (kJ/mol per C) for both chemisorbed (C) and physisorbed (P) configurations of graphene on nickel (111) using the LDA, PBE-XDM and B86bPBE-XDM functionals. Two sets of results are given: the distances and energies at the minimum-energy surface lattice constant, and at the experimental nickel lattice constant (2.49 Å). The latter are comparable to the reported RPA results in the literature.[50,231] The experimental values are also given.

		bridge-fcc		bridge-hcp		bridge-top		fcc-hcp		top-fcc		top-hcp	
Method		d	E_{ads}	d	E_{ads}	d	E_{ads}	d	E_{ads}	d	E_{ads}	d	E_{ads}
Minimum-energy structures													
LDA	C	2.05	1.13	2.05	0.76	2.01	9.03	3.33	1.82	2.07	8.45	2.08	7.09
	P	3.21	2.29	3.22	2.28	3.08	2.69			2.98	2.89	3.05	2.79
PBE-XDM	C					2.12	5.05			2.19	5.39	2.24	4.07
	P	3.38	6.61	3.39	6.60	3.33	6.83	3.45	6.28	3.30	6.94	3.32	6.89
B86bPBE-XDM	C					2.14	7.31			2.22	7.79	2.28	6.48
	P	3.25	8.00	3.26	7.97	3.18	8.33	3.34	7.54	3.15	8.50	3.17	8.40
Experimental nickel surface lattice constant (2.49 Å)													
PBE-XDM	C					2.14	4.93			2.15	4.91	2.24	3.53
	P	3.38	4.00	3.38	3.99	3.31	4.24	3.46	3.65	3.27	4.37	3.30	4.31
B86bPBE-XDM	C					2.16	7.29			2.24	7.33	2.26	6.10
	P	3.24	5.63	3.25	5.60	3.14	6.01	3.34	5.12	3.08	6.20	3.12	6.09
RPA[50]	C									2.17	6.46	2.17	5.02
	P									3.30	5.79	3.30	5.79
Experiment		d =2.04–2.18 Å[87,249] E_{ads} = 7.20–11.20 kJ/mol[53,244]											

Appendix C: Supporting Information for Chapter 7

Table C.0.1: Computed minimum-energy interlayer distances, in Å, for all orientations and all metals.

Orientation	Al	Cu	Ag	Au	Ni		Pd		Pt	
	P	P	P	P	C	P	C	P	C	P
bridge-fcc	3.64	3.29	3.17	3.34	–	3.25	2.23	–	–	3.40
bridge-hcp	3.61	3.29	3.18	3.34	–	3.26	2.25	–	–	3.42
bridge-top	3.56	3.24	3.10	3.26	2.14	3.18	2.12	–	2.10	3.29
fcc-hcp	3.69	3.35	3.27	3.44	–	3.34	–	3.26	–	3.50
top-fcc	3.61	3.22	3.06	3.22	2.22	3.15	2.25	–	2.40	3.22
top-hcp	3.48	3.23	3.09	3.25	2.28	3.17	2.28	–	2.45	3.32
$\sqrt{3} \times \sqrt{3}$	3.75	–	3.31	3.41	–	–	–	3.24	–	3.44

Figure C.0.1: Base functional contributions to the computed PES for graphene adsorption on selected metals.

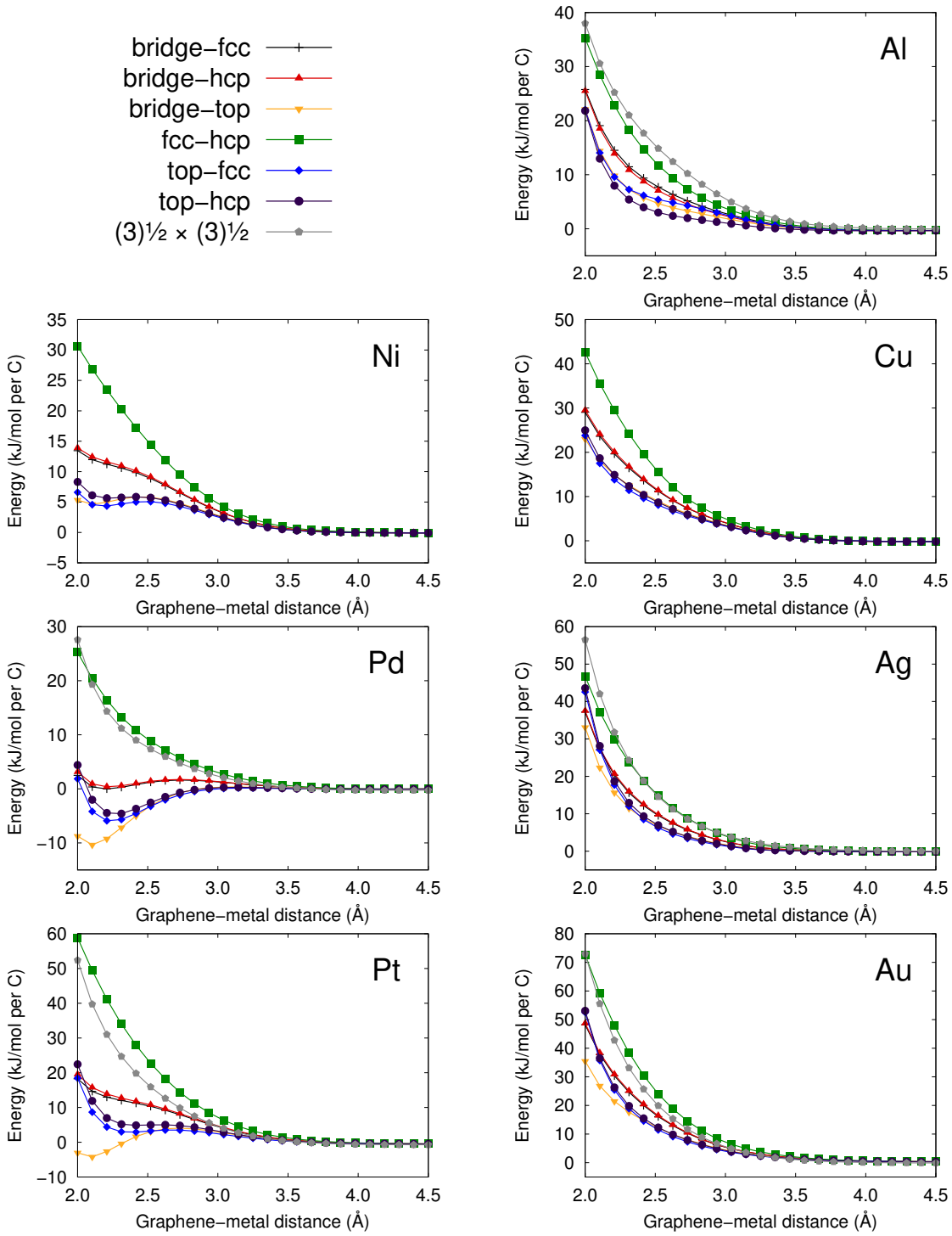

Figure C.0.2: XDM dispersion contributions to the computed PES for graphene adsorption on selected metals.

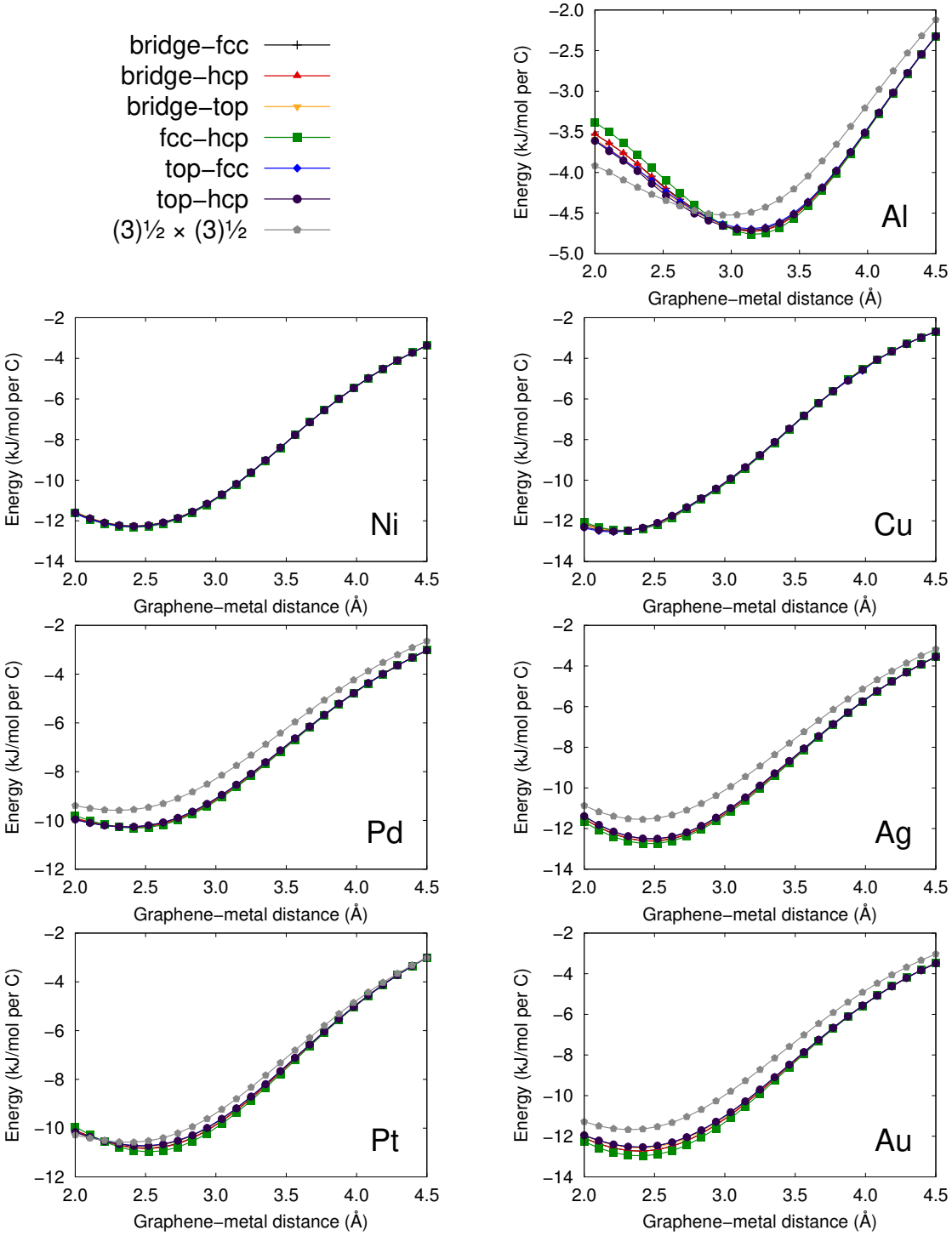

Appendix D: Supporting Information for Chapter 8

Figure D.0.1: PES for exfoliation of graphene from a graphene-metal or graphite base using experimental lattice constants.

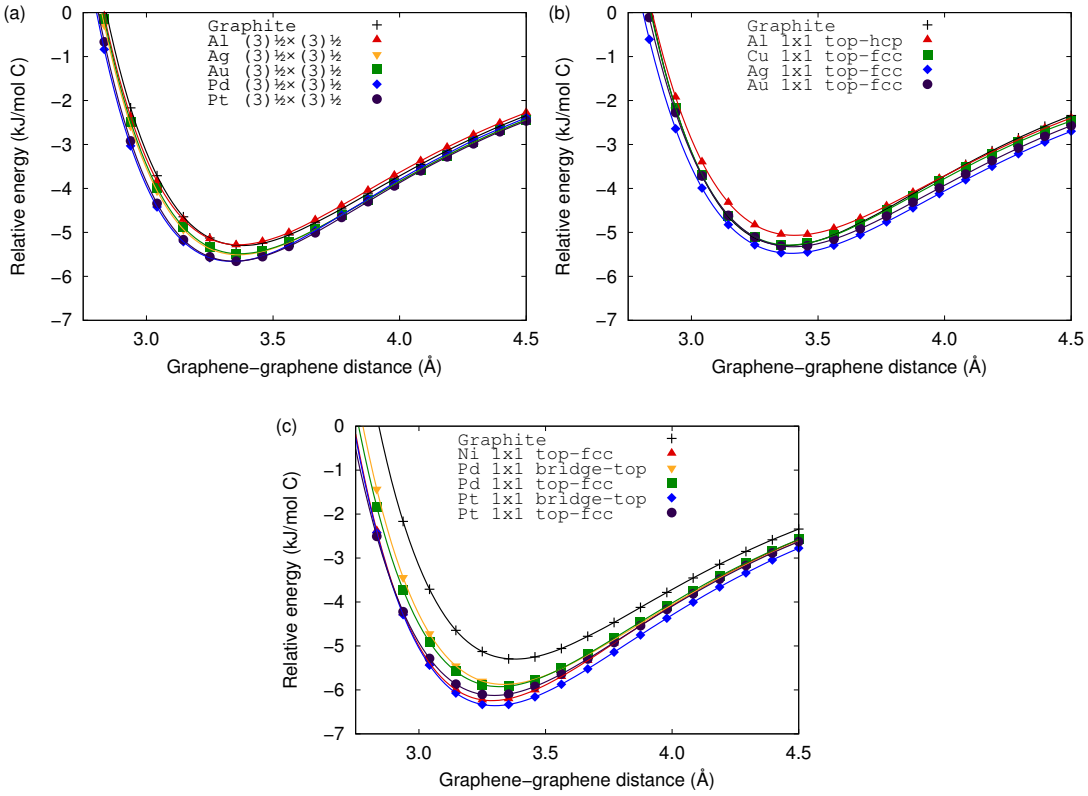

Appendix E: Statement of Contribution

The preceding thesis consists of papers that have been written during my graduate tenure. I carried out the primary calculations and investigations for these papers, as well as wrote the primary draft of the published manuscripts, while my co-authors primarily functioned in advisory and editorial roles.

Bibliography

[1] G. R. Bhimanapati, Z. Lin, V. Meunier, Y. Jung, J. Cha, S. Das, D. Xiao, Y. Son, M. S. Strano, V. R. Cooper, L. Liang, S. G. Louie, E. Ringe, W. Zhou, S. S. Kim, R. R. Naik, B. G. Sumpter, H. Terrones, F. Xia, Y. Wang, J. Zhu, D. Akinwande, N. Alem, J. A. Schuller, R. E. Schaak, M. Terrones, and J. A. Robinson, Recent Advances in Two-Dimensional Materials Beyond Graphene, ACS Nano **9**, 11509 (2015).

[2] R. Mas-Ballesté, C. Gómez-Navarro, J. Gómez-Herrero, and F. Zamora, 2D Materials: To Graphene and Beyond, Nanoscale **3**, 20 (2011).

[3] A. K. Geim, Graphene : Status and Prospects, Science **324**, 1530 (2009).

[4] A. H. Castro-Neto, F. Guinea, N. M. R. Peres, K. S. Novoselov, and A. K. Geim, The Electronic Properties of Graphene, Rev. Mod. Phys. **81**, 109 (2009).

[5] X. Zong, H. Yan, G. Wu, G. Ma, F. Wen, L. Wang, and C. Li, Enhancement of Photocatalytic H_2 Evolution on CdS by Loading MoS_2 as Cocatalyst under Visible Light Irradiation, J. Am. Chem. Soc. **130**, 7176 (2008).

[6] G. Eda, H. Yamaguchi, D. Voiry, T. Fujita, M. Chen, and M. Chhowalla, Photoluminescence From Chemically Exfoliated MoS_2, Nano Lett. **11**, 5111 (2011).

[7] X. Hong, J. Kim, S.-F. Shi, Y. Zhang, C. Jin, Y. Sun, S. Tongay, J. Wu, Y. Zhang, and F. Wang, Ultrafast Charge Transfer in Atomically Thin MoS_2/WS_2 Heterostructures, Nat. Nanotechnol. **9**, 682 (2014).

[8] D. Jariwala, V. K. Sangwan, L. J. Lauhon, T. J. Marks, and M. C. Hersam, Emerging Device Applications for Semiconducting Two-Dimensional Transition Metal Dichalcogenides, ACS Nano **8**, 1102 (2014).

[9] O. Penkov, H. J. Kim, H. J. Kim, and D. E. Kim, Tribology of Graphene: A Review, Int. J. Precis. Eng. Manuf. **15**, 577 (2014).

[10] T. W. Scharf and S. V. Prasad, Solid Lubricants: A Review, J. Mater. Sci. **48**, 511 (2013).

[11] J. C. Spear, B. W. Ewers, and J. D. Batteas, 2D-Nanomaterials for Controlling Friction and Wear at Interfaces, Nano Today **10**, 301 (2015).

[12] K. F. Mak and J. Shan, Photonics and Optoelectronics of 2D Semiconductor Transition Metal Dichalcogenides, Nat. Photonics **10**, 216 (2016).

[13] K. S. Novoselov, A. Mishchenko, A. Carvalho, and A. H. Castro Neto, 2D Materials and van der Waals Heterostructures, Science **353**, 461 (2016).

[14] K. S. Novoselov, D. Jiang, F. Schedin, T. J. Booth, V. V. Khotkevich, S. V. Morozov, and a. K. Geim, Two-Dimensional Atomic Crystals, Proc. Natl. Acad. Sci. U. S. A. **102**, 10451 (2005).

[15] M. Xu, T. Liang, M. Shi, and H. Chen, Graphene-Like Two-Dimensional Materials, Chem. Rev. **113**, 3766 (2013).

[16] J. Zhao, H. Liu, Z. Yu, R. Quhe, S. Zhou, Y. Wang, C. C. Liu, H. Zhong, N. Han, J. Lu, Y. Yao, and K. Wu, Rise of Silicene: A Competitive 2D Material, Prog. Mater. Sci. **83**, 24 (2016).

[17] K. S. Novoselov, A. K. Geim, S. Morozov, D. Jiang, Y. Zhang, S. Dubonos, I. Grigorieva, and A. A. Firsov, Electric Field Effect in Atomically Thin Carbon Films, Science **306**, 666 (2004).

[18] V. Singh, D. Joung, L. Zhai, S. Das, S. I. Khondaker, and S. Seal, Graphene Based Materials: Past, Present and Future, Prog. Mater. Sci. **56**, 1178 (2011).

[19] S. Li, Q. Li, R. W. Carpick, P. Gumbsch, X. Z. Liu, X. Ding, J. Sun, and J. Li, The Evolving Quality of Frictional Contact with Graphene, Nature **539**, 541 (2016).

[20] N. Bartelt and K. McCarty, Graphene Growth on Metal Surfaces, MRS Bull. **37**, 1158 (2012).

[21] X. Li, L. Colombo, and R. S. Ruoff, Synthesis of Graphene Films on Copper Foils by Chemical Vapor Deposition, Adv. Mater. **28**, 6247 (2016).

[22] R. Muñoz and C. Gómez-Aleixandre, Review of CVD Synthesis of Graphene, Chem. Vap. Depos. **19**, 297 (2013).

[23] M. Batzill, The Surface Science of Graphene: Metal Interfaces, CVD Synthesis, Nanoribbons, Chemical Modifications, and Defects, Surf. Sci. Rep. **67**, 83 (2012).

[24] D. Voiry, M. Salehi, R. Silva, T. Fujita, M. Chen, T. Asefa, V. B. Shenoy, G. Eda, and M. Chhowalla, Conducting MoS_2 Nanosheets as Catalysts for Hydrogen Evolution Reaction, Nano Lett. **13**, 6222 (2013).

[25] K. C. Knirsch, N. C. Berner, H. C. Nerl, C. S. Cucinotta, Z. Gholamvand, N. McEvoy, Z. Wang, I. Abramovic, P. Vecera, M. Halik, S. Sanvito, G. S. Duesberg, V. Nicolosi, F. Hauke, A. Hirsch, J. N. Coleman, and C. Backes, Basal-Plane Functionalization of Chemically Exfoliated Molybdenum Disulfide by Diazonium Salts, ACS Nano **9**, 6018 (2015).

[26] T. Heine, Transition Metal Chalcogenides: Ultrathin Inorganic Materials with Tunable Electronic Properties, Acc. Chem. Res. **48**, 65 (2015).

[27] J. Nam, D. C. Kim, H. Yun, D. H. Shin, S. Nam, W. K. Lee, J. Y. Hwang, S. W. Lee, H. Weman, and K. S. Kim, Chemical Vapor Deposition of Graphene on Platinum: Growth and Substrate Interaction, Carbon **111**, 733 (2017).

[28] I. Hernández-Rodríguez, J. M. García, J. A. Martín-Gago, P. L. de Andrés, and J. Méndez, Graphene Growth on Pt(111) and Au(111) Using a MBE Carbon Solid-Source, Diam. Relat. Mater. **57**, 58 (2015).

[29] C. Mattevi et al., A Review of Chemical Vapour Deposition of Graphene on Copper, J. Mater. Chem. **21**, 3324 (2011).

[30] J. Wintterlin and M. L. Bocquet, Graphene on Metal Surfaces, Surf. Sci. **603**, 1841 (2009).

[31] T. Oznuluer, E. Pince, E. O. Polat, O. Balci, O. Salihoglu, and C. Kocabas, Synthesis of Graphene on Gold, Appl. Phys. Lett. **98**, 183101 (2011).

[32] H. Ueta, M. Saida, C. Nakai, Y. Yamada, M. Sasaki, and S. Yamamoto, Highly Oriented Monolayer Graphite Formation on Pt(111) by a Supersonic Methane Beam, Surf. Sci. **560**, 183 (2004).

[33] S. Y. Kwon, C. V. Ciobanu, V. Petrova, V. B. Shenoy, J. Bareño, V. Gambin, I. Petrov, and S. Kodambaka, Growth of Semiconducting Graphene on Palladium, Nano Lett. **9**, 3985 (2009).

[34] Y. Murata, E. Starodub, B. B. Kappes, C. V. Ciobanu, N. C. Bartelt, K. F. McCarty, and S. Kodambaka, Orientation-Dependent Work Function of Graphene on Pd(111), Appl. Phys. Lett. **97**, 2014 (2010).

[35] P. A. Khomyakov, G. Giovannetti, P. C. Rusu, G. Brocks, J. Van Den Brink, and P. J. Kelly, First-Principles Study of the Interaction and Charge Transfer Between Graphene and Metals, Phys. Rev. B **79**, 195425 (2009).

[36] M. Vanin, J. Mortensen, A. Kelkkanen, J. Garcia-Lastra, K. Thygesen, and K. Jacobsen, Graphene on Metals: A van der Waals Density Functional Study, Phys. Rev. B **81**, 081408 (2010).

[37] I. Hamada and M. Otani, Comparative van der Waals Density-Functional Study of Graphene on Metal Surfaces, Phys. Rev. B **82**, 153412 (2010).

[38] S. M. Kozlov, F. Viñes, and A. Görling, Bonding Mechanisms of Graphene on Metal Surfaces, J. Phys. Chem. C **116**, 7360 (2012).

[39] T. Olsen and K. S. Thygesen, Random Phase Approximation Applied to Solids, Molecules, and Graphene-Metal Interfaces: From van der Waals to Covalent Bonding, Phys. Rev. B **87**, 075111 (2013).

[40] H. Li, K. Yu, Z. Tang, and Z. Zhu, Enhanced Hydrogen Evolution Performance of Ultra Thin Nanoslice/Nanopetal Structured XS_2 (X=W, Mo): From Experiment to Theory, J. Appl. Phys. **120**, 24301 (2016).

[41] Z. Ye, A. Balkanci, A. Martini, and M. Z. Baykara, Effect of Roughness on the Layer-Dependent Friction of Few-Layer Graphene, Phys. Rev. B **96**, 115401 (2017).

[42] Q. Li, C. Lee, R. W. Carpick, and J. Hone, Substrate Effect on Thickness-Dependent Friction on Graphene, Phys. Status Solidi Basic Res. **247**, 2909 (2010).

[43] J. Lee, K. S. Novoselov, and H. S. Shin, Interaction Between Metal and Graphene: Dependence on the Layer Number of Graphene, ACS Nano **5**, 608 (2011).

[44] D. Berman, A. Erdemir, and A. V. Sumant, Few layer Graphene to Reduce Wear and Friction on Sliding Steel Surfaces, Carbon **54**, 454 (2013).

[45] D. Berman, S. A. Deshmukh, S. K. R. S. Sankaranarayanan, A. Erdemir, and A. V. Sumant, Extraordinary Macroscale Wear Resistance of One Atom Thick Graphene Layer, Adv. Funct. Mater. **24**, 6640 (2014).

[46] H. Zhang, Z. Guo, H. Gao, and T. Chang, Stiffness-Dependent Interlayer Friction of Graphene, Carbon **94**, 60 (2015).

[47] W. Liu, J. Carrasco, B. Santra, A. Michaelides, M. Scheffler, and A. Tkatchenko, Benzene Adsorbed on Metals: Concerted Effect of Covalency and van der Waals Bonding, Phys. Rev. B **86**, 245405 (2012).

[48] J. Zheng, Y. Wang, L. Wang, R. Quhe, Z. Ni, W.-N. Mei, Z. Gao, D. Yu, J. Shi, and J. Lu, Interfacial Properties of Bilayer and Trilayer Graphene on Metal Substrates, Sci. Rep. **3**, 2081 (2013).

[49] C. Gong, G. Lee, B. Shan, E. M. Vogel, R. M. Wallace, and K. Cho, First-Principles Study of Metal-Graphene Interfaces, J. Appl. Phys. **108**, 123711 (2010).

[50] F. Mittendorfer, A. Garhofer, J. Redinger, J. Klimeš, J. Harl, and G. Kresse, Graphene on Ni(111): Strong Interaction and Weak Adsorption, Phys. Rev. B **84**, 201401 (2011).

[51] J. P. P. Ramalho, J. R. B. Gomes, and F. Illas, Accounting for van der Waals Interactions Between Adsorbates and Surfaces in Density Functional Theory Based Calculations: Selected Examples, RSC Adv. **3**, 13085 (2013).

[52] W. Zhao, S. M. Kozlov, H. Oliver, K. Gotterbarm, M. P. a. Lorenz, F. Viñes, C. Papp, G. Andreas, and H.-P. Steinrück, Graphene on Ni (111): Coexistence of Different Surface Structures, J. Chem. Phys. Lett. **2**, 759 (2011).

[53] P. Janthon, F. Viñes, S. M. Kozlov, J. Limtrakul, and F. Illas, Theoretical Assessment of Graphene-Metal Contacts, J. Chem. Phys. **138**, 244701 (2013).

[54] A. F. Kuloglu, B. Sarikavak-Lisesivdin, S. B. Lisesivdin, and E. Ozbay, First-Principles Calculations of Pd-Terminated Symmetrical Armchair Graphene Nanoribbons, Comput. Mater. Sci. **68**, 18 (2013).

[55] F. Furche, Developing the Random Phase Approximation into a Practical Post-Kohn-Sham Correlation Model, J. Chem. Phys. **129**, 114105 (2008).

[56] S. Grimme, J. Antony, S. Ehrlich, and H. Krieg, A Consistent and Accurate Ab Initio Parametrization of Density Functional Dispersion Correction (DFT-D) for the 94 Elements H-Pu, J. Chem. Phys. **132**, 154104 (2010).

[57] S. Grimme, Semiempirical GGA-Type Density Functional Constructed with a Long-Range Dispersion Correction, J. Comp. Chem. **27**, 1787 (2006).

[58] A. Tkatchenko and M. Scheffler, Accurate Molecular van der Waals Interactions from Ground-State Electron Density and Free-Atom Reference Data, Phys. Rev. Lett. **102**, 073005 (2009).

[59] A. Tkatchenko, L. Romaner, O. T. Hofmann, E. Zojer, C. Ambrosch-Draxl, and M. Scheffler, Van der Waals Interactions Between Organic Adsorbates and at Organic/Inorganic Interfaces, MRS Bull. **35**, 435 (2010).

[60] A. D. Becke and E. R. Johnson, Exchange-Hole Dipole Moment and the Dispersion Interaction Revisited, J. Chem. Phys. **127**, 154108 (2007).

[61] A. Otero-de-la-Roza and E. R. Johnson, Van der Waals Interactions in Solids Using the Exchange-Hole Dipole Moment, J. Chem. Phys. **136**, 174109 (2012).

[62] A. Tkatchenko, R. A. DiStasio, R. Car, and M. Scheffler, Accurate and Efficient Method for Many-Body van der Waals Interactions, Phys. Rev. Lett. **108**, 236402 (2012).

[63] A. Ambrosetti, A. M. Reilly, R. A. DiStasio, and A. Tkatchenko, Long-Range Correlation Energy Calculated From Coupled Atomic Response Functions, J. Chem. Phys. **140**, 18A508 (2014).

[64] M. S. Christian, A. Otero-de-la-Roza, and E. R. Johnson, Surface Adsorption from the Exchange-Hole Dipole Moment Dispersion Model, J. Chem. Theory Comput. **12**, 3305 (2016), Chapter 5 in this thesis.

[65] G. Ehrlich, Interaction of Nitrogen With a Tungsten Surface, J. Phys. Chem. **60**, 1388 (1956).

[66] A. de Jong and J. Niemantsverdriet, Thermal Desorption Analysis: Comparative Test of Ten Commonly Applied Procedures, Surf. Sci. **233**, 355 (1990).

[67] E. Tomkova, TDS Spectra Analysis, Surf. Sci. **351**, 309 (1996).

[68] D. Nieskens, A. van Bavel, and J. Niemantsverdriet, The Analysis of Temperature Programmed Desorption Experiments of Systems with Lateral Interactions; Implications of the Compensation Effect, Surf. Sci. **546**, 159 (2003).

[69] E. Seebauer, A. Kong, and L. Schmidt, The Coverage Dependence of the Pre-Exponential Factor for Desorption, Surf. Sci. **193**, 417 (1988).

[70] D. A. King, Thermal Desorption From Metal Surfaces: A Review, Surf. Sci. **47**, 384 (1975).

[71] J. L. Falconer and R. J. Madix, Desorption Rate Isotherms in Flash Desorption Analysis, J. Catal. **48**, 262 (1977).

[72] P. Redhead, Thermal Desorption of Gases, Vacuum **12**, 203 (1962).

[73] M. Xi, M. X. Yang, S. K. Jo, B. E. Bent, and P. Stevens, Benzene Adsorption on Cu(111): Formation of a Stable Bilayer, J. Chem. Phys. **101**, 9122 (1994).

[74] K. E. Smith and S. D. Kevan, The Electronic Structure of Solids Studied Using Angle Resolved Photoemission Spectroscopy, Prog. Solid State Chem. **21**, 49 (1991).

[75] A. A. Kordyuk, ARPES Experiment in Fermiology of Quasi-2D Metals (Review Article), Low Temp. Phys. **40**, 286 (2014).

[76] A. Damascelli, Z. Hussain, and Z.-X. Shen, Angle-Resolved Photoemission Studies of the Cuprate Superconductors, Rev. Mod. Phys. **75**, 473 (2003).

[77] A. A. Kordyuk and S. V. Borisenko, ARPES on High-Temperature Superconductors: Simplicity vs. Complexity, Low Temp. Phys. **32**, 298 (2006).

[78] J. Wollschläger, Simple Analysis of Spot Splitting Due to Diffraction at Surfaces with Atomic Steps, Surf. Sci. **383**, 103 (1997).

[79] F. Jona, LEED Crystallography, J. Phys. C **11**, 4271 (1978).

[80] K. Heinz and L. Hammer, Surface Crystallography by Low Energy Electron Diffraction, Zeitschrift für Krist. **213**, 615 (1998).

[81] R. D. Diehl, J. Ledieu, N. Ferralis, A. W. Szmodis, and R. Mcgrath, Low-Energy Electron Diffraction from Quasicrystal, Surf. Sci. **15**, R63 (2003).

[82] C. Leslie, E. Landree, C. Collazo-Davila, E. Bengu, D. Grozea, and L. D. Marks, Electron Crystallography in Surface Structure Analysis, Microsc. Res. Tech. **46**, 160 (1999).

[83] V. Blum and K. Heinz, Fast LEED Intensity Calculations for Surface Crystallography using Tensor LEED, Comput. Phys. Commun. **134**, 392 (2001).

[84] R. D and M. A. H. Van, Global Optimization in LEED Structure Determination using Genetic Algorithms, Surf. Sci. **355**, L393 (1996).

[85] E. A. Soares, C. M. De Castilho, and V. E. De Carvalho, Advances on Surface Structural Determination by LEED, J. Phys. Condens. Matter **23**, 303001 (2011).

[86] S. Nie, J. M. Wofford, N. C. Bartelt, O. D. Dubon, and K. F. McCarty, Origin of the Mosaicity in Graphene Grown on Cu(111), Phys. Rev. B **84**, 155425 (2011).

[87] Y. Gamo, A. Nagashima, M. Wakabayashi, M. Terai, and C. Oshima, Atomic Structure of Monolayer Graphite Formed on Ni(111), Surf. Sci. **17**, 745 (1996).

[88] P. Sutter, J. T. Sadowski, and E. Sutter, Graphene on Pt(111): Growth and Substrate Interaction, Phys. Rev. B **80**, 245411 (2009).

[89] J. M. Wofford, E. Starodub, A. L. Walter, S. Nie, A. Bostwick, N. C. Bartelt, K. Thürmer, E. Rotenberg, K. F. McCarty, and O. D. Dubon, Extraordinary Epitaxial Alignment of Graphene Islands on Au(111), New J. Phys. **14**, 053008 (2012).

[90] Y. Liu, K. M. Leung, H. Y. Nie, W. M. Lau, and J. Yang, A New AFM Nanotribology Method using a T-shape Cantilever with an Off-Axis Tip for Friction Coefficient Measurement with Minimized Abbé Error, Tribol. Lett. **41**, 313 (2011).

[91] M. L. Palacio and B. Bhushan, Normal and Lateral Force Calibration Techniques for AFM Cantilevers, Crit. Rev. Solid State Mater. Sci. **35**, 73 (2010).

[92] E. Tocha, H. Schönherr, and G. Julius Vancso, Quantitative Nanotribology by AFM: A Novel Universal Calibration Platform, Langmuir **22**, 2340 (2006).

[93] L. Y. Lin, D. E. Kim, W. K. Kim, and S. C. Jun, Friction and Wear Characteristics of Multi-Layer Graphene Films Investigated by Atomic Force Microscopy, Surf. Coatings Technol. **205**, 4864 (2011).

[94] H. J. Butt, B. Cappella, and M. Kappl, Force Measurements with the Atomic Force Microscope: Technique, Interpretation and Applications, Surf. Sci. Rep. **59**, 1 (2005).

[95] C. Lee, X. Wei, Q. Li, R. Carpick, J. W. Kysar, and J. Hone, Elastic and Frictional Properties of Graphene, Phys. Status Solidi **246**, 2562 (2009).

[96] D. H. Cho, L. Wang, J. S. Kim, G. H. Lee, E. S. Kim, S. Lee, S. Y. Lee, J. Hone, and C. Lee, Effect of Surface Morphology on Friction of Graphene on Various Substrates, Nanoscale **5**, 3063 (2013).

[97] C. Mak and J. Krim, Quartz-Crystal Microbalance Studies of the Velocity Dependence of Interfacial Friction, Phys. Rev. B **58**, 5157 (1998).

[98] J. Krim, Friction and Energy Dissipation Mechanisms in Adsorbed Molecules and Molecularly Thin Films, Adv. Phys. **61**, 155 (2012).

[99] J. B. Sokoloff, J. Krim, and A. Widom, Determination of an Atomic-Scale Frictional Force Law Through Quartz-Crystal Microbalance Measurements, Phys. Rev. B **48**, 9134 (1993).

[100] J. Krim and A. Widom, Damping of a Crystal Oscillator by an Adsorbed Monolayer and its Relation to Interfacial Viscosity, Phys. Rev. B **38**, 12184 (1988).

[101] M. Walker, C. Jaye, J. Krim, and M. W. Cole, Frictional Temperature Rise in a Sliding Physisorbed Monolayer of Kr/Graphene, J. Phys. Condens. Mat. **24**, 424201 (2012).

[102] T. Coffey and J. Krim, Impact of Substrate Corrugation on the Sliding Friction Levels of Adsorbed Films, Phys. Rev. Lett. **95**, 076101 (2005).

[103] F. Bloch, Über die Quantenmechanik der Elektronen in Kristallgittern, Zeitschrift für Physik **52**, 555 (1928).

[104] H. J. Monkhorst and J. D. Pack, Special Points for Brillouin-Zone Integrations, Phys. Rev. B **13**, 5188 (1976).

[105] N. D. Mermin, Thermal Properties of the Inhomogeneous Electron Gas, Phys. Rev. A **137**, 1441 (1965).

[106] A. De Vita, *The Energetics of Defects and Impurities in Metals and Ionic Materials from First Principles*, PhD thesis, University of Keele, 1992.

[107] M. Methfessel and A. T. Paxton, High-Precision Sampling for Brillouin-Zone Integration in Metals, Phys. Rev. B **40**, 3616 (1989).

[108] N. Marzari, D. Vanderbilt, A. De Vita, and M. C. Payne, Thermal Contraction and Disordering of the Al(110) Surface, Phys. Rev. Lett. **82**, 3296 (1999).

[109] D. Hamann, M. Schlüter, and C. Chiang, Norm-Conserving Pseudopotentials, Phys. Rev. Lett. **43**, 1494 (1979).

[110] D. Vanderbilt, Soft Self-Consistent Pseudopotentials in a Generalized Eigenvalue Formalism, Phys. Rev. B **41**, 7892 (1990).

[111] J. C. Slater, Wave Functions in a Periodic Potential, Phys. Rev. **51**, 846 (1937).

[112] O. K. Andersen, Linear Methods in Band Theory, Phys. Rev. B **12**, 3060 (1975).

[113] C. Herring, A New Method for Calculating Wave Functions in Crystals, Phys. Rev. **57**, 1169 (1940).

[114] P. E. Blöchl, Projector Augmented-Wave Method, Phys. Rev. B **50**, 17953 (1994).

[115] G. Kresse and D. Joubert, From Ultrasoft Pseudopotentials to the Projector Augmented-Wave Method, Phys. Rev. B **59**, 1758 (1999).

[116] R. F. W. Bader, *Atoms in Molecules: A Quantum Theory*, Oxford University Press, Oxford, 1990.

[117] R. F. W. Bader, M. T. Carroll, J. R. Cheeseman, and C. Chang, Properties of Atoms in Molecules: Atomic Volumes, J. Am. Chem. Soc. **109**, 7968 (1987).

[118] M. Yu and D. R. Trinkle, Accurate and Efficient Algorithm for Bader Charge Integration, J. Chem. Phys. **134**, 064111 (2011).

[119] W. Kohn and L. J. Sham, Self-Consistent Equations Including Exchange and Correlation Effects, Phys. Rev. **140**, A1133 (1965).

[120] D. M. Ceperley and B. J. Alder, Ground State of the Electron Gas by a Stochastic Model, Phys. Rev. Lett. **45**, 566 (1980).

[121] T. Björkman, A. Gulans, A. V. Krasheninnikov, and R. M. Nieminen, Are We van der Waals Ready?, J. Phys. Condens. Matter **24**, 424218 (2012).

[122] D. N. P. Sony, P. Puschnig and C. Ambrosch-Draxl, Importance of Van der Waals Interaction for Organic Molecule-Metal Junctions: Adsorption of Thiophene on Cu(110) as a Prototype, Phys. Rev. Lett. **99**, 176401 (2007).

[123] H. Ihm, H. M. Ajo, J. M. Gottfrie, P. Bera, and C. T. Campbell, Calorimetric Measurement of the Heat of Adsorption of Benzene on Pt(111), J. Phys. Chem. B **108**, 14627 (2004).

[124] V. G. Ruiz, W. Liu, E. Zojer, M. Scheffler, and A. Tkatchenko, Density-Functional Theory with Screened van der Waals Interactions for the Modeling of Hybrid Inorganic-Organic Systems, Phys. Rev. Lett. **108**, 146103 (2012).

[125] A. Bilić, J. R. Reimers, N. S. Hush, R. C. Hoft, and M. J. Ford, Adsorption of Benzene on Copper, Silver, and Gold Surfaces, J. Chem. Theory Comput. **2**, 1093 (2006).

[126] J. Perdew, K. Burke, and M. Ernzerhof, Generalized Gradient Approximation Made Simple, Phys. Rev. Lett. **77**, 3865 (1996).

[127] G. P. Chen, V. K. Voora, M. M. Agee, S. G. Balasubramani, and F. Furche, Random-Phase Approximation Methods, Annu. Rev. Phys. Chem. **68**, 421 (2017).

[128] F. Furche, Molecular Tests of the Random Phase Approximation to the Exchange-Correlation Energy Functional, Phys. Rev. B **64**, 195120 (2001).

[129] F. Furche and T. Van Voorhis, Fluctuation-Dissipation Theorem Density-Functional Theory, J. Chem. Phys. **122**, 164106 (2005).

[130] X. Ren, P. Rinke, C. Joas, and M. Scheffler, Random-Phase Approximation and its Applications in Computational Chemistry and Materials Science, J. Mat. Sci. **47**, 7447 (2012).

[131] H. Eshuis and F. Furche, A Parameter-Free Density Functional that Works for Noncovalent Interactions, J. Phys. Chem. Lett. **2**, 983 (2011).

[132] H. Eshuis, J. Yarkony, and F. Furche, Fast Computation of Molecular Random Phase Approximation Correlation Energies using Resolution of the Identity and Imaginary Frequency Integration, J. Chem. Phys. **132**, 234114 (2010).

[133] M. Dion, H. Rydberg, E. Schröder, D. C. Langreth, and B. I. Lundqvist, Van der Waals Density Functional for General Geometries, Phys. Rev. Lett. **92**, 246401 (2004).

[134] J. Wellendorff, A. Kelkkanen, J. J. Mortensen, B. I. Lundqvist, and T. Bligaard, RPBE-vdW Description of Benzene Adsorption on Au (111), Top. Catal. **53**, 378 (2010).

[135] D. Carter and A. L. Rohl, Van der Waals Corrected Density Functional Calculations of the Adsoprtion of Benzene on the Cu (111) Surface, J. Comp. Chem. **35**, 2263 (2014).

[136] S. Lukas, S. Vollmer, G. Witte, and C. Wall, Adsorption of Acenes on Flat and Vicinal Cu(111) Surfaces: Step Induced Formation of Lateral Order, J. Chem. Phys. **114**, 10123 (2001).

[137] K. Toyoda, Y. Nakano, I. Hamada, K. Lee, S. Yanagisawa, and Y. Morikawa, First-Principles Study of the Pentacene/Cu(111) Interface: Adsorption States and Vacuum Level Shifts, J. Electron Spectros. Relat. Phenomena **174**, 78 (2009).

[138] K. Toyoda, I. Hamada, K. Lee, S. Yanagisawa, and Y. Morikawa, Density Functional Theoretical Study of Pentacene/Noble Metal Interfaces With van der Waals Corrections: Vacuum Level Shifts and Electronic Structures, J. Chem. Phys. **132**, 134703 (2010).

[139] R. Ahlrichs, R. Penco, and G. Scoles, Intermolecular Forces in Simple Systems, Chem. Phys. **19**, 119 (1977).

[140] S. Grimme, Accurate Description of van der Waals Complexes by Density Functional Theory Including Empirical Corrections, J. Comp. Chem. **25**, 1463 (2004).

[141] M. Callsen, N. Atodiresei, V. Caciuc, and S. Blügel, Semiempirical van der Waals Interactions Versus Ab Initio Nonlocal Correlation Effects in the Thiophene-Cu(111) System, Phys. Rev. B **86**, 085439 (2012).

[142] P. K. Milligan, B. Murphy, D. Lennon, B. C. C. Cowie, and M. Kadodwala, A Complete Structural Study of the Coverage Dependence of the Bonding of Thiophene on Cu(111), J. Phys. Chem. B **105**, 140 (2001).

[143] O. Anatole von Lilienfeld and A. Tkatchenko, Two- and Three-Body Interatomic Dispersion Energy Contributions to Binding in Molecules and Solids, J. Chem. Phys. **132**, 234109 (2010).

[144] E. M. Lifshitz, The Theory of Molecular Attractive Forces Between Solids, Sov. Phys. Rev. Lett. **2**, 73 (1956).

[145] E. Zaremba and W. Kohn, Van der Waals Interaction Between an Atom and a Solid Surface, Phys. Rev. B **13**, 2270 (1976).

[146] R. A. Distasio, V. V. Gobre, and A. Tkatchenko, Many-Body van der Waals Interactions in Molecules and Condensed Matter, J. Phys. Condens. Matter **26**, 213202 (2014).

[147] R. J. Maurer, V. G. Ruiz, and A. Tkatchenko, Many-Body Dispersion Effects in the Binding of Adsorbates on Metal Surfaces, J. Chem. Phys. **143**, 102808 (2015).

[148] W. Liu, F. Maaß, M. Willenbockel, C. Bronner, M. Schulze, S. Soubatch, F. S. Tautz, P. Tegeder, and A. Tkatchenko, Quantitative Prediction of Molecular Adsorption: Structure and Binding of Benzene on Coinage Metals, Phys. Rev. Lett. **115**, 036104 (2015).

[149] A. Otero-de-la-Roza, J. D. Mallory, and E. R. Johnson, Metallophilic Interactions from Dispersion-Corrected Density-Functional Theory, J. Chem. Phys. **140**, 18A504 (2014).

[150] A. Otero-de-la-Roza and E. R. Johnson, Non-Covalent Interactions and Thermochemistry Using XDM-Corrected Hybrid and Range-Separated Hybrid Density Functionals, J. Chem. Phys. **138**, 204109 (2013).

[151] A. Otero-de-la-Roza and E. R. Johnson, A Benchmark for Non-Covalent Interactions in Solids, J. Chem. Phys. **137**, 054103 (2012).

[152] V. V. Tsukruk, F. Rinderspacher, and V. N. Bliznyuk, Self-Assembled Multilayer Films from Dendrimers, Langmuir **13**, 2171 (1997).

[153] J. R. Heath, Molecular Electronics, Annu. Rev. Mater. Res. **39**, 1 (2009).

[154] J. C. Scott, Metal Organic Interface and Charge Injection in Organic Electronic Devices, J. Vac. Sci. Technol. A **21**, 521 (2003).

[155] V. Johánek, S. Schauermann, M. Laurin, C. S. Gopinath, J. Libuda, and H.-J. Freund, On the Role of Different Adsorption and Reaction Sites on Supported Nanoparticles During a Catalytic Reaction: NO Decomposition on a Pd/Alumina Model Catalyst, J. Phys. Chem. B **108**, 14244 (2004).

[156] P. Väterlein, M. Schmelzer, J. Taborski, T. Krause, F. Viczian, M. Bässler, R. Fink, E. Umbach, and W. Wurth, Orientation and Bonding of Thiophene and 2,2-Bithiophene on Ag(111): A Combined Near Edge Extended X-Ray Absorption Fine Structure and Xα Scattered-Wave Study, Surf. Sci. **452**, 20 (2000).

[157] G. Liu, J. A. Rodriguez, J. Dvorak, J. Hrbek, and T. Jirsak, Chemistry of Sulfur-Containing Molecules on Au: Thiophene, Sulfur Dioxide, and Methanethiol Adsorption, Surf. Sci. **505**, 295 (2002).

[158] A. Mulligan, S. M. Johnston, G. Miller, V. Dhanak, and M. Kadodwala, A TPD and NIXSW Investigation of Furan and Tetrahydrofuran Adsorption on Cu(111), Surf. Sci. **541**, 3 (2003).

[159] Q. Zhong, C. Gahl, and M. Wolf, Two-Photon Photoemission Spectroscopy of Pyridine Adsorbed on Cu, Surf. Sci. **496**, 21 (2002).

[160] M. Dell'Angela, G. Kladnik, A. Cossaro, A. Verdini, M. Kamenetska, I. Tamblyn, S. Y. Quek, J. B. Neaton, D. Cvetko, A. Morgante, and L. Venkataraman, Relating Energy Level Alignment and Amine-Linked Single Molecule Junction Conductance, Nano Lett. **10**, 2470 (2010).

[161] W. Liu, A. Tkatchenko, and M. Scheffler, Modeling Adsorption and Reactions of Organic Molecules at Metal Surfaces, Acc. Chem. Res. **47**, 3369 (2014).

[162] J. R. Reimers, D. Panduwinata, J. Visser, Y. Chin, C. G. Tang, L. Goerigk, M. J. Ford, M. Sintic, T. J. Sum, M. J. J. Coenen, B. L. M. Hendriksen, J. A. A. Elemans, N. S. Hush, and C. M. J, A Priori Calculations of the Free Energy of Formation from Solution of Polymorphic Self-Assembled Monolayers, Proc. Nat. Acad. Sci. **112**, E6101–E6110 (2015).

[163] J. R. Reimers, D. Panduwinata, J. Visser, Y. Chin, C. G. Tang, L. Goerigk, M. J. Ford, M. Baker, T. J. Sum, M. J. J. Coenen, B. L. M. Hendriksen, J. A. A. Elemans, N. S. Hush, and C. M. J, From Chaos to Order: Chain-Length Dependence of the Free Energy of Formation of Meso-Tetraalkylporphyrin Self-Assembled Monolayer Polymorphs, J. Phys. Chem. C **120**, 1739 (2016).

[164] E. R. Johnson, I. D. Mackie, and G. A. DiLabio, Dispersion Interactions in Density-Functional Theory, J. Phys. Org. Chem. **22**, 1127 (2009).

[165] G. A. DiLabio and A. Otero-de-la-Roza, Non-Covalent Interactions in Density-Functional Theory, in *Reviews in Computational Chemistry*, edited by K. B. Lipkowitz, Wiley-VCH, Hoboken, NJ, 2014.

[166] A. Bilic, J. R. Reimers, N. S. Hush, R. C. Hoft, and M. J. Ford, Adsorption of Benzene on Copper, Silver, and Gold Surfaces, J. Chem. Theory Comput. **2**, 1093 (2006).

[167] L. Ferrighi, G. K. H. Madsen, and B. Hammer, Self-Consistent Meta-Generalized Gradient Approximation Study of Adsorption of Aromatic Molecules on Noble Metal Surfaces, J. Chem. Phys. **135**, 084704 (2011).

[168] K. Tonigold and A. Gross, Adsorption of Small Aromatic Molecules on the (111) Surfaces of Noble Metals: A Density Functional Theory Study with Semiempirical Corrections for Dispersion Effects, J. Chem. Phys. **132**, 224701 (2010).

[169] W. Reckien, M. Eggers, and T. Bredow, Theoretical Study of the Adsorption of Benzene on Coinage Metals, Beilstein J. Org. Chem. **10**, 1775 (2014).

[170] T. S. Chwee and M. B. Sullivan, Adsorption Studies of C6H6 on Cu (111), Ag (111), and Au (111) Within Dispersion Corrected Density Functional Theory, J. Chem. Phys. **137**, 134703 (2012).

[171] W. Liu, V. G. Ruiz, G. X. Zhang, B. Santra, X. Ren, M. Scheffler, and A. Tkatchenko, Structure and Energetics of Benzene Adsorbed on Transition-Metal Surfaces: Density-Functional Theory with van der Waals

Interactions Including Collective Substrate Response, New J. Phys. **15**, 053046 (2013).

[172] J. Carrasco, W. Liu, A. Michaelides, and A. Tkatchenko, Insight Into the Description of van der Waals Forces for Benzene Adsorption on Transition Metal (111) Surfaces, J. Chem. Phys. **140**, 084704 (2014).

[173] H. Yildirim, T. Greber, and A. Kara, Trends in Adsorption Characteristics of Benzene on Transition Metal Surfaces: Role of Surface Chemistry and van der Waals Interactions, J. Phys. Chem. C **117**, 20572 (2013).

[174] P. L. Silvestrelli and A. Ambrosetti, Inclusion of Screening Effects in the van der Waals Corrected DFT Simulation of Adsorption Processes on Metal Surfaces, Phys. Rev. B **87**, 075401 (2013).

[175] H. Peng, Z. H. Yang, J. Sun, and J. P. Perdew, SCAN+rVV10: A Promising van der Waals Density Functional, Phys. Rev. X **6**, 041005 (2015).

[176] E. R. Johnson and A. D. Becke, A Post-Hartree-Fock Model of Intermolecular Interactions: Inclusion of Higher-Order Corrections, J. Chem. Phys. **124**, 174104 (2006).

[177] E. R. Johnson, S. Keinan, P. Mori-Sánchez, J. Contreras-García, A. J. Cohen, and W. Yang, Revealing Noncovalent Interactions, J. Am. Chem. Soc. **132**, 6498 (2010).

[178] A. Otero-de-la-Roza, E. R. Johnson, and J. Contreras-Garcia, Revealing Non-Covalent Interactions in Solids: NCI Plots Revisited, Phys. Chem. Chem. Phys. **14**, 12165 (2012).

[179] P. Giannozzi, S. Baroni, and et. al., Quantum ESPRESSO: A Modular and Open-Source Software Project for Quantum Simulations of Materials, J. Phys. Condens. Mat. **21**, 395502 (2009).

[180] A. D. Becke, On the Large Gradient Behavior of the Density Functional Exchange Energy, J. Chem. Phys. **85**, 7184 (1986).

[181] S. G. Louie, S. Froyen, and M. L. Cohen, Nonlinear Ionic Pseudopotentials in Spin-Density-Functional Calculations, Phys. Rev. B **26**, 1738 (1982).

[182] A. Otero-de-la-Roza, E. R. Johnson, and V. Luaña, Critic2: A Program for Real-Space Analysis of Quantum Chemical Interactions in Solids, Comput. Phys. Commun. **185**, 1007 (2014).

[183] A. Hansen, C. Bannwarth, S. Grimme, P. Petrović, C. Werlé, and J.-P. Djukic, The Thermochemistry of London Dispersion-Driven Transition Metal Reactions: Getting the Right Answer for the Right Reason, ChemistryOpen **3**, 177 (2014).

[184] K. Lee, É. D. Murray, L. Kong, B. I. Lundqvist, and D. C. Langreth, Higher-Accuracy van der Waals Density Functional, Phys. Rev. B **82**, 081101 (2010).

[185] D. J. Lacks and R. G. Gordon, Pair Interactions of Rare-Gas Atoms as a Test of Exchange-Energy-Density Functionals in Regions of Large Density Gradients, Phys. Rev. A **47**, 4681 (1993).

[186] F. L. Hirshfeld, Bonded-Atom Fragments for Describing Molecular Charge Densities, Theor. Chim. Acta **44**, 129 (1977).

[187] A. D. Becke and M. R. Roussel, Exchange Holes in Inhomogeneous Systems: A Coordinate-Space Model, Phys. Rev. A **39**, 3761 (1989).

[188] A. D. Becke and E. R. Johnson, Exchange-Hole Dipole Moment and the Dispersion Interaction: High-Order Dispersion Coefficients, J. Chem. Phys. **124**, 014104 (2006).

[189] E. R. Johnson, Dependence of Dispersion Coefficients on Atomic Environment, J. Chem. Phys. **135**, 234109 (2011).

[190] P. Mori-Sánchez, A. Martín Pendás, and V. Luaña, A Classification of Covalent, Ionic, and Metallic Solids Based on the Electron Density, J. Am. Chem. Soc. **124**, 14721 (2002).

[191] G. Li, I. Tamblyn, V. R. Cooper, H.-J. Gao, and J. B. Neaton, Molecular Adsorption on Metal Surfaces with van der Waals Density Functionals, Phys. Rev. B **85**, 121409 (2012).

[192] X. L. Zhou, M. Castro, and J. White, Interactions of UV Photons and Low Energy Electrons with Chemisorbed Benzene on Ag(111), Surf. Sci. **238**, 215 (1990).

[193] B. Sexton, A Vibrational and TDS Study of the Adosprtion of Pyrrole, Furan and Thiophene on Cu(100): Evidence for pi-bonded and Inclined Species, Surf. Sci. **163**, 99 (1985).

[194] P. Milligan, J. McNamarra, B. Murphy, B. Cowie, D. Lennon, and M. Kadodwala, A NIXSW and NEXAFS Investigation of Thiophene on Cu(111), Surf. Sci. **412**, 166 (1998).

[195] C. J. Barnes, C. M. Whelan, C. Gregoire, and J. J. Pireaux, A HREELS Study of Benzenethiol Adsorption on Au(111) and Au(322), Surf. Rev. Lett. **06**, 193 (1999).

[196] F. Schreiber, Structure and Growth of Self-Assembling Monolayers, Prog. Surf. Sci. **65**, 151 (2000).

[197] K. T. Carron and L. G. Hurley, Axial and Azimuthal Angle Determination with Surface-Enhanced Raman Spectroscopy: Thiophenol on Copper, Silver, and Gold Metal Surfaces, J. Phys. Chem. **95**, 9979 (1991).

[198] P. Avouris and J. E. Demuth, Electronic Excitations of Benzene, Pyridine, and Pyrazine Adsorbed on Ag(111), J. Chem. Phys. **75**, 4783 (1981).

[199] W. Xu, R. E. A. Kelly, R. Otero, M. Schöck, E. Lœgsgaard, I. Stensgaard, L. N. Kantorovich, and F. Besenbacher, Probing the Hierachy of Thymine-Thymine Interactions in Self-Assembled Structures by Manipulation with Scanning Tunneling Micrscopy, Small **3**, 2011 (2007).

[200] B. Roelfs, E. Bunge, C. Schröter, T. Solomun, H. Meyer, R. J. Nichols, and H. Baumgärtel, Adsorption of Thymine on Gold Single-Crystal Electrodes, J. Phys. Chem. B **101**, 754 (1997).

[201] L. M. Demers, M. Östblom, H. Zhang, N. H. Jang, B. Liedberg, and C. A. Mirkin, Thermal Desorption Behavior and Binding Properties of DNA Bases and Nucleosides on Gold, J. Am. Chem. Soc. **124**, 11248 (2002).

[202] M. Östblom, B. Liedberg, L. M. Demers, and C. A. Mirkin, On the Structure and Desorption Dynamics of DNA Bases Adsorbed on Gold: A Temperature-Programmed Study, J. Phys. Chem. B **109**, 15150 (2005).

[203] N. J. Tao, J. A. DeRose, and S. M. Lindsay, Self-Assembly of Molecular Superstructures Studied by In Situ Scanning Tunneling Microscopy: DNA Bases on Gold (111), J. Phys. Chem. **97**, 910 (1993).

[204] R. Otero, M. Lukas, R. E. A. Kelly, W. Xu, E. Laegsgaard, I. Stensgaard, L. N. Kantorovich, and F. Besenbacher, Elementary Structural Motifs in a Random Network of Cytosine Adsorbed on a Gold(111) Surface, Science **319**, 312 (2008).

[205] R. E. Kelly, An Investigation Into the Interactions Between Self-Assembled Adenine Molecules and a Au(111) Surface, Small **4**, 1494 (2008).

[206] M. Furukawa, H. Tanaka, and T. Kawai, The Role of Dimer Formation in the Self-Assemblies of DNA Base Molecules on Cu(111) Surfaces: A Scanning Tunneling Microscope Study, J. Chem. Phys. **115**, 3419 (2001).

[207] R. Otero, M. Schck, L. M. Molina, E. Lgsgaard, I. Stensgaard, B. Hammer, and F. Besenbacher, Guanine Quartet Networks Stabilized by Coopertive Hydrogen Bonds, Angew. Chem. Int. Ed. **44**, 2270 (2005).

[208] M. J. Frisch, G. W. Trucks, H. B. Schlegel, G. E. Scuseria, M. A. Robb, J. R. Cheeseman, G. Scalmani, V. Barone, B. Mennucci, G. A. Petersson, H. Nakatsuji, M. Caricato, X. Li, H. P. Hratchian, A. F. Izmaylov, J. Bloino, G. Zheng, J. L. Sonnenberg, M. Hada, M. Ehara, K. Toyota, R. Fukuda, J. Hasegawa, M. Ishida, T. Nakajima, Y. Honda, O. Kitao, H. Nakai, T. Vreven, J. A. Montgomery, Jr., J. E. Peralta, F. Ogliaro, M. Bearpark, J. J. Heyd, E. Brothers, K. N. Kudin, V. N. Staroverov, R. Kobayashi, J. Normand, K. Raghavachari, A. Rendell, J. C. Burant, S. S. Iyengar, J. Tomasi, M. Cossi, N. Rega, J. M. Millam, M. Klene, J. E. Knox, J. B. Cross, V. Bakken, C. Adamo, J. Jaramillo, R. Gomperts, R. E. Stratmann, O. Yazyev, A. J. Austin, R. Cammi, C. Pomelli, J. W. Ochterski, R. L. Martin, K. Morokuma, V. G. Zakrzewski, G. A. Voth, P. Salvador, J. J. Dannenberg, S. Dapprich, A. D. Daniels, . Farkas, J. B. Foresman, J. V. Ortiz, J. Cioslowski, and D. J. Fox, Gaussian 09 Revision B.1, Gaussian Inc. Wallingford CT 2009.

[209] O. A. Vydrov and G. E. Scuseria, Assessment of a Long-Range Corrected Hybrid Functional, J. Chem. Phys. **125**, 234109 (2006).

[210] O. A. Vydrov, J. Heyd, A. V. Krukau, and G. E. Scuseria, Importance of Short-Range Versus Long-Range Hartree-Fock Exchange for the Performance of Hybrid Density Functionals, J. Chem. Phys. **125**, 074106 (2006).

[211] E. R. Johnson, A. Otero-de-la-Roza, S. G. Dale, and G. A. DiLabio, Efficient Basis Sets for Non-Covalent Interactions in XDM-Corrected Density-Functional Theory, J. Chem. Phys. **139**, 214109 (2013).

[212] A. K. Geim and K. S. Novoselov, The Rise of Graphene, Nat. Mater. **6**, 183 (2007).

[213] P. Plachinda, D. R. Evans, and R. Solanki, Electronic Properties of Metal-Arene Functionalized Graphene, J. Chem. Phys. **135**, 044103 (2011).

[214] S. Das Sarma, S. Adam, E. H. Hwang, and E. Rossi, Electronic Transport in Two-Dimensional Graphene, Rev. Mod. Phys. **83**, 407 (2011).

[215] S. Guo and S. Dong, Graphene Nanosheet: Synthesis, Molecular Engineering, Thin Film, Hybrids, and Energy and Analytical Applications, Chem. Soc. Rev. **40**, 2644 (2011).

[216] Z. Xu, Q. Zhang, X. Shi, W. Zhai, and Q. Zhu, Comparison of Tribological Properties of NiAl Matrix Composites Containing Graphite, Carbon Nanotubes, or Graphene, J. Mater. Eng. Perform. **24**, 1926 (2015).

[217] M. S. Won, O. V. Penkov, and D. E. Kim, Durability and Degradation Mechanism of Graphene Coatings Deposited on Cu Substrates Under Dry Contact Sliding, Carbon **54**, 472 (2013).

[218] H. Chen and T. Filleter, Effect of Structure on the Tribology of Ultrathin Graphene and Graphene Oxide Films, Nanotechnology **26**, 135702 (2015).

[219] S. Cahangirov, S. Ciraci, and V. O. Özçelik, Superlubricity Through Graphene Multilayers Between Ni(111) Surfaces, Phys. Rev. B **87**, 205428 (2013).

[220] M. Tripathi, F. Awaja, G. Paolicelli, R. Bartali, E. Iacob, S. Valeri, S. Ryu, S. Signetti, G. Speranza, and N. M. Pugno, Tribological Characteristics of Few-Layer Graphene Over Ni Grain and Interface Boundaries, Nanoscale **8**, 6646 (2016).

[221] L. Zhao, K. T. Rim, H. Zhou, R. He, T. F. Heinz, A. Pinczuk, G. W. Flynn, and A. N. Pasupathy, Influence of Copper Crystal Surface on the CVD Growth of Large Area Monolayer Graphene, Solid State Commun. **151**, 509 (2011).

[222] J. Coraux, A. T. N'Diaye, M. Engler, C. Busse, D. Wall, N. Buckanie, F. J. Meyer Zu Heringdorf, R. Van Gastel, B. Poelsema, and T. Michely, Growth of Graphene on Ir(111), New J. Phys. **11**, 565 (2009).

[223] H. J. Park, J. Meyer, S. Roth, and V. Skákalová, Growth and Properties of Few-Layer Graphene Prepared by Chemical Vapor Deposition, Carbon **48**, 1088 (2010).

[224] Y. Zhang, L. Zhang, and C. Zhou, Review of Chemical Vapor Deposition of Graphene and Related Applications, Acc. Chem. Res. **46**, 2329 (2013).

[225] Y. Zhang, T. Gao, S. Xie, B. Dai, L. Fu, Y. Gao, Y. Chen, M. Liu, and Z. Liu, Different Growth Behaviors of Ambient Pressure Chemical Vapor Deposition Graphene on Ni(111) and Ni films: A Scanning Tunneling Microscopy Study, Nano Res. **5**, 402 (2012).

[226] A. Dahal and M. Batzill, Graphene-Nickel Interfaces: A Review, Nanoscale **6**, 2548 (2014).

[227] W. B. Zhang, C. Chen, and P. Y. Tang, First-Principles Study for Stability and Binding Mechanism of Graphene/Ni(111) Interface: Role of vdW Interaction, J. Chem. Phys. **141**, 044708 (2014).

[228] F. Bianchini, L. L. Patera, M. Peressi, C. Africh, and G. Comelli, Atomic Scale Identification of Coexisting Graphene Structures on Ni(111), J. Chem. Phys. Lett. **5**, 467 (2014).

[229] S. Grimme, Density Functional Theory with London Dispersion Corrections, Wiley Interdisciplinary Reviews: Computational Molecular Science **1**, 211 (2011).

[230] H. Kawanowa, H. Ozawa, T. Yazaki, Y. Gotoh, and R. Souda, Structure Analysis of Monolayer Graphite on Ni (111) Surface by Li^+ Impact Collision Ion Scattering Spectroscopy, Jpn. J. Appl. Phys. **41**, 6149 (2002).

[231] T. Olsen, J. Yan, J. J. Mortensen, and K. S. Thygesen, Dispersive and Covalent Interactions Between Graphene and Metal Surfaces from the Random Phase Approximation, Phys. Rev. Lett. **107**, 156401 (2011).

[232] T. Thonhauser, V. Cooper, S. Li, A. Puzder, P. Hyldgaard, and D. Langreth, Van der Waals Density Functional: Self-Consistent Potential and the Nature of the van der Waals Bond, Phys. Rev. B **76**, 125112 (2007).

[233] D. Langreth, B. I. Lundqvist, S. D. Chakarova-Käck, V. Cooper, M. Dion, P. Hyldgaard, A. Kelkkanen, J. Kleis, L. Kong, S. Li, P. G. Moses, E. Murray, A. Pudzer, H. Rydberg, E. Schröder, and T. Thonhauser, A Density Functional for Sparse Matter, J. Phys.: Condens. Matter **21**, 084203 (2009).

[234] J. Klimeš, D. R. Bowler, and A. Michaelides, Van der Waals Density Functionals Applied to Solids, Phys. Rev. B **83**, 195131 (2011).

[235] H. Muñoz Galán, F. Viñes, J. Gebhardt, A. Görling, and F. Illas, The Contact of Graphene with Ni(111) Surface: Description by Modern Dispersive Forces Approaches, Theor. Chem. Acc. **135**, 165 (2016).

[236] A. Otero-de-la-Roza and E. R. Johnson, Many-Body Dispersion Interactions from the Exchange-Hole Dipole Moment Model, J. Chem. Phys. **138**, 054103 (2013).

[237] F. O. Kannemann and A. D. Becke, Van der Waals Interactions in Density-Functional Theory: Rare-Gas Diatomics, J. Chem. Theory Comput. **5**, 719 (2009).

[238] J. B. Dizon and E. R. Johnson, Van der Waals Potential Energy Surfaces from the Exchange-Hole Dipole Moment Dispersion Model, Can. J. Chem. **94**, 1049 (2016).

[239] F. Kannemann and A. Becke, Van der Waals Interactions in Density-Functional Theory: Intermolecular Complexes, J. Chem. Theory Comput. **6**, 1081 (2010).

[240] A. Otero-de-la-Roza and E. R. Johnson, Predicting Energetics of Supramolecular Systems Using the XDM Dispersion Model, J. Chem. Theory Comput. **11**, 4033 (2015).

[241] A. Otero-de-la-Roza, B. H. Cao, I. K. Price, J. E. Hein, and E. R. Johnson, Predicting the Relative Solubilities of Racemic and Enantiopure Crystals by Density-Functional Theory, Angew. Chem. Int. Ed. **53**, 7879 (2014).

[242] S. Whittleton, A. Otero-de-la-Roza, and E. R. Johnson, Molecular Crystal Polymorphism using the Exchange-Hole Dipole Moment Dispersion Model II: Non-Planar Molecules, J. Chem. Theory Comput. **13**, 5332 (2017).

[243] E. R. Johnson and A. Otero-de-la-Roza, Adsorption of Organic Molecules on Kaolinite from the Exchange-Hole Dipole Moment Dispersion Model, J. Chem. Theory Comput. **8**, 5124 (2012).

[244] J. Shelton, H. Patil, and J. Blakely, Equilibrium Segregation of Carbon to a Nickel (111) Surface: A Surface Phase Transition, Surf. Sci. **43**, 493 (1974).

[245] J. P. Perdew and A. Zunger, Self-Interaction Correction to Density-Functional Approximations for Many-Electron Systems, Phys. Rev. B **23**, 5048 (1981).

[246] R. Wyckoff, *Crystal Structures*, Interscience publishers, New York, 1960.

[247] L. V. Dzemiantsova, M. Karolak, F. Lofink, A. Kubetzka, B. Sachs, K. Von Bergmann, S. Hankemeier, T. O. Wehling, R. Frömter, H. P. Oepen, A. I. Lichtenstein, and R. Wiesendanger, Multiscale Magnetic Study of Ni(111) and Graphene on Ni(111), Phys. Rev. B **84**, 205431 (2011).

[248] R. F. W. Bader, A Quantum Theory of Molecular Structure and its Applications, Chem. Rev. **91**, 893 (1991).

[249] J. Sun, J. B. Hannon, R. M. Tromp, P. Johari, A. A. Bol, V. B. Shenoy, and K. Pohl, Spatially-Resolved Structure and Electronic Properties of Graphene on Polycrystalline Ni, ACS Nano **4**, 7073 (2010).

[250] R. Zacharia, H. Ulbricht, and T. Hertel, Interlayer Cohesive Energy of Graphite from Thermal Desorption of Polyaromatic Hydrocarbons, Phys. Rev. B **69**, 155406 (2004).

[251] L. X. Benedict, N. G. Chopra, M. L. Cohen, A. Zettl, S. G. Louie, and V. H. Crespi, Microscopic Determination of the Interlayer Binding Energy in Graphite, Chem. Phys. Lett. **286**, 490 (1998).

[252] A. Dahal, R. Addou, P. Sutter, and M. Batzill, Graphene Monolayer Rotation on Ni(111) Facilitates Bilayer Graphene Growth, Appl. Phys. Lett. **100**, 241602 (2012).

[253] P. Zeller, F. Speck, M. Weinl, M. Ostler, M. Schreck, T. Seyller, and J. Wintterlin, Healing of Graphene on Single Crystalline Ni(111) Films, Appl. Phys. Lett. **105**, 191612 (2014).

[254] A. Tkatchenko, A. Ambrosetti, and R. A. Distasio, Interatomic Methods for the Dispersion Energy Derived from the Adiabatic Connection Fluctuation-Dissipation Theorem, J. Chem. Phys. **138**, 074106 (2013).

[255] Y. S. Dedkov, M. Fonin, U. Rüdiger, and C. Laubschat, Rashba Effect in the Graphene/Ni(111) System, Phys. Rev. Lett. **100**, 107602 (2008).

[256] L. Kong, C. Bjelkevig, S. Gaddam, M. Zhou, Y. H. Lee, G. H. Han, H. K. Jeong, N. Wu, Z. Zhang, J. Xiao, P. A. Dowben, and J. A. Kelber, Graphene/Substrate Charge Transfer Characterized by Inverse Photoelectron Spectroscopy, J. Phys. Chem. C **114**, 21618 (2010).

[257] A. Tamtögl, E. Bahn, J. Zhu, P. Fouquet, J. Ellis, and W. Allison, Graphene on Ni(111): Electronic Corrugation and Dynamics from Helium Atom Scattering, J. Phys. Chem. C **119**, 25983 (2015).

[258] K. S. Kim, H. J. Lee, C. Lee, S. K. Lee, H. Jang, J. H. Ahn, J. H. Kim, and H. J. Lee, Chemical Vapor Deposition-Grown Graphene: The Thinnest Solid Lubricant, ACS Nano **5**, 5107 (2011).

[259] A. Dianat, D. A. Ryndyk, and G. Cuniberti, Contact-Dependent Mechanical Properties of Graphene Nanoribbons: an ab-initio Study, Nanotech. **27**, 025702 (2016).

[260] L. Kong, A. Enders, T. S. Rahman, and P. a. Dowben, Molecular Adsorption on Graphene, J. Phys. Condens. Matter **26**, 443001 (2014).

[261] J. H. Gao, N. Ishida, I. Scott, and D. Fujita, Controllable Growth of Single-Layer Graphene on a Pd(111) Substrate, Carbon **50**, 1674 (2012).

[262] M. Sasaki, Y. Yamada, Y. Ogiwara, S. Yagyu, and S. Yamamoto, Moiré Contrast in the Local Tunneling Barrier Height Images of Monolayer Graphite on Pt(111), Phys. Rev. B **61**, 15653 (2000).

[263] P. Merino, M. Svec, A. L. Pinardi, and G. Otero, Strain-Driven Moire Superstructures of Epitaxial Graphene on Transition, ACS Nano **5**, 5627 (2011).

[264] M. Gao, Y. Pan, L. Huang, H. Hu, L. Z. Zhang, H. M. Guo, S. X. Du, and H. J. Gao, Epitaxial Growth and Structural Property of Graphene on Pt(111), Appl. Phys. Lett. **98**, 033101 (2011).

[265] N. Chan, S. G. Balakrishna, A. Klemenz, M. Moseler, P. Egberts, and R. Bennewitz, Contrast in Nanoscale Friction between Rotational Domains of Graphene on Pt(111), Carbon **113**, 132 (2017).

[266] A. J. Martínez-Galera, I. Brihuega, and J. M. Gómez-Rodríguez, Ethylene Irradiation: A New Route to Grow Graphene on Low Reactivity Metals, Nano Lett. **11**, 3576 (2011).

[267] G. Giovannetti, P. A. Khomyakov, G. Brocks, V. M. Karpan, J. van den Brink, and P. J. Kelly, Doping Graphene with Metal Contacts, Phys. Rev. Lett. **101**, 026803 (2008).

[268] B. B. Kappes, A. Ebnonnasir, S. Kodambaka, and C. V. Ciobanu, Orientation-Dependent Binding Energy of Graphene on Palladium, Appl. Phys. Lett. **102**, 051606 (2013).

[269] T. Chanier and L. Henrard, From Carbon Atom to Graphene on Cu(111): An ab-initio Study, Eur. Phys. J. B **88**, 31 (2015).

[270] Y. Zhang and W. Yang, Comment on "Generalized Gradient Approximation Made Simple", Phys. Rev. Lett. **80**, 890 (1998).

[271] V. R. Cooper, Van der Waals Density Functional: An Appropriate Exchange Functional, Phys. Rev. B **81**, 161104 (2010).

[272] M. S. Christian, A. Otero-de-la-Roza, and E. R. Johnson, Adsorption of Graphene to Nickel (111) using the Exchange-Hole Dipole Moment Model, Carbon **118**, 184 (2017), Chapter 6 in this thesis.

[273] E. R. Johnson, The Exchange-Hole Dipole Moment Dispersion Model, in *Non-covalent Interactions in Quantum Chemistry and Physics*, edited by A. Otero-de-la-Roza and G. A. DiLabio, chapter 5, pages 169–194, Elsevier, 2017.

[274] T. Wiederholt, H. Brune, J. Wintterlin, R. J. Behm, and G. Ertl, Formation of Two-Dimensional Sulfide Phases on Al(111): An STM Study, Surf. Sci. **324**, 91 (1995).

[275] L. Gao, J. R. Guest, and N. P. Guisinger, Epitaxial Graphene on Cu(111), Nano Lett. **10**, 3512 (2010).

[276] P. Tsipas, S. Kassavetis, D. Tsoutsou, E. Xenogiannopoulou, E. Golias, S. A. Giamini, C. Grazianetti, D. Chiappe, A. Molle, M. Fanciulli, and A. Dimoulas, Evidence for Graphite-like Hexagonal AlN Nanosheets Epitaxially Grown on Single Crystal Ag(111), Appl. Phys. Lett. **103**, 251605 (2013).

[277] M. Enachescu, D. Schleef, D. F. Ogletree, and M. Salmeron, Integration of Point-Contact Microscopy and Atomic-Force Microscopy: Application to Characterization of Graphite/Pt(111), Phys. Rev. B **60**, 16913 (1999).

[278] E. Schröder, V. R. Cooper, K. Berland, B. I. Lundqvist, P. Hyldgaard, and T. Thonhauser, The vdW-DF Family of Nonlocal Exchange-Correlation Functionals, in *Non-covalent Interactions in Quantum Chemistry and Physics*, edited by A. Otero-de-la-Roza and G. A. DiLabio, chapter 8, pages 241–274, Elsevier, 2017.

[279] J. Cho, L. Gao, J. Tian, H. Cao, W. Wu, Q. Yu, E. N. Yitamben, B. Fisher, J. R. Guest, Y. P. Chen, and N. P. Guisinger, Atomic-Scale Investigation of Graphene Grown on Cu Foil and the Effects of Thermal Annealing, ACS Nano **5**, 3607 (2011).

[280] N. R. Wilson, A. J. Marsden, M. Saghir, C. J. Bromley, R. Schaub, G. Costantini, T. W. White, C. Partridge, A. Barinov, P. Dudin, A. M. Sanchez, J. J. Mudd, M. Walker, and G. R. Bell, Weak Mismatch Epitaxy and Structural Feedback in Graphene Growth on Copper Foil, Nano Res. **6**, 99 (2013).

[281] J. C. W. Swart, E. van Steen, I. M. Ciobíc, and R. A. van Santen, Interaction of Graphene with FCC Co(111), Phys. Chem. Chem. Phys. **11**, 803 (2009).

[282] M. S. Christian, A. Otero-de-la-Roza, and E. R. Johnson, Adsorption of Graphene to Metal (111) Surfaces using the Exchange-Hole Dipole Moment Model, Carbon **124**, 531 (2017), Chapter 7 in this thesis.

[283] T. Filleter and R. Bennewitz, Structural and Frictional Properties of Graphene Films on SiC(0001) Studied by Atomic Force Microscopy, Phys. Rev. B **81**, 155412 (2010).

[284] A. L. Kitt, Z. Qi, S. Re, H. S. Park, A. K. Swan, and B. B. Goldberg, How Graphene Slides: Measurement and Theory of Strain-Dependent Frictional Forces between Graphene and SiO_2, Nano Lett. **13**, 2605 (2013).

[285] Z. Chen, P. Darancet, L. Wang, A. C. Crowther, Y. Gao, C. R. Dean, T. Taniguchi, K. Watanabe, J. Hone, C. A. Marianetti, and L. E. Brus, Physical Adsorption and Charge Transfer of Molecular Br_2 on Graphene, ACS Nano **8**, 2943 (2014).

[286] M. S. Lodge, C. Tang, B. T. Blue, W. A. Hubbard, A. Martini, B. D. Dawson, and M. Ishigami, Lubricity of Gold Nanocrystals on Graphene Measured Using Quartz Crustal Microbalance, Sci. Rep. **6**, 31837 (2016).

[287] X. Bian, Q. Wang, X. Wang, L. Wang, W.-Q. Li, G.-H. Chen, and H. Zhu, Graphene Layers on Bimetallic Ni/Cu(111) Surface and Near Surface Alloys in Controlled Growth of Graphene, RSC Adv. **6**, 74973 (2016).

[288] E. Khan, T. S. Rahman, and S. Subrina, Electronic Structure of Bilayer Graphene Physisorbed on Metal Substrates, J. App. Phys. **120**, 185101 (2016).

[289] Q. Wang, L. Wei, M. Sullivan, S.-W. Yang, and Y. Chen, Graphene Layers on Cu and Ni (111) Surfaces in Layer Controlled Graphene Growth, RSC Adv. **3**, 3046 (2013).

[290] C. H. Lui, Z. Li, Z. Chen, P. V. Klimov, L. E. Brus, and T. F. Heinz, Imaging Stacking Order in Few-Layer Graphene, Nano Lett. **11**, 164 (2011).

[291] L. M. Malard, M. A. Pimenta, G. Dresselhaus, and M. S. Dresselhaus, Raman Spectroscopy in Graphene, Phys. Rep. **473**, 51 (2009).

[292] D. Berman, A. Erdemir, and A. V. Sumant, Graphene: A New Emerging Lubricant, Mater. Today **17**, 31 (2014).

[293] L. Wu, L. Gu, Z. Xie, C. Zhang, and B. Song, Improved Tribological Properties of Si_3N_4/GCr_{15} Sliding Pairs with Few Layer Graphene as Oil Additives, Ceram. Int. **43**, 14218 (2017).

[294] J. Zhao, J. Mao, Y. Li, Y. He, and J. Luo, Friction-Induced Nano-Structural Evolution of Graphene as a Lubrication Additive, Appl. Surf. Sci. **434**, 21 (2018).

[295] D. Mishra, F. J. Sonia, D. Srivastava, G. N. Ganesha, U. Singha, and A. Mukhopadhyay, Wear Damage and Effects of Graphene-Based Lubricants/Coatings During Linear Reciprocating Sliding Wear at High Contact Pressure, Wear **400**, 144 (2018).

[296] F. Chen, J. Ying, Y. Wang, S. Du, Z. Liu, and Q. Huang, Effects of Graphene Content on the Microstructure and Properties of Copper Matrix Composites, Carbon **96**, 836 (2016).

[297] L. Ruiz, W. Xia, Z. Meng, and S. Keten, A Coarse-Grained Model for the Mechanical Behavior of Multi-Layer Graphene, Carbon **82**, 103 (2015).

[298] S. Wang, Y. Chen, Y. Ma, Z. Wang, and J. Zhang, Size Effect on Interlayer Shear Between Graphene Sheets, J. Appl. Phys. **122**, 074301 (2017).

[299] D. Abbasi-Pérez, J. M. Menéndez, J. M. Recio, A. Otero-de-la-Roza, E. Del Corro, M. Taravillo, V. G. Baonza, and M. Marqués, Modeling Graphite Under Stress: Equations of State, Vibrational Modes, and Interlayer Friction, Phys. Rev. B **90**, 054105 (2014).

[300] M. S. Christian and E. R. Johnson, Effect of a Metal Substrate on Interlayer Interactions in Bilayer Graphene, The Journal of Physical Chemistry C (2018), Chapter 8 in this thesis.

[301] J. Wellendorff, T. L. Silbaugh, D. Garcia-Pintos, J. K. Norskov, T. Bligaard, F. Studt, and C. T. Campbell, A Benchmark Database for Adsorption Bond Energies to Transition Metal Surfaces and Comparison to Selected DFT Functionals, Surf. Sci. **640**, 36 (2015).

[302] J. Krim, Friction and Energy Dissipation Mechanisms in Adsorbed Molecules and Molecularly Thin Films, Adv. Phys. **61**, 155 (2012).

[303] X. Feng, S. Kwon, J. Y. Park, and M. Salmeron, Superlubric Sliding of Graphene Nanoflakes on Graphene, ACS Nano **7**, 1718 (2013).

[304] M. Dienwiebel, G. S. Verhoeven, N. Pradeep, J. W. Frenken, J. A. Heimberg, and H. W. Zandbergen, Superlubricity of Graphite, Phys. Rev. Lett. **92**, 126101 (2004).

[305] T. Maeda and H. Washizu, Mechanism of Ultra-low Friction of Multilayer Graphene Studied by All Atom Molecular Dynamics, Microsyst. Technol. **24**, 757 (2018).

[306] H. Washizu, S. Kajita, M. Tohyama, T. Ohmori, N. Nishino, H. Teranishi, and A. Suzuki, Mechanism of Ultra Low Friction of Multilayer Graphene Studied by Coarse-Grained Molecular Simulation, Faraday Discuss. **156**, 279 (2012).

[307] A. S. De Wijn, A. Fasolino, A. E. Filippov, and M. Urbakh, Low Friction and Rotational Dynamics of Crystalline Flakes in Solid Lubrication, Europhys. Lett. **95**, 66002 (2011).

[308] A. Smolyanitsky, Effects of Thermal Rippling on the Frictional Properties of Free-Standing Graphene, RSC Adv. **5**, 29179 (2015).

[309] G. Zhang, H. Liu, J. Qu, and J. Li, Two-dimensional Layered MoS_2 : Rational Design, Properties and Electrochemical Applications, Energy Environ. Sci. **9**, 1190 (2016).

[310] Q. Ding, F. Meng, C. R. English, M. Cabán-Acevedo, M. J. Shearer, D. Liang, A. S. Daniel, R. J. Hamers, and S. Jin, Efficient Photoelectrochemical Hydrogen Generation Using Heterostructures of Si and Chemically Exfoliated Metallic MoS_2, J. Am. Chem. Soc. **136**, 8504 (2014).

[311] Y. Gong, J. Lin, X. Wang, G. Shi, S. Lei, Z. Lin, X. Zou, G. Ye, R. Vajtai, B. I. Yakobson, H. Terrones, M. Terrones, B. K. Tay, J. Lou, S. T. Pantelides, Z. Liu, W. Zhou, and P. M. Ajayan, Vertical and In-Plane Heterostructures from WS_2/MoS_2 Monolayers, Nat. Mater. **13**, 1135 (2014).

[312] Materials Genome Initiative, JARVIS-DFT Database for 2D Materials, https://mgi.nist.gov/jarvis-dft.